ABSTRACT

CUSHER, AARON ANTHONY. A Design and Analysis Approach for Drag Reduction on Aircraft with Adaptive Lifting Surfaces. (Under the direction of Professor Ashok Gopalarathnam).

Adaptive lifting surfaces, which can be tailored for different flight conditions, have been shown to be beneficial for drag reduction when compared with conventional non-adaptive surfaces. Applying multiple trailing-edge flaps along the wing span allows for the redistribution of lift to suit different flight conditions. The current approach uses the trailing-edge flap distribution to reduce both induced- and profile- components of drag with a trim constraint. Induced drag is reduced by optimally redistributing the lift between the lifting surfaces and along the span of each surface. Profile drag is reduced through the use of natural laminar flow airfoils, which maintain distinct low-drag-ranges (drag buckets) surrounding design lift values. The low-drag-ranges can be extended to include off-design values through small flap deflections, similar to cruise flaps. Trim is constrained for a given static margin by considering longitudinal pitching moment contributions from changes in airfoil section due to individual flap deflections, and from the redistribution of fore-and-aft lift due to combination of flap deflections. The approach uses the concept of basic and additional lift to linearlize the problem, which allows for standard constrained-minimization theory to be employed for determining optimal flap-angle solutions. The resulting expressions for optimal flap-angle solutions are presented as simple matrix equations.

This work presents a design and analysis approach which is used to produce flap-angle solutions that independently reduce induced, profile, and total drag. Total drag is defined to be the sum of the induced- and profile-components of drag. The general drag reduction approach is adapted for each specific situation to develop specific drag reduction schemes that are applied to single- and multiple-surface configurations. Successful results show that, for the application of the induced drag reduction schemes on a tailless aircraft, near-elliptical lift distributions are produced which match the classical result for minimum induced drag. Application of the profile drag reduction schemes produce solutions which force the wing to operate in the low-drag-ranges of the natural-laminar-flow airfoil sections, thereby lowering profile drag. The total drag reduction schemes use a curve-fit routine that generates airfoil drag polars given flap angle and Reynolds number. The approximated drag polars allow the prediction of profile drag values to be combined with induced drag values

to form a total drag function, which is utilized with a constrained nonlinear optimizer that determines best flap angles for total drag and trim. The different drag reduction schemes each produce independent flap-angle solutions and lift distributions for a given aircraft configuration and operating condition, and provide valuable insight for aerodynamic design and trade studies. The drag reduction approach is intended to be applicable to arbitrary aircraft configurations, and can be adapted to use surface incidence, twist, and flap angles as optimization variables, thereby creating a powerful and flexible aerodynamic design and analysis tool.

A Design and Analysis Approach for Drag Reduction on Aircraft with Adaptive Lifting Surfaces

by

Aaron Anthony Cusher

A dissertation submitted to the Graduate Faculty of
North Carolina State University
in partial fullfillment of the
requirements for the Degree of
Doctor of Philosophy

Aerospace Engineering

Raleigh, North Carolina

2008

APPROVED BY:

Dr. Jack Edwards	Dr. Jeff Joines
Dr. Robert Nagel	Dr. Ashok Gopalarathnam Chair of Advisory Committee

BIOGRAPHY

Aaron Anthony Cusher was born to George and Carolyn Cusher April 16th, 1980 in Fargo, North Dakota. The second of three children, Aaron spent his first five years on a small farm operated by his family located in the South Eastern portion of North Dakota. In 1986, Aaron and his family moved off the farm to the big city of Fargo, where he resided through his graduation from Fargo South High School in the Spring of 1998. That fall Aaron moved to Sioux Falls, SD, to attend Augustana College and pursue academic and athletic opportunities. Four years later he graduated cum laude from Augustana with Bachelor of Arts degrees in Mathematics and Computer Science. Immediately following graduation, Aaron accepted a position as a software engineer and analyst at Citibank in Sioux Falls, working in the fast paced world of credit card disputes. Over the next 15 months this corporate environment inspired him to return to school and focus his mathematical abilities on a more applied field. Aerospace Engineering was selected due to past exposure to the subject through an undergraduate research opportunity. In the Fall of 2003 Aaron moved out of the upper Midwest to Raleigh, NC, and enrolled as a Master's student in Aerospace Engineering at North Carolina State University. He joined the applied aerodynamics group at NC State in the Spring of 2004 under the advisement of Dr. Ashok Gopalarathnam, who supported his Master's and Ph.D. work.

ACKNOWLEDGMENTS

I would like to extend my gratitude to Dr. Ashok Gopalarathnam for his guidance throughout my graduate studies. This work has been possible because of his inspiration and motivation throughout my years at N.C. State, and I am without doubt a better student, engineer, and person because of it. I would also like to recognize and thank Dr. Robert Nagel, Dr. Jack Edwards, and Dr. Jeff Joines for serving as my committee members. Each of them has introduced me to fields of study other than aerodynamics through course work and projects, broadening my knowledge and abilities.

To all my family I would like to say thank you for standing by and supporting me throughout this entire process. I am here today because of each of you and what you have done for me. My biggest thank you goes to my wife, Julie, for all of your undaunted love, support, and encouragement throughout our time together. While I am sure that I have accomplished some things in my life, the greatest of these has been convincing you to spend your life with me. I thank God every day for having you in my life and am increasingly excited about all the tomorrows that I get to share with you. I love you all so much.

TABLE OF CONTENTS

LIST OF TABLES

LIST OF FIGURES

Nomenclature

ac	aerodynamic center
AR	wing aspect ratio
b	wingspan
$\mathbf{D}$	matrix of drag coefficients
BWB	blended wing body
$\bar{c}$	mean aerodynamic chord
C_D	aircraft drag coefficient
C_d	airfoil drag coefficient
cg	center of gravity
C_L	aircraft lift coefficient
C_l	airfoil lift coefficient
C_{L_0}	aircraft lift coefficient for zero α
$C_{lb,camber}$	basic lift coefficient due to airfoil camber
$C_{lb,flap}$	basic lift coefficient due to flap deflection
$C_{lb,twist}$	basic lift coefficient due to wing twist
C_M	aircraft pitching moment coefficient
C_m	airfoil pitching moment coefficient
C_{m_0}	zero-lift airfoil pitching moment coefficient
$C_{M_{basic}}$	aircraft pitching moment coefficient about the neutral point resulting from the basic lift

$C_{M_{sections}}$ aircraft pitching moment coefficient about the neutral point resulting from the airfoil sections

$c(y)$ spanwise chord distribution

D aircraft drag

LDR low drag range

LHS left hand side

L aircraft lift

NLF natural laminar flow

N number of flaps per half span of wing

NP Neutral Point

RHS right hand side

S wing area

SM static margin

TE trailing edge

UAV unmanned aerial vehicle

v induced velocity in the spanwise direction

V_∞ freestream velocity

w normalwash/downwash in the Trefftz-plane

W aircraft weight

X_{cg} longitudinal location of the center of gravity

X_{NP} longitudinal location of the neutral point

Y_{ac} lateral location of the aerodynamic center

α angle of attack

δ_f flap angle

$\bar{\delta}_f$ mean flap angle

$\hat{\delta}_f$ variation flap angle distribution

Γ spanwise distribution of bound-vorticity strength

Λ quarter-chord sweep angle

λ Lagrange multiplier

μ coefficient of dynamic viscosity

ρ density of air

θ_f angular location of flap hinge in radians

Subscripts

a additional

$a, 1$ additional distribution at $C_L = 1$

b basic

cg center of gravity

i, j flap indices

ind induced drag

low lower corner of low-drag range with most-negative flap angle

max maximum, most-positive flap angle

min minimum, most-negative flap angle

NP neutral point

pro profile drag

ref reference

tot total drag

up upper corner of low-drag range with most-positive flap angle

Chapter 1

Introduction

This chapter presents an introduction to adaptive aircraft concepts and unconventional configurations which provides motivation for the current work. The first section discusses adaptive aircraft, beginning with historical examples that provide early concepts relating to the current methods. Several modern examples follow that show drag reduction potential for more recent adaptive configurations. Multiple trailing-edge (TE) flaps are introduced as a method for wing adaptation, and several examples are presented highlighting previous studies using multiple TE flaps for drag reduction. The next section discusses unconventional aircraft configurations, beginning with tailless aircraft to provide insight into their potential and to highlight specific design considerations of tailless configurations. Multiple surface and canard configurations are introduced next to show how multiple surfaces can be used for drag reduction and also display some shortcomings of canard configurations. The next section presents research objectives for this dissertation. Finally, an outline of the dissertation is provided.

1.1 Adaptive Aircraft

1.1.1 Historical Examples

Aircraft that are designed to change shape in flight are said to be adaptive, indicating that the geometry can be adapted to suit different operating conditions. The most common examples of adaptive techniques used on modern aircraft occur on the wings, or primary lifting surface. Methods for changing the shape of an aircraft's wings have been employed

since the earliest designs. Consider the 1903 Wright Flyer, the first heavier-than-air machine to achieve sustained powered flight.[2] The Wright Flyer used a system where the pilot lay on a cradle that shifted sideways on tracks to cause wing warp.[3] The wing warping was a physical twisting of the wingtips by a pulley system attached to the cradle, and provided lateral control of the aircraft. As time progressed, aircraft design tended toward flap-type control surfaces, in which a portion of the wing surface is hinged to modify the surface's shape and overall lift. In 1908, Glenn Curtiss made the first flight of his June Bug aircraft, which had flap-type lateral controls.[3] These Curtiss *ailerons* marked an early advance in lateral-control ability beyond the Wright brothers' wing warping, and ushered in a mainstay technique for wing adaptation. Today, virtually every aircraft design uses some form of hinged surface for control purposes. These control surfaces have grown so familiar that aircraft utilizing them are seldom considered adaptive aircraft. However common, these methods for controlling the aircraft represent the earliest forms of wing shape being changed to adapt an aircraft for different flight conditions.

Shape change of wings have been employed not only for directional, lateral, and yaw control of the aircraft, but also for tailoring aircraft performance to suit specific flight regimes. For example, an aircraft typically encounters its lowest velocities during take-off or landing to ensure the safety of the aircraft and its passengers or cargo. To accommodate the slower speed, high-lift systems are used on the leading and trailing edges of wings. Typically, high-lift devices consist of trailing-edge flaps and leading-edge slats which are deflected symmetrically to increase the curvature of the wing, thereby increasing its maximum lift potential. High-lift systems are common amongst general aviation, commercial, and military aircraft and are often the only way for an aircraft to adapt itself for different flight conditions. However, less common methods of wing adaptation exist, such as variable wing sweep, which was used by the Air Force's supersonic F-111 aircraft.[3] Sweeping the wings forward benefited performance when flying at low subsonic speeds, such as for take-off and landings, while sweeping the wings back reduced drag during supersonic flight. While unconventional, variable wing sweep has proven to be a successful method for adapting an aircraft for different flight regimes. Evidence for this is shown by the longevity of the Grumman F-14 Tomcat, which has been operational in the United States since the early 1970s.

Natural examples provide motivation and insight into the potential for adaptive configurations. Birds of every species use their ability to change wing shape, size, and

angle to gain superior control and efficiency. Similar to the way humans use their senses and coordination for balance, birds almost continuously change their bodies as they fly, adapting to variations in speed, altitude, and endurance. For example, they can tuck their wings into their bodies for high speed flight, or puff out their feathers and camber their wings to produce high lift and drag for deceleration and slower speed. Further, they have the ability to shift their weight fore and aft to produce a variable center of gravity, providing stability over a wide range of flight conditions. When considering the potential for adaptive configurations, birds should be considered as the ultimate example. In fact, researchers such as Spillman[4] have used birds as motivation for adaptive spanwise camber studies and indicated drag reduction benefits for adaptive wings versus similar fixed wings.

1.1.2 Modern Examples

As the demand for efficient aircraft increases, adaptive configurations which can easily tailor themselves for low drag at different flight conditions become likely substitutes to fixed configurations. Several modern examples exist which attempt to reduce drag through the use of adaptive surfaces. Zink, Love, and Youngren[5] presented results for an adaptive tailless aircraft aircraft which uses mission adaptive trailing-edge flaps and fuel state control through fuel pumping. The flaps used on this configuration included both conventional flaps and conformal flaps that provide smooth, continuous camber change and allow for flap twisting. Results for this large, high-endurance adaptive configuration (wing area = 1717 sq. ft. and wingspan = 181 ft.) showed that between 5 and 15% increase in range could be achieved by using optimal flap scheduling and fuel pumping. This increase in range relates to hundreds of miles gained through the use of these adaptive methods.

In 2004, Neal and Good et al.[6] presented wind tunnel test results for a fully adaptive aircraft configuration. The adaptive model used for that study was designed to achieve large scale wing shape changes, including variable sweep, span, and twist. Tests were conducted to investigate the drag response of five specific configuration examples, each with a different combination of wing sweep angle, wingspan, and wing twist distribution. Wind tunnel results showed that the different configurations resulted in minimum drag over wider C_L range then a similar fixed configuration. The authors concluded that using a configuration which can change shape results in low drag, with specific benefits shown through changing wing sweep and span.

Ricci and Terraneo[7] presented results for an Active Adaptive Wing Camber (AAWC) concept, which is based on a device that is able to continuously change the camber of a wing. The AAWC concept uses traditional leading-edge and trailing-edge devises to change the camber of the wing at multiple locations along the wingspan. An optimizer is employed for determining the spanwise camber distribution for minimum induced drag. The authors theorize that using such an adaptive concept leads to improved aerodynamic efficiency, increased Mach number capability, improved buffet boundary, increased operational flexibility, reduced structural weight, and in general reduced fuel burn. Results were presented for a three-surface aircraft which had 12 camber design points on the wing. Results for this aircraft showed induced drag reduction ranges from 15.17% to 5.9% when using the AAWC concept versus using a similar configuration with standard control surfaces.

The above examples highlight some modern attempts at adaptive configurations for low drag which are similar to the methods derived for this work. Each example presents a different concept for wing adaptation, however the results are the same. Drag is reduced when implementing a well designed adaptive concept versus a standard fixed configuration. These examples provide motivation for exploring adaptive configuration concepts and show potential for their use.

1.1.3 Multiple TE Flaps

Trailing-edge flaps are a simple and effective methods for wing adaptation, and are very familiar to modern aircraft design. Multiple trailing-edge flaps distributed along the span of a wing builds on these benefits and has great potential for drag reduction. Just as a single flap uses camber change to affect the lift properties of a wing over the flap area, several trailing-edge flaps may be used in conjunction with one another to change the camber of the entire wing span. This adaptive camber change technique can be used to redistribute of lift of a wing for optimum drag. Benefits of this adaptive method has been shown in several studies,[4,8–11] and adaptive trailing-edge flaps are used frequently on high performance sailplanes today. While simple, trailing-edge flap deflections which redistribute the wing lift are a powerful and efficient method for drag reduction, which provides motivation for their usage. Figure 1.1 displays a wing with multiple trailing edge flaps.

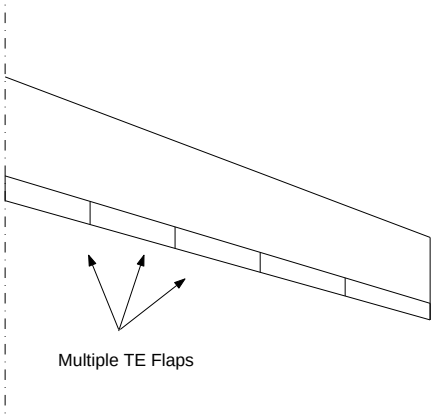

Figure 1.1: Wing displaying a multiple trailing edge flap configuration.

The N.C. State Applied Aerodynamics Group has conducted several adaptive wing projects using multiple trailing edge flap configurations that have provided direction for this dissertation. King and Gopalarathnam[12] presented a method for determining ideal lift distributions and flap angles for adaptive wings using distributed flaps. The methods were designed to minimize induced and profile drag without trim constraints, as it was assumed that the adaptive wings were part of a wing-tail configuration and the tail would be used for trimming the airplane. Ideal lift distributions were first determined from aerodynamic theory, then flap angles were determined to produce lift distributions that matched the ideal distributions. This method was shown to be successful for drag reduction on both planar and non-planar wings examples.

Cusher and Gopalarathnam[13] extended the methodology developed by King and Gopalarathnam by adding a trim constraint. This work explored in-depth the pitching moment contributions that multiple trailing-edge flaps have on an adaptive aircraft. Optimal trimmed lift distributions were produced based on aerodynamic theory which solves for lift distributions resulting in minimum induced drag with constraints, and flap angle setting were determined to produce lift distributions to match. Induced and profile drag minimization routines were developed. The method was applied to an example tailless aircraft configuration to highlight the capabilities for producing reduced drag and trim. Segawa and Gopalarathnam[14] conducted similar studies on roll control of a multiple TE flap configuration. In those studies the TE flap distribution was used for determining optimal lift

distributions with lateral rolling moment constraints. Shipley and Gopalarathnam[15] further studied multiple TE flap configurations by considering static aeroelastic effects of adaptive wings.

Several other adaptive airfoil and wing studies have been conducted at N.C. State relating to multiple TE flaps, including the development of an automated cruise flap by McAvoy and Gopalarathnam.[16] This automated cruise flap uses a sense-and-adapt routine which analyzes pressure readings taken from the upper and lower surfaces of the airfoil to optimally position the airfoil stagnation point for low drag. Stability and control issues of a wing with automated cruise flaps were addressed by Vosburg and Gopalarathnam[17] as well as Cox, Gopalarathnam, and Hall.[18,19] Jepson and Gopalarathnam[20] conducted wind tunnel experiments of a wing with multiple automated cruise flaps.

The efforts presented above show the power and potential for using multiple TE flaps as a wing adaptation method. They provide valuable insight into the fundamentals necessary for successful drag reduction approaches and give the background for the work of this dissertation.

1.2 Unconventional Configurations

1.2.1 Tailless Aircraft

Over the past 100 years, although most aircraft have been designed with a wing (as the primary lifting surface) and an aft tail (for stability and trim), there have been several unconventional configurations. Tailless aircraft are examples of unconventional configurations. However modest, tailless configurations have found popularity along side tailed configurations in particular applications. These applications include sailplanes and gliders, light airplanes, unmanned aerial vehicles (UAV), high-speed military planes, supersonic airliners, and hypersonic re-entry vehicles.[21] One need not look any further than the Northrup B-2 "stealth"-bomber in order to get a sense of the potential that future tailless designs hold. And because only one lifting surface is used, it has often been proposed that drag benefits should be realized and design costs kept lower when implementing a tailless design verses a comparable tailed design.[22] Despite these positives, tailless configurations have seen limited use in general aviation and commercial aircraft design, most likely due to inherent complexity in the aerodynamic design of tailless aircraft and perhaps also due to the over-

whelming history of tailed-aircraft use, giving indication of the need for the advancement in tailless design technology.

One hindrance to the development of tailless aircraft is the idea that these aircraft present difficulty for achieving longitudinal stability and trim, as pointed out by Kroo.[23] With seemingly limitless parameters used in modern aircraft design, including wing and tail geometry variables, engine size, and operational parameters for several flight conditions, it is understandable that the conservative tailed design has stood the test of time as it satisfies trim with little optimization necessary.[24] However, analysis by Kroo has shown that the removal of an aircraft's tail can result in aircraft gross weight, fuel consumption, and direct operating cost reduction when compared to similar tailed configurations.[24] And further, by employing the design philosophy of Reimar and Walter Horten of Germany that has the lift at the wing tips nearly zero and utilizes twist to push much of the lift inboard, a tailless aircraft that is very stable longitudinally is possible.[22] In fact, this method describes the classic bell-shaped lift distribution that is typical of successful designs employed on modern tailless aircraft.

Although tailless aircraft have found most favor with UAV and military applications, there is evidence that such a configuration may one day be utilized by the commercial airline industry. The Boeing Company, in a joint venture with NASA, has recently been exploring a "blended-wing-body" (BWB) concept that has shown preliminary improvements in airliner efficiency.[22] Boeing studies have shown 15% reduction in sized take-off weight, 20% improvement in L/D, 27% reduction in fuel usage, 27% lower thrust, and 12% lower operating empty weight when compared to a similar tailed design.[25] The design has a large delta-shaped wing/fuselage center section which accommodates a two-story passenger cabin. Such a design leads to reductions in root bending moment stresses, as the fuselage is largely incorporated in the wing section. It seems that this a design most suited for a very large airliner, however negatives such as a large, windowless cabin may lead to passenger discomfort, and need to be addressed.

Figure 1.2 displays an adaptive tailless aircraft with multiple TE flaps along its span. Noted is the location of the aerodynamic center to highlight its importance for successful design. Similar adaptive tailless configurations will be studied in upcoming chapters of this dissertation to show drag reduction methods. A single surface configuration offers

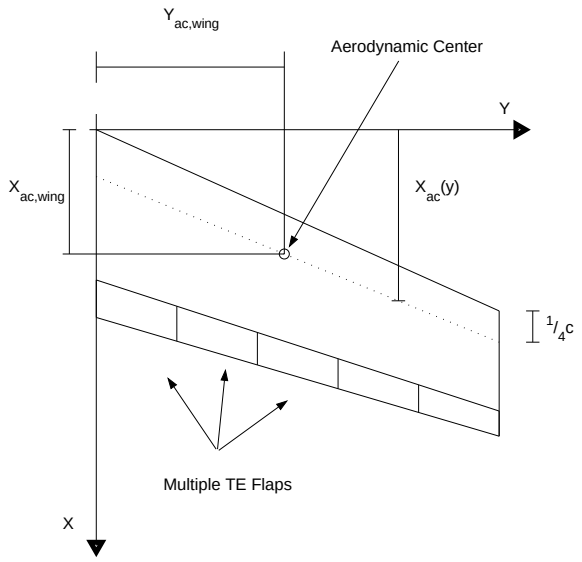

Figure 1.2: Planform of wing with multiple trailing-edge flaps (right side shown). Location of wing aerodynamic center is marked.

simplicity for describing specific aspects of drag reduction schemes with trim constraints, and highlights the aerodynamic trade-offs associated with constraints.

1.2.2 Canard and Multiple-Surface Configurations

Multiple-surface configurations have been studied extensively in the past, where Prandtl's biplane equation[26] served as the first popular approach for induced drag prediction. Noted for its simplicity, the biplane equation assumes elliptically loaded surfaces and results in span efficiency that varies with changes in span and vertical gap ratios alone. While Prandtl's equation enabled several early studies, modern analysis methods have shown that elliptical distributions on each surface, particularly those operating in the downwash field of another surface, do not necessarily result in minimum induced drag. Several researchers have provided modified versions of Prandtl's equation[27–29] for multiple surface configurations, each presenting steps forward in understanding optimal spanwise lift and surface lift ratios. Research performed by Kroo and McGeer[30] on conventional, tailed and canard configurations presented comparisons of surfaces twisted for minimum induced drag and trim, and highlighted shortcomings of canard configurations. Most notable is the inability for canard configurations to achieve the low induced drag values of comparable tailed configurations

at the same static margins, due to the forward center of gravity location required by the canard.

Three-surface configurations provide unique opportunities for aerodynamic analysis, as the additional surface adds variables for solving optimal lift with trim constraints. With three surface lift variables available, there are infinite possibilities for producing longitudinal trim, thus allowing for optimal lift and trim to occur simultaneously. This redundancy in design variables has led to interest in three surface aircraft, as indicated by several references.[31–33] Goodrich, et al.,[34] studied a three surface aircraft optimized for induced drag and trim. In that study, the incidence angles of the three surfaces were determined using a linear optimization procedure similar to that developed here, and the suggested incidence angles resulting in slightly negative loads on the aft tail.

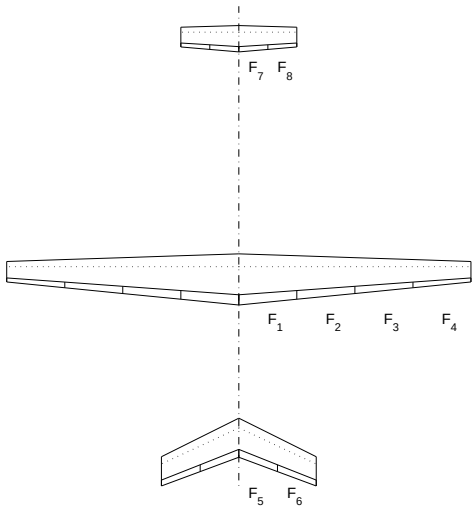

Figure 1.3: Example three surface airplane with eight adaptive trailing-edge flaps.

Figure 1.3 displays an example three-surface aircraft using multiple TE flaps on each surface as a method for wing adaptation. The drag reduction approaches presented in this dissertation will study similar adaptive configurations and present aerodynamic analysis of adaptive three-surface aircraft. Previous study of multiple surface optimization[27–34] has shown both positives and negatives for their usage, and indicate complexity for the design of adaptive multiple-surface aircraft with constraints. The research in this dissertation presents an optimization procedure that seeks to simplify the aerodynamic design and optimization process and give insight into the benefits and pitfalls of multiple surface configuration.

1.3 Objectives of Dissertation

The focus of this dissertation is the development of a design and analysis method for adaptive subsonic aircraft utilizing multiple TE flaps. Previous adaptive wing studies performed at N.C. State University are built upon which use the concept of basic and additional lift to linearize flap-deflection effects on spanwise lift and downwash distributions. The current approach seeks to exploit the drag-reduction potential shown by the previous approaches to create a more universal aerodynamic design and analysis tool for determining optimal lift distributions and reduced drag.

Specific objectives of this research were to:

1. Formulate the problem using standard mathematical definitions and follow constrained minimization theory for determining optimal flap deflections.

2. Develop methods to universally accept single or multiple surface configurations and optimize TE flap angles for minimum induced, profile, and total drag.

3. Allow the addition of longitudinal trim constraints and solve for optimal TE flap angles for minimum trimmed drag.

4. Develop a drag polar approximation routine to accurately predict profile drag of a NLF airfoil, and use the approximate drag polars for lowering profile and total drag of a multiple TE flap configuration.

5. Produce methods that allow for several aerodynamic optimization variables, including TE flaps, wing twist, and wing incidence.

6. Show results of the drag reduction methods applied to a tailless aircraft and highlight how trim constraints affect drag on a single surface.

7. Show results of the drag reduction methods applied to a three-surface aircraft to highlight the benefits of additional surfaces for producing minimum drag and trim simultaneously.

1.4 Outline of Dissertation

Chapter 2 presents background and methodology information pertaining to the development of drag reductions schemes applied to multiple TE flap configurations. Background is provided for well-known applied aerodynamic concepts, including: basic and additional lift distributions, induced drag of superposed lift distributions, profile drag approximation of airfoils, static margin and pitching moment constraints, and TE flap for drag bucket control. Further, a mathematical background is presented for relative minima of multi-variable functions with constraints. The methodology section describes how pitching moment is decomposed for the drag reduction methods, and how the TE flap angles are defined. Superposition of lift distributions is described, and a drag polar approximation routine is introduced. Finally, methodology is described for solving TE flap angles resulting in minimum drag, including: induced drag, trimmed induced drag, profile drag, and total drag. This chapter addresses objectives $1 - 5$.

Chapter 3 discusses the problem set up and results of the drag reduction methods introduced in chapter 2 applied to a tailless aircraft. Specific drag reduction schemes are provided which result in minimum trimmed induced, profile, and total drag. An example configuration is provided and results are displayed for variations in wing sweep angle and airfoil section. This chapter addresses objective 6.

Chapter 4 provides specific drag reduction schemes for multiple surface configurations and presents results for an example three surface aircraft. These results discuss the aerodynamic benefits of additional surfaces and show minimum drag results with trim. This chapter addresses objective 7.

Chapter 5 summarizes the results of the research and presents conclusions. Possible future work on adaptive configurations using multiple TE flaps is also provided.

Chapter 2

Flap Angles for Minimum Drag

This chapter describes necessary background information that was used by this work as well as the methodology for determining optimal lift distributions of an adaptive configuration utilizing multiple trailing-edge flaps.

2.1 Background

This section provides background information on well-known applied aerodynamic and mathematical principles that were used by this body of work. The background is presented in six subsections. Subsection 2.1.1 provides a description of the concept of basic and additional lift distributions. Subsection 2.1.2 discusses how induced drag is derived from superposed lift distributions. Profile drag of airfoils is introduced in the third subsection. The fourth and fifth subsections provide background information on constraints, beginning with relative minima of multi-variable functions with constraints, followed by airfoil static margin and pitching moment constraints. Lastly, subsection 2.1.6 presents a brief review of how trailing-edge (TE) flaps are used to control the low-drag range of an airfoil.

2.1.1 Basic and Additional Lift Distributions

Within the assumption of linear aerodynamics (linear $C_l - \alpha$ variation and linear $C_l - \Gamma$ relationship), the spanwise distribution of bound circulation (or alternatively, lift distribution) over a wing can be expressed as a sum of two contributions:[35–37] i) basic distribution,

$\Gamma_b(y)$ and ii) additional distribution, $\Gamma_a(y)$:

$$\Gamma(y) = \Gamma_b(y) + \Gamma_a(y) \tag{2.1}$$

The basic distribution, Γ_b, is the Γ distribution at $C_L = 0$, and is the result of spanwise variation in geometric twist, aerodynamic twist due to camber, and flap deflections. Further, the Γ_b distributions due to twist, camber, or flap deflection scale linearly with that particular parameter, and individual Γ_b distributions can be added to equal the total Γ_b distribution, as shown in Eq. 2.2

$$\Gamma_b(y) = \Gamma_{b,twist}(y) + \Gamma_{b,camber}(y) + \Gamma_{b,flap}(y) \tag{2.2}$$

The additional Γ distribution, $\Gamma_a(y)$, is due to changes to α for the wing with zero geometric and aerodynamic twist, and therefore scales linearly with wing C_L. Thus, the additional Γ distribution for $C_L = 1$, written as $\Gamma_{a,1}$, can be precomputed for a wing and used to compute the Γ_a for any C_L, as follows:

$$\Gamma_a(y) = C_L \Gamma_{a,1}(y) \tag{2.3}$$

If the component of the induced velocity along the freestream direction, v, is assumed to be small compared to V_∞, then the magnitude of the local loading is proportional to the local Γ distribution:

$$L'(y) = \rho(V_\infty + v(y))\Gamma \approx \rho V_\infty \Gamma \tag{2.4}$$

leading to the following linear relationship between Γ and the load lift coefficient, C_l:

$$C_l(y) = \frac{2\Gamma}{cV_\infty} \tag{2.5}$$

It is, therefore, possible to write the spanwise C_l distribution using superposition as follows:

$$C_l(y) = C_{lb,twist}(y) + C_{lb,camber}(y) + C_{lb,flap}(y) + C_L C_{la,1} \tag{2.6}$$

2.1.2 Induced Drag of Superposed Lift Distributions

It is well known that for a given bound-circulation distribution, the induced drag, D_{ind}, can be obtained by integration along the wake trace in the Trefftz plane as follows:

$$D_{ind} = \frac{\rho}{2} \int_{-\frac{b}{2}}^{\frac{b}{2}} \Gamma(y) w(y) dy \tag{2.7}$$

where, $w(y)$ is the Trefftz-plane downwash distribution. This equation has been written for a planar wing with a rigid wake spanning from $y = -\frac{b}{2}$ to $y = \frac{b}{2}$.

In non-dimensional form, the induced drag coefficient, $C_{D_{ind}}$, can be written as:

$$C_{D_{ind}} = \frac{1}{2S} \int_{\frac{-b}{2}}^{\frac{b}{2}} c(y) C_l(y) \frac{w(y)}{V_\infty} dy \tag{2.8}$$

where $\frac{w(y)}{V_\infty}$ is the spanwise distribution of downwash angle in the Trefftz plane.

Noting that the $w(y)$ distributions can also be constructed using superposition of basic and additional distributions, just like the $C_l(y)$ distribution of Eq. 2.6, the total induced drag coefficient can be written using superposition. As an illustration, consider a superposed lift distribution constructed from two distributions P and Q. The total induced drag coefficient of the superposed lift distribution can be written as:

$$C_{D_{ind}} = C_{D_{PP}} + C_{D_{PQ}} + C_{D_{QP}} + C_{D_{QQ}} \tag{2.9}$$

where, for each term on the right-hand-side the first subscript indicates the source of the $c(y)C_l(y)$ distribution and the second subscript indicates the source of the $\frac{w(y)}{V_\infty}$ distribution. For example,

$$C_{D_{PQ}} = \frac{1}{2S} \int_{\frac{-b}{2}}^{\frac{b}{2}} c(y) C_{l_P}(y) \frac{w_Q(y)}{V_\infty} dy \tag{2.10}$$

Further, using Munk's mutual drag theorem,[38] the expression for total induced drag coefficient can be further simplified because $C_{D_{PQ}} = C_{D_{QP}}$, and so on.

2.1.3 Profile Drag Approximation for Wings

Profile drag at low subsonic Mach numbers is determined by skin friction when there is no separated flow and associated pressure drag. To compute profile drag, the shape of an airfoil needs to be considered, as airfoil shape determines the flow properties over the surface of the airfoil. Reynolds number is a non-dimensional quantity which gives a measure the ratio of viscous forces to inertial forces for a given flow field as follows:

$$Re = \frac{\rho V c}{\mu} \tag{2.11}$$

where ρ is the density of the fluid, V is the velocity, c is a characteristic length (typically the chord for airfoils), and μ is the coefficient of dynamic viscosity. In determining profile

drag for an airfoil, it is important to analyze the flow over the airfoil at the correct Reynolds number.

The measure of profile drag for an airfoil is often plotted versus lift to form a $C_d - C_l$ plot, or drag polar. XFOIL[39] is an analysis code which uses a high-order panel method with an integral boundary-layer technique for determining aerodynamic characteristics, such as lift and drag, of an airfoil. XFOIL takes an airfoil geometry as input and calculates C_l and C_d for a range of angles-of-attack and an operating Reynolds number, outputting the drag polar. For this dissertation, XFOIL was used to create the necessary drag polars. For the range of operating conditions used in this study, XFOIL has been found to predict airfoil characteristics that match well with experimental results.[16,39]

Airfoil drag polars can be used in combination with the spanwise lift distribution to approximate the profile drag of a 3-D wing. Provided one or more drag polars describing the $C_l - C_d$ relationships of the airfoil section used on the wing, the spanwise $C_{d,pro}(y)$ distribution can be interpolated and integrated across the span as follows:

$$C_{D_{pro}} = \frac{2}{S} \int_0^{\frac{b}{2}} c(y) C_{d,pro}(y) dy \tag{2.12}$$

where S is the reference wing area and $c(y)$ is the spanwise chord distribution. The factor of 2 ahead of the integral accounts for the half-span integration limits. Several drag polars may be used to increase the accuracy of the approximation to account for spanwise changes in airfoil section and Reynolds number.

2.1.4 Relative Minima of Multi-Variable Functions with Constraints

Consider a function of several variables, $f(\mathbf{x})$, which has first and second partial derivatives everywhere. The necessary condition for a minimum in f is that the first derivative with respect to all the variables $\mathbf{x}$ should be zero[40] as follows:

$$\frac{\partial f}{\partial \mathbf{x}} = 0 \tag{2.13}$$

The sufficient condition for a minimum is that the Hessian matrix composed of the terms $\frac{\partial^2 \mathbf{f}}{\partial \mathbf{x_i} \partial \mathbf{x_j}}$, evaluated at the extrema from Eq. 2.13, be positive definite.

With the addition of an equality constraint, $g(\mathbf{x}) = \mathbf{0}$, the constrained minimum of $\mathbf{x}$ can be determined by using a Lagrange multiplier, λ. The new objective function to be minimized is now written as $H(\mathbf{x}, \lambda) = \mathbf{f}(\mathbf{x}) + \lambda \mathbf{g}(\mathbf{x})$. The necessary condition for the

constrained minimum is that the first derivative of H with respect to all x and λ should be zero, as follows:

$$\frac{\partial H}{\partial \mathbf{x}} = 0, \quad \frac{\partial H}{\partial \lambda} = 0 \tag{2.14}$$

2.1.5 Static Margin and Pitching Moment Constraint

When designing a aircraft of any type, longitudinal stability and trim are of primary concern. Traditionally most aircraft have been designed using a tailed configuration, which utilizes a wing as the primary lifting surface and a tail for trim, stability and control purposes. However, many configurations exist which lack this traditional design, such as tailless aircraft and canard designs. For aircraft such as these it is of critical importance that the lift distribution and airfoil section be designed with longitudinal trim and stability in mind.

Static margin (SM) is the distance between the aircraft center of gravity and neutral point, and is typically non-dimensionalized using a reference chord length $\frac{(X_{NP}-X_{cg})}{c_{ref}}$. Neutral point is the longitudinal location about which C_M does not change with angle of attack. It can be shown that the neutral point is at the centroid of the additional lift distribution. For positive longitudinal stability, the center of gravity should be designed to be forward of the neutral point, thus requiring a positive value for static margin. The greater value of SM, the greater the stability of the aircraft.

Static margin also plays an important role for longitudinal trim. An aircraft is trimmed when there is no net pitching moment about the center of gravity, or $C_{M_{cg}} = 0$. Equation 2.15 displays the relationship between SM and the moment coefficients for an aircraft, and Fig. 2.1 provides a graphical presentation of the terms in this equation for an airfoil. It is important to note that while an airfoil is displayed in the figure, the relationships shown also apply to an aircraft configuration.

$$C_{M_{cg}} = C_{M_{NP}} - C_L \frac{(X_{NP} - X_{cg})}{c_{ref}} \tag{2.15}$$

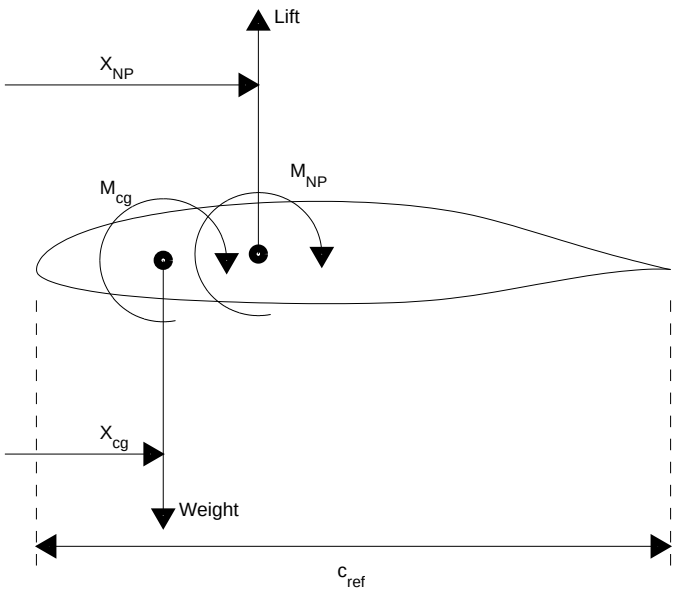

Figure 2.1: Forces applied to an airfoil representing the relationship between pitching moments and SM.

It follows that for a given static margin and C_L, the necessary condition for longitudinal trim ($C_{M_{cg}} = 0$) can be rewritten in terms of a desired $C_{M_{NP}}$, as shown in Eq. 2.16.

$$C_{M_{NP}} = C_L \frac{(X_{NP} - X_{cg})}{c_{ref}} \tag{2.16}$$

Thus if an aircraft is required to fly at a desired C_L with a known SM, the $C_{M_{NP}}$ needs to be constrained as per Eq. 2.16. Because SM should be positive for longitudinal stability and C_L should also be positive, it follows that $C_{M_{NP}}$ will be a positive value.

For the current work it will be shown that $C_{M_{NP}}$ becomes the constraint on the drag reduction schemes as it is critical for longitudinal stability and trim. Further, the moment about the neutral point can be broken down into contributions from two distinct sources: (1) the airfoil sections of a wing, and (2) the lift distribution of a wing. The benefit of this breakdown will be evident when specific drag reduction schemes are introduced.

2.1.6 TE Flap for Drag Bucket Control

For flight at low subsonic Mach numbers, wing profile drag is determined by skin-friction when there is no separated flow and associated pressure drag. To minimize profile drag, airfoils are often designed to have significant regions of favorable pressure gradient on both the upper and lower surfaces to support laminar flow. Such natural laminar flow (NLF) airfoils typically have a distinct low-drag range (LDR), or drag bucket, which is the range of lift coefficients over which low drag is achieved. To extend the range of lift coefficients over which low drag is achieved, a trailing-edge "cruise" flap is often used. First introduced by Pfenninger,[41,42] it has since been used on several airfoil designs,[1,43–46] especially on airfoils for high-performance sailplanes.[44]

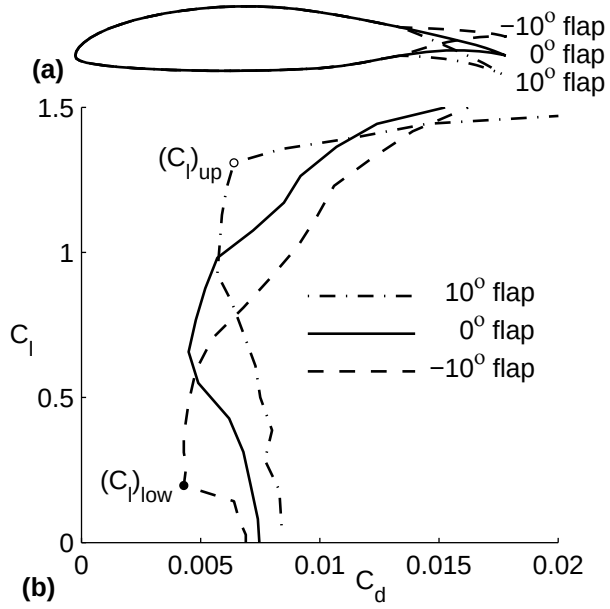

Figure 2.2: Example use of TE cruise flap to adjust the location of airfoil low-drag range: (a) Geometry and (b) Drag polars from wind-tunnel experiments[1] for the NLF(1)-0215F airfoil at Reynolds number of 6 million.

Figure 2.2 illustrates the effect of a trailing-edge flap on a the low-drag range of the NASA NLF(1)-0215F airfoil,[1] used in this illustration as an example. It is seen that a positive (TE down) flap angle results in the low-drag range moving to higher values of C_l and vise-versa for a negative flap angle. Thus, it is seen that low profile C_d is achieved over a

larger C_l range using a TE flap than without the flap. This benefit is limited to a small range of flap angles, typically close to ± 10 deg, beyond which flow separation at the flap hinge results in large pressure drag, which negates the benefit from the reduction in skin-friction drag. These limiting values of flap angle, when the flap is used for drag reduction, are referred to in this dissertation as the most negative flap angle, $\delta_{f_{min}}$, and the most-positive flap angle $\delta_{f_{max}}$. Using the results for the NLF(1)-0215F airfoil in Fig. 2.2 as an example, low C_d can be achieved with $\delta_{f_{max}}$ of +10 deg flap. For any value of operating C_l that lies between $C_{l_{low}}$ and $C_{l_{up}}$, using a flap angle that is determined by linear interpolation between $\delta_{f_{min}}$ and $\delta_{f_{max}}$ will result in a smooth variation of the TE flap angle with operating C_l, while ensuring low C_d.

2.2 Methodology

Presented in this section are descriptions of the drag reduction techniques developed for this work. Several important components of the work are described independently, and are intended to be utilized in conjunction with one another when applied to a specific problem. Because different configurations require different applications of the drag reduction approaches, the methodology presented here is more generic and is intended to introduce the fundamental drag reduction processes. The Results section will provide examples of the methods applied to different configurations and specific drag reduction schemes will be developed.

The methodology is presented in eight subsections. The first subsection shows how aircraft pitching moment is defined as it pertains to this work. The next subsection presents an approach for defining the TE flap-angle distribution. The third subsection discusses superposition of lift distributions. Subsections four, five, and six present methodology for solving flap angles resulting in minimum drag, including: unconstrained induced drag in subsection four, trimmed induced drag in subsection five, and profile drag in subsection six. Subsection seven introduces a routine for approximating the drag polar of a NLF airfoil. Lastly, methods for determining flap angles for minimum total drag using a constrained optimization approach are described in subsection eight.

2.2.1 Pitching Moment Decomposition for a Flapped Configuration

The drag reduction methods developed by this work are intended to be applicable to configurations typical of subsonic aircraft, including tailed, tailless, and canard configurations. It is important to consider longitudinal trim when analyzing such configurations. Shown in Sec. 2.1.5 was the relationship between the neutral point (NP), center of gravity (cg), and static margin (SM) of an airfoil. These relationships can be similarly applied to an aircraft.

Shown in Eq. 2.17 is the moment about the NP and how it relates to the moment about the aircraft center of gravity and static margin, $\frac{(X_{NP}-X_{cg})}{\bar{c}}$.

$$C_{M_{cg}} = C_{M_{NP}} - C_L \frac{(X_{NP} - X_{cg})}{\bar{c}} \tag{2.17}$$

For trim, $C_{M_{cg}}$ is set equal to zero, and leads to the necessary condition that $C_{M_{NP}}$ is positive, assuming a positive SM for longitudinal static stability and positive C_L, as displayed here:

$$C_{M_{NP}} = C_L \times SM \tag{2.18}$$

Multiple surfaces and multiple TE flaps provide several variables for altering the pitching moment about the NP. These variables are expanded and grouped as follows to solve for neutral point pitching moment resulting from a series of TE flap deflection angles δ_f:

$$C_{M_{NP}} = \sum_{j=1}^{N} (C_{M_{sections,j}} + C_{M_{basic,j}})\delta_{f,j} + C_{M_{sections,0}} + C_{M_{basic,0}} = C_L \times SM \tag{2.19}$$

In the above equation the subscript *sections* refers to the airfoil section pitching moment, and the subscript *basic* refers to the pitching moment on the configuration caused by a basic lift distribution. Note that, by definition, the additional lift distribution does not cause any pitching moment about the NP. $C_{M_{sections,j}}$ and $C_{M_{basic,j}}$ are the pitching moment contributions from a unit deflection of flap j. Thus, each flap produces a pitching moment from two sources, each of which can be calculated for a unit deflection and stored, then multiplied by a flap angle to get the pitching moment response for any deflection angle. The $C_{M_{sections,j}}$ term is integrated as:

$$C_{M_{sections,j}} = \frac{2}{S\bar{c}} \int_{y_{j,start}}^{y_{j,end}} C_{m_{\delta_{f,j}}} c(y)^2 dy \tag{2.20}$$

and the $C_{M_{basic,j}}$ term is integrated as:

$$C_{M_{basic,j}} = \frac{2}{S\bar{c}} \sum_{k=1}^{M} \int_{0}^{\frac{b}{2}(k)} c(y) C_{l_{b,\delta_f,j}}(y) \Delta x(y) dy \tag{2.21}$$

The $C_{m_{\delta_f,j}}$ term in Eq. 2.20 is the flap effectiveness parameter predicted by thin airfoil theory, and the $C_{l_{b,\delta_f,j}}(y)$ term in Eq. 2.21 is the basic loading resulting from a unit deflection of flap j. The summation, $\sum_{k=1}^{M}$, accounts for a M-surface configuration, where $\frac{b}{2}(k)$ refers to the half span of surface k. The $\Delta x(y)$ term refers to the longitudinal difference between the local airfoil section aerodynamic center and aircraft NP and is equal to $(x(y) - X_{NP})$. Finally, the C_{M_0} terms of Eq. 2.19 are the moments produced by the aircraft at zero lift and zero flap deflections, and incorporates the unflapped airfoil section pitching moments (*sections*) and moment produced by the unflapped basic lift (*basic*). These two terms are constant once the planform, twist, and airfoils are determined and lumped into one term, C_{M_0}, for the remainder of this work.

The upcoming section will discuss the *sections* and *basic* pitching moment in more detail, specifically in regard to how the flap angle distribution is defined. It will be shown that these two contributions to the pitching moment become critical design variables when solving for both minimum induced and profile drag.

2.2.2 Flap Angle Decomposition

Previous adaptive wing studies [12,47,48] by the N.C. State University Applied Aerodynamics Group have shown it advantageous to decompose the flap angles on a wing into a full-span deflection angle, labeled the mean angle, and a set of variation angles about the mean, labeled the variation angles. For a single surface, the two can be combined to form the aggregate flaps angles, as shown in Eq. 2.22 where the mean flap angle is designated $\bar{\delta}_f$ and the variation flap angles $\hat{\delta}_f$.

$$\{\delta_f\} = \bar{\delta}_f + \{\hat{\delta}_f\} \tag{2.22}$$

While the specific usage of these flaps will be shown later, it can be noted that for a single wing, the mean flap affects the lift in a manner similar to wing angle of attack, and can be used to change wing C_L without affecting the basic loading. And conversely, the variation angles can be used to alter the basic loading without changing wing C_L. It will be shown that the mean angle can be used to directly target profile-drag reduction while the variation angles play a critical role in induced-drag reduction via lift redistribution.

By defining the flap-angle distribution as the sum of mean and variation angles, it offers increased opportunity for changing the pitching moment about the aircraft neutral point. An an example, consider a single wing surface with the pitching moment variables $C_{M_{sections}}$ and $C_{M_{basic}}$ presented in the previous section. For a single surface, a mean flap deflection will mimic a change in wing angle of attack. Because a change in angle of attack does not affect the basic loading of a wing, it follows that a mean flap deflection will not alter the pitching moment due to basic loading ($C_{M_{basic}}$ variable). A similar argument would be that the aircraft neutral point is the location where pitching moment is independent of angle of attack. And because a mean flap deflection is similar to a change in angle of attack, the moment due to lift is unaffected. However, because a mean flap deflection changes the camber of the airfoil sections along the span, there will be a change in the $C_{M_{sections}}$ variable. Conversely, the variation angles are defined such that they do not contribute to wing C_L, and thus do not affect the additional loading of the wing. They will, however, directly influence the basic loading of the wing and thus the $C_{M_{basic}}$ variable. Because the variation angles also change the airfoil section of the wing, it follows that the variation angles will also affect $C_{M_{sections}}$. This is compensated for through the use of a weighting factor, which will be described in more detail in an upcoming section. Briefly, the weighting factor forces the summed influence on $C_{M_{sections}}$ of each individual variation flap to zero, thus effectively canceling the effect of each individual flap section change on the $C_{M_{sections}}$ variable.

It is important to note that the mean and variation flap angle distribution is defined per wing, and thus multiple surfaces present the opportunity for multiple mean flap variables. Displayed in Fig. 2.3 is an example of an adaptive three surface configuration using multiple TE flaps. The figure illustrates both the mean and variation flap angles, showing examples on the wing surface. This particular example is considered to have three mean flaps and eight variation flaps. While several mean flap variables offer added opportunity for aerodynamic design and drag reduction, the additional variables increase complexity when determining trim.

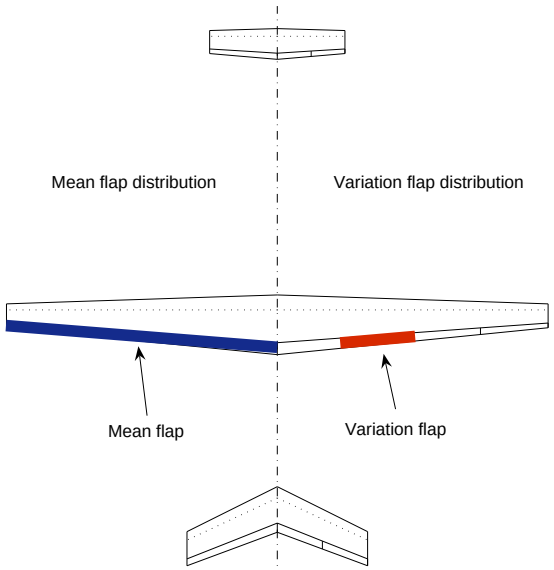

Figure 2.3: Multiple surface configuration illustrating mean and variation flap examples.

When multiple surfaces are considered, a single mean flap deflection may result in a change to the aircraft basic loading, and thus a change to $C_{M_{basic}}$. Care must be taken by the designer to properly distribute the flap variables and take into consideration pitching moment contributions from all sources when developing drag reduction schemes. While multiple surfaces somewhat alter the usage of the mean and variation flap angles, benefits can be shown supporting their use in developing the flap-optimization approaches.

2.2.3 Superposition of Lift Distributions

The advantage of using the superposition concept is that the net C_l distribution for a particular wing C_L can be posed in terms of the unknown flap angles.

$$C_l = C_L C_{la,1} + C_{lb,0} + \sum_{j=1}^{N} C_{lb,j}\delta_{f,j} \tag{2.23}$$

where, $C_{lb,0}$ is the basic C_l distribution of the unflapped wing system, and $C_{lb,j}$ is the basic C_l distribution of due to a unit deflection of flap j.

As shown in Sec. 2.1.2, $C_{D_{ind}}$ can be computed for superposed distributions, and can be expressed for all pairs of distributions of an N-flap system as follows:

$$\begin{aligned} C_{D_{ind}} = \quad & C_{D_{aa}} C_L^2 + C_{D_{00}} + (C_{D_{a0}} + C_{D_{0a}}) C_L + \\ & \sum_{j=1}^{N} (C_{D_{aj}} C_L + C_{D_{ja}} C_L + C_{D_{0j}} + C_{D_{j0}}) \delta_{f,j} + \\ & \sum_{i=1}^{N} \sum_{j=1}^{N} C_{D_{ij}} \delta_{f,i} \delta_{f,j} \end{aligned} \tag{2.24}$$

which can be written compactly in matrix notation as:

$$C_{D_{ind}} = \mathbf{f}^T \mathbf{D} \mathbf{f} \tag{2.25}$$

where $\mathbf{f}^T$ is the transpose of $\mathbf{f}$, and written as:

$$\mathbf{f}^T = \begin{bmatrix} C_L & 1 & \delta_{f,1} & \dots & \delta_{f,N} \end{bmatrix} \tag{2.26}$$

and the drag interdependency matrix, $\mathbf{D}$, is written as:

$$\begin{bmatrix} C_{D_{aa}} & C_{D_{a0}} & C_{D_{a1}} & \dots & C_{D_{aN}} \\ C_{D_{0a}} & C_{D_{00}} & C_{D_{01}} & \dots & C_{D_{0N}} \\ C_{D_{1a}} & C_{D_{10}} & C_{D_{11}} & \dots & C_{D_{1N}} \\ \vdots & \vdots & \vdots & & \vdots \\ C_{D_{Na}} & C_{D_{N0}} & C_{D_{N1}} & \dots & C_{D_{NN}} \end{bmatrix} \tag{2.27}$$

in which the elements are defined as in Sec. 2.1.2. The elements of the matrix shown in Eq. 2.27 can be precomputed using any wing analysis method, such as a vortex lattice, lifting line, or Weissinger-type, which outputs spanwise lift and spanwise downwash angle in the Trefftz plane. For the work described in this dissertation, the AVL[49] code was used for computing the necessary distributions.

Displayed in Fig. 2.4 is an example of a planar, tapered wing which illustrates the superposition concept. The wing has five evenly spaced flaps distributed along the trailing edge, each with a flap to chord ratio of 0.2. For this example, the wing is assumed to have zero geometric and aerodynamic twist, and zero camber. Plot (a) shows the $C_{la,1}$ distribution for the wing, as well as C_{lb} distributions (scaled 10 times, for clarity) for 1-deg flap deflections for (i) flap two ($\delta_{f,2}$) and (ii) flap five ($\delta_{f,5}$). Only the right hand side of the wing is shown due to symmetry.

The C_l distribution for this wing at $C_L = 0.5$ is displayed in plot (b) with $\delta_{f,2}$ deflected six degrees and $\delta_{f,5}$ deflected negative four degrees. The solution from direct analysis is compared with the solution from the superposition of (i) $C_{la,1}$ scaled by 0.5, (ii) C_{lb} for $\delta_{f,2}$ scaled by six, and (iii) C_{lb} for $\delta_{f,5}$ scaled by negative four. Following the methodology of the previous section, the variables $C_{M_{sections}}$ and $C_{M_{basic}}$ where calculated by integrating the individual distributions and found to be -0.00921 and 0.02957, respectively. These two components sum up to a total moment about the NP of 0.02036. Direct analysis for the configuration with $\delta_{f,2}$ deflected six degrees and $\delta_{f,5}$ deflected negative four degrees predicts a moment about the NP equal to 0.02080. Further, when induced drag is considered, superposition of lift distributions for this example gives a value of $C_{D_{ind}} = 0.00715$. The direct analysis $C_{D_{ind}}$ value is 0.00711. This very good agreement between direct analysis and superposition for both $C_{M_{NP}}$ and $C_{D_{ind}}$ highlights the capabilities provided by the superposition method.

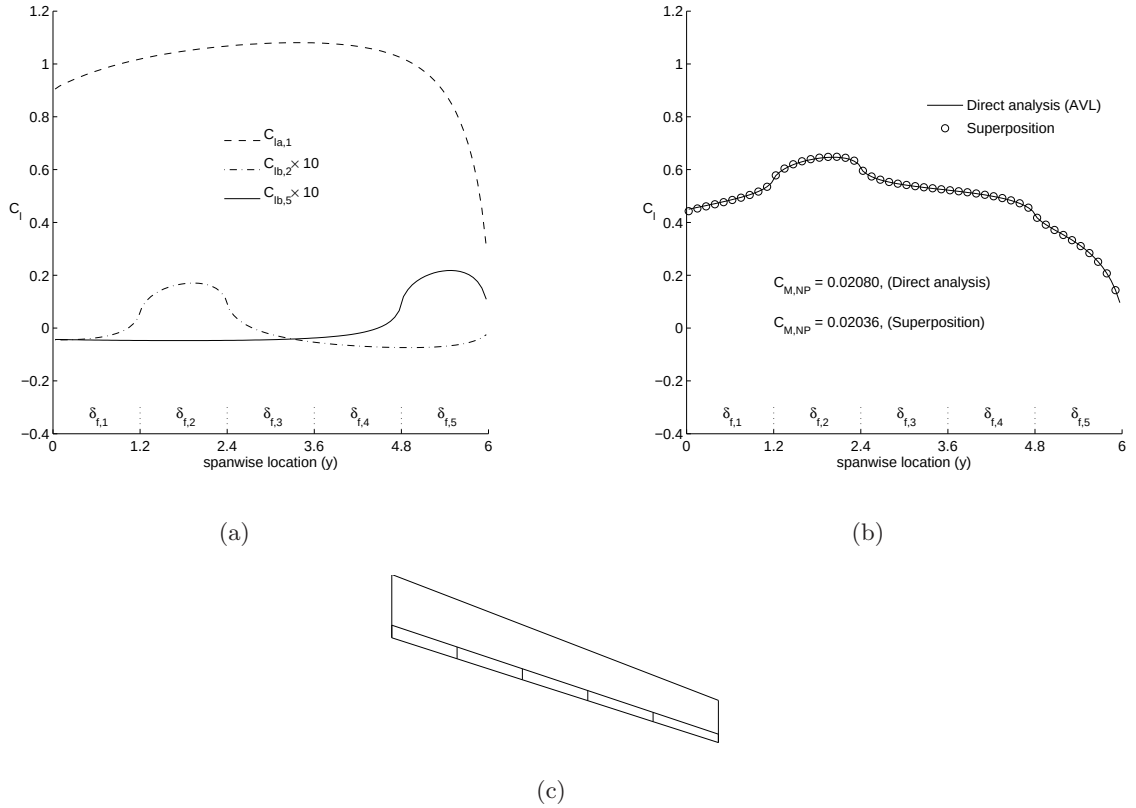

(a) (b)

(c)

Figure 2.4: Illustration of superposition: (a) basic and additional C_l distributions and (b) C_l due to superposition compared with C_l from direct analysis. $C_{M,NP} = 0.02036$ from superposition and $C_{M,NP} = 0.02080$ from direct analysis. (c) RHS of wing showing multiple TE flap geometry.

2.2.4 Flap Angles for Unconstrained Minimum Induced Drag

A necessary condition for a minimum in the induced drag is that the first derivatives of the $C_{D_{ind}}$ with respect to all the flap angles should be zero. As an illustration, the derivative with respect to flap j is set equal to zero as follows:

$$\frac{\partial C_{D_{ind}}}{\partial \delta_{f,j}} = (C_{D_{aj}} + C_{D_{ja}})C_L + (C_{D_{0j}} + C_{D_{j0}}) + \sum_{i=1}^{N}(C_{D_{ij}} + C_{D_{ji}})\delta_{f,i} = 0 \tag{2.28}$$

The resulting system of N equations can be expressed compactly as:

$$\begin{bmatrix} C_{D_{11}} & \dots & C_{D_{1N}} \\ \vdots & & \vdots \\ C_{D_{N1}} & \dots & C_{D_{NN}} \end{bmatrix} \begin{Bmatrix} \delta_{f,1} \\ \vdots \\ \delta_{f,N} \end{Bmatrix} = - \begin{Bmatrix} C_L C_{D_{a1}} + C_{D_{01}} \\ \vdots \\ C_L C_{D_{aN}} + C_{D_{0N}} \end{Bmatrix} \tag{2.29}$$

in which Munk's mutual-drag theorem has been used to simplify the vector on the right hand side.

In many cases, when the multiple flaps occupy the entire span of the wing, the square matrix on the LHS of Eq. 2.29 is singular and has a rank $(N-1)$ for a wing with N flaps. In other words, the N equations are not linearly independent. The reason for this behavior is explained by considering a wing with all flaps having the same flap-to-chord ratio. For this wing, the basic loading due to a 1-degree deflection of flap j can be replicated exactly by instead deflecting all the other flaps to -1 degrees. This lack of linear independence poses a problem for the solution of Eq. 2.29, because there are an infinite number of solutions for the optimum flap angles. Clearly, an additional equation is needed to solve the system.

Discussed in Sec. 2.2.2 was the decomposition of a set of trailing-edge flap deflections into two components: (1) a mean angle, and (2) a set of variation angles. This relationship helps to solve the linear independence problem stated previously for a wing with flaps along its entire span. By definition, the variation flap-angle distribution does not contribute to the wing C_L. This offers the opportunity to construct an equation which sets the weighted mean of the variation flap angles to zero, as follows:

$$W_1 \hat{\delta}_{f,1} + \ldots + W_N \hat{\delta}_{f,N} = 0 \tag{2.30}$$

where the weighting factor for each flap angle takes into consideration the relative influence of that flap on the lift of the wing. For a planar wing, the weighting factor for a given flap may be determined by simply taking the ratio of the area of the wing affected by the flap to the total wing area. An alternate and more rigorous approach that is also applicable to non-planar geometries can be developed, especially when using an analysis method for determining the elements of the $\mathbf{D}$ matrix. In this approach, the weighting factor for a given flap is the ratio of the angle of attack for the basic loading with a unit deflection of this flap to the sum of the basic-loading angles of attack for all the flaps, as follows:

$$W_j = \frac{\alpha_{b,j}}{\alpha_{b,1} + \ldots + \alpha_{b,N}} \tag{2.31}$$

where, $\alpha_{b,j}$ is the angle-of-attack for basic loading with 1-degree angle of flap j. These angles-of-attack can be determined as a part of the same analysis used in the computation of the elements of the **D** matrix without the need for any additional analysis. With the addition of the equation to Eq. 2.29, the system of equations for a solution of the variation flap angles for minimization of induced drag becomes:

$$\begin{bmatrix} C_{D_{11}} & \dots & C_{D_{1N}} \\ \vdots & & \vdots \\ C_{D_{N1}} & \dots & C_{D_{NN}} \\ W_1 & \dots & W_N \end{bmatrix} \begin{Bmatrix} \hat{\delta}_{f,1} \\ \vdots \\ \hat{\delta}_{f,N} \end{Bmatrix} = - \begin{Bmatrix} C_L C_{D_{a1}} + C_{D_{01}} \\ \vdots \\ C_L C_{D_{aN}} + C_{D_{0N}} \\ 0 \end{Bmatrix} \tag{2.32}$$

As seen, Eq. 2.32 has $N + 1$ equations but only N unknowns. This system can be solved either by eliminating any one of the first N equations or by solving the over-determined system using a least-squares approach. Note also that the variation flap angles have been used in Eq. 2.32, because the mean flap angle does not affect the basic loading and hence does not affect the $C_{D_{ind}}$ of a single wing.

While the above equation displays a solution for variation flap angles resulting in minimum induced drag, it should be noted that the method can easily be adapted to solve for flap variables other then variation flaps. For example, if multiple lifting surfaces exist and mean flaps exist on each surface, then these mean flap variables can be substituted provided the drag interdependency and RHS matrix are constructed appropriately. Such examples will be studied in upcoming sections, while here only the fundamental method is discussed.

2.2.5 Flap Angles for Minimum Trimmed Induced Drag

Discussed in Sections 2.2.1 and 2.2.2 are the relationships between flap deflections and aircraft pitching moment. It was stated that, for this problem, there are two types of flap deflections, mean and variation flaps, and that each flap variable presents specific opportunities to affect that aircraft pitching moment. The methodology of the current section seeks to solve for minimum induced drag with a pitching moment constraint. While the multiple flap angles present multiple methods for solving the problem, for now the mean flap angle will be ignored and the variation flaps will be the focus. Later drag reduction schemes will show the need for constraining the variation flap angles.

Previous sections discussed aircraft pitching moment and trim for a configuration, and have derived expressions for determining the pitching moment of an adaptive configuration using multiple TE flaps. Further, background information (Sec. 2.1.4) has been provided for finding relative minima of multi-variable functions with constraints. These ideas can be combined for the purposes of this section, with the constraint introduced as the pitching moment about the aircraft NP which satisfies the trim requirement for a desired SM and C_L. Introduced earlier as Eq. 2.19 was the total pitching moment about the aircraft NP for any given flap deflections. This equation becomes the constraint, and is set equal to zero, $g(\delta_f) = 0$, leading to Eq. 2.33.

$$g(\delta_f) = \sum_{j=1}^{N} C_{M_j}\delta_{f,j} + C_{M_0} - (SM \times C_L) = 0 \tag{2.33}$$

In the above equation the C_{M_j} term includes the moment contribution produced by a unit deflection of flap j, which occurs both from a change in airfoil section pitching moment and from a change in basic loading. These terms were labeled $C_{M_{sections,j}}$ and $C_{M_{basic,j}}$ and were expanded in Eqs. 2.20, and 2.21.

For a configuration with N flaps, the flap angles resulting in minimum trimmed induced drag can be obtained by solving the system of linear equations expressed in matrix form as:

$$\begin{bmatrix} C_{D_{11}} & C_{D_{12}} & \dots & C_{D_{1N}} & C_{M_1} \\ C_{D_{21}} & C_{D_{22}} & \dots & C_{D_{2N}} & C_{M_2} \\ \vdots & \vdots & & \vdots & \vdots \\ C_{D_{N1}} & C_{D_{N2}} & \dots & C_{D_{NN}} & C_{M_N} \\ C_{M_1} & C_{M_2} & \dots & C_{M_N} & 0 \end{bmatrix} \begin{Bmatrix} \delta_{f,1} \\ \delta_{f,2} \\ \vdots \\ \delta_{f,N} \\ \lambda/2 \end{Bmatrix} = - \begin{Bmatrix} C_{D_{a1}}C_L + C_{D_{01}} \\ C_{D_{a2}}C_L + C_{D_{02}} \\ \vdots \\ C_{D_{aN}}C_L + C_{D_{0N}} \\ -(SM \times C_L) + C_{M_0} \end{Bmatrix} \tag{2.34}$$

In the above equation the flap angles to be optimized can be variation flaps, mean flaps, or a combination of the two. It is only necessary that the terms of the drag interdependency matrix and constraint equation be calculated and stored appropriately. If only variation angles are to be optimized, then the weighting equation displayed previously in Eq. 2.30 can be inserted, reducing the contribution from the airfoil *section* pitching moment. While the weighting equation forces zero change in surface C_L, not airfoil *section* pitching moment, the small positive and negative flap deflection combinations necessary to zero out the C_L will act similar for zeroing out the airfoil *section* pitching moment contribution. And any small

pitching moment that results can be negated with slight mean flap deflections. Upcoming sections will show how the weighting equation can be used to simplify the constraint value to be the *basic* pitching moment contribution alone. The weighting equation is shown inserted as the $(N+1)^{th}$ row of Eq. 2.35.

$$\begin{bmatrix} C_{D_{11}} & C_{D_{12}} & \dots & C_{D_{1N}} & C_{M_1} \\ C_{D_{21}} & C_{D_{22}} & \dots & C_{D_{2N}} & C_{M_2} \\ \vdots & \vdots & & \vdots & \vdots \\ C_{D_{N1}} & C_{D_{N2}} & \dots & C_{D_{NN}} & C_{M_N} \\ W_1 & W_2 & \dots & W_N & 0 \\ C_{M_1} & C_{M_2} & \dots & C_{M_N} & 0 \end{bmatrix} \begin{Bmatrix} \hat{\delta}_{f,1} \\ \hat{\delta}_{f,2} \\ \vdots \\ \hat{\delta}_{f,N} \\ \lambda/2 \end{Bmatrix} = - \begin{Bmatrix} C_{D_{a1}} C_L + C_{D_{01}} \\ C_{D_{a2}} C_L + C_{D_{02}} \\ \vdots \\ C_{D_{aN}} C_L + C_{D_{0N}} \\ 0 \\ -(SM \times C_L) + C_{M_0} \end{Bmatrix} \tag{2.35}$$

Solution of the overdetermined system results in variation flap angles producing minimum induced drag and trim. Upcoming sections will show how this can be used in combination with other techniques for other drag reduction schemes.

2.2.6 Flap Angles for Minimum Profile Drag

Discussed in Sec. 2.1.6 were cruise flaps and their ability to achieve lower profile drag for NLF airfoils. A primary benefit for decomposing the flap angle distribution as in Sec. 2.2.2 is that a deflection of the mean flap is the same as deflecting a full-span flap, which is similar to a TE flap on an airfoil. Thus, the mean flap can be used similar to a cruise flap for shifting the LDR of the wing sections, and allows for profile drag reduction.

For profile drag reduction, a method for setting the mean flap $\bar{\delta}_f$ for a given wing C_L needs to be in place to ensure that the majority of the wing sections are operating within the low-drag ranges of their respective sections. This is achieved by linear interpolation between ($C_{l_{low}}$,$\delta_{f_{min}}$) and ($C_{l_{up}}$,$\delta_{f_{max}}$) for the operating C_L, as follows:

$$\bar{\delta}_f = \delta_{f_{min}} + \frac{C_L - C_{l_{low}}}{C_{l_{up}} - C_{l_{low}}} (\delta_{f_{max}} - \delta_{f_{min}}) \tag{2.36}$$

While this linear variation of $\bar{\delta}_f$ with C_L works well for wings with NLF airfoils having well-defined drag buckets, other variations may be desirable for airfoils such as those used on low Reynolds number aircraft. By simply providing airfoil-specific values for ($C_{l_{low}}$,$\delta_{f_{min}}$) and ($C_{l_{up}}$,$\delta_{f_{max}}$), it becomes an easy task to determine a mean flap deflection angle for ensuring low profile drag.

Considering the system of multiple flap variables presented earlier for a single surface, if the mean flap angle is fixed at a value for drag-bucket control (profile drag optimization), then the variation flap angles can be constrained to produce minimum induced drag and trim by utilizing the methodology presented in Sec. 2.2.5. However, if multiple mean flap variables exist, for example on a multiple surface configuration, then it is possible for the mean flap variables to be solved using the same matrix optimization routine. Consider a system of flap variables, which could be mean or variation flaps. Fixing a single flap variable for the purposes of reducing profile drag results in additional known values to the system. The flap variable that is known will be removed from the variable vector, along with a row and column from the drag interdependency matrix. The removed column multiplied by the known flap value is then subtracted from the RHS matrix.

Displayed in Eq. 2.37 an example of a system containing several flap variables, of which flap j has been fixed to be a value of $X_{f,j}$. As shown, $\delta_{f,j}$ has been removed from the variable vector as well as the row and column from the drag interdependency matrix associated with $\delta_{f,j}$. The RHS shows how the fixed flap value $X_{f,j}$ is introduced back into the system. For this example, the order of the system reduces by one and the remaining flap variables can still be optimized for minimum $C_{D_{ind}}$ and trim.

$$\begin{bmatrix} C_{D_{11}} & \cdots & C_{D_{1j-1}} & C_{D_{1j+1}} & \cdots & C_{D_{1N}} & C_{M_1} \\ \vdots & & \vdots & \vdots & & \vdots & \vdots \\ C_{D_{j-11}} & \cdots & C_{D_{j-1j-1}} & C_{D_{j-1j+1}} & \cdots & C_{D_{j-1N}} & C_{M_{j-1}} \\ C_{D_{j+11}} & \cdots & C_{D_{j+1j-1}} & C_{D_{j+1j+1}} & \cdots & C_{D_{j+1N}} & C_{M_{j+1}} \\ \vdots & & \vdots & \vdots & & \vdots & \vdots \\ C_{D_{N1}} & \cdots & C_{D_{Nj-1}} & C_{D_{Nj+1}} & \cdots & C_{D_{NN}} & C_{M_N} \\ C_{M_1} & \cdots & C_{M_{j-1}} & C_{M_{j+1}} & \cdots & C_{M_N} & 0 \end{bmatrix} \begin{Bmatrix} \delta_{f,1} \\ \vdots \\ \delta_{f,j-1} \\ \delta_{f,j+1} \\ \vdots \\ \delta_{f,N} \\ \lambda/2 \end{Bmatrix} =$$

$$-\begin{Bmatrix} C_{D_{a1}} C_L + C_{D_{01}} \\ \vdots \\ C_{D_{aj-1}} C_L + C_{D_{0j-1}} \\ C_{D_{aj+1}} C_L + C_{D_{0j+1}} \\ \vdots \\ C_{D_{aN}} C_L + C_{D_{0N}} \\ -SM \times C_L + C_{M_0} \end{Bmatrix} - \begin{Bmatrix} C_{D_{1j}} \\ \vdots \\ C_{D_{j-1j}} \\ C_{D_{j+1j}} \\ \vdots \\ C_{D_{Nj}} \\ C_{M_j} \end{Bmatrix} [\, X_{f,j} \,] \tag{2.37}$$

The preceding methodology shows the flexibility of the drag reduction system for reducing profile drag. The Results sections will explore different types of configurations and utilize the methods presented to provide insight into aerodynamic design possibilities.

2.2.7 Drag Polar Approximation Routine

The previously introduced methodology has shown capabilities for minimizing both induced and profile drag with a trim constraint. While these methods are powerful aerodynamic analysis and design tools, there was a significant shortcoming in the method for profile drag reduction. Because the drag polar of an airfoil changes with flap angle and Reynolds number, it is difficult to accurately predict specific values of profile drag for a wing. The methods for minimizing profile drag have focused on exploiting linear trends of the low-drag ranges of NLF airfoils, and Sec. 2.2.6 has described how to ensure minimum profile drag is achieved for a wing, however it does not give a profile drag value. That value is only achieved once the optimum flap angles are determined and an airfoil analysis method such as XFOIL can be utilized to predict the drag polars as a post-processing exercise. On the other hand, induced drag results from the lift distribution alone. The methodology has

shown that by pre-computing and storing the basic and additional lift distributions for a multiple flap configuration, specific induced drag values can be solved for directly with flap angles. Therefore, it becomes desirable to develop a method for approximating the drag polar using curve fit, and using these curve fits for predicting the drag polar of an airfoil to be used directly by the optimization scheme, thus increasing the design capabilities.

For the current work, the two most important factors influencing the drag polar of an airfoil are flap angle and Reynolds number. Section 2.1.6 discussed the effect that flap deflection has on NLF airfoils, shifting the drag bucket to higher and lower C_l values and effectively increasing the low-drag range that the airfoil can operate in. Reynolds number effects on the drag bucket differ from flap effects in that changes in Reynolds number typically act to shrink or expand the drag bucket, as well as shifting it to higher or lower drag values. Figure 2.5 displays the resulting change to the drag bucket of a NLF airfoil with Reynolds number.

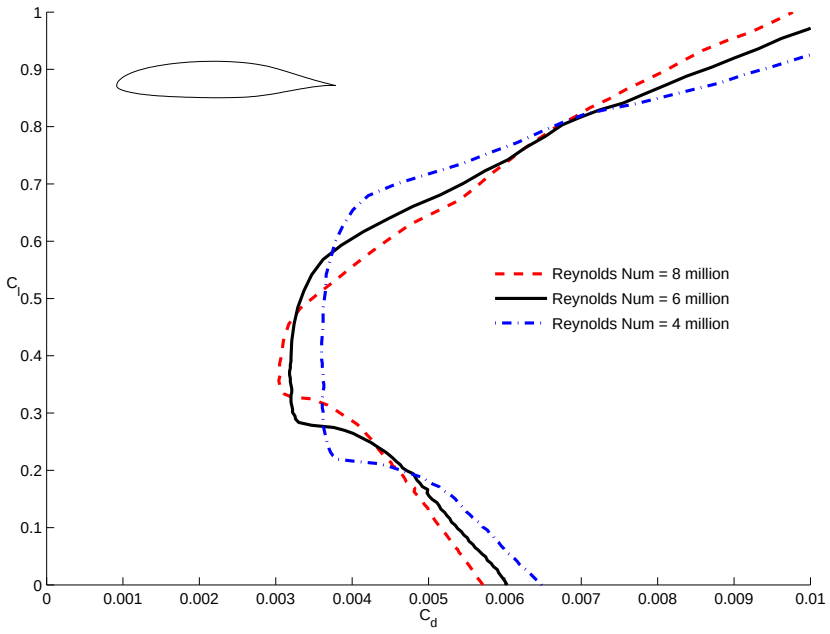

Figure 2.5: Change in airfoil drag bucket with Reynolds number.

The figure shows that as Reynolds number increases, the drag bucket shrinks to encompass a smaller C_l range and also shifts to lower minimum drag values. The shift to lower minimum

drag values is explained by the classic result that local skin friction coefficient decreases with increasing Reynolds number for incompressible laminar flow. Thus, the Reynolds number increase results in the drag bucket shifting left on the $C_d - C_l$ plot. The shrinking of the drag bucket is a consequence of decreasing stability of a laminar boundary layer with increasing Reynolds number, resulting in an increased tendency for the laminar boundary layer to transition to turbulent boundary layer at higher Reynolds numbers. At higher Reynolds numbers, even a small deviation of the operating C_l from the ideal C_l results in movement of the transition location towards the leading edge, and increase in C_d.

The simple example displayed in Fig. 2.5 introduces several difficulties for approximating a drag polar for an airfoil. Flow properties such as boundary layer transition and separation location are difficult to predict accurately for a single example case without considering flap angle changes and Reynolds number effects. Further, the relationships discussed above tend to be non-linear, as small changes in Reynolds number can cause large drag changes, and are very dependent on airfoil design. For example, NLF airfoils are typically designed for a single operating Reynolds number and C_l, and thus the pronounced low-drag range surrounding its design location. When operating outside of this condition, the airfoil will mostly likely incur large drag penalties.

Adding further complication are the regions of the drag polar that exist outside of the drag bucket. These regions are as important as the drag bucket, as design examples may not be focusing on low profile drag, indicating that much of the wing will be operating in the regions outside the drag bucket. These regions are non-linear, they change with Reynolds number and flap angle, and are very specific to airfoil design. Each of these facts needs to be considered for proper design. Figure 2.6 displays the regions of the drag polar graphically, and splits it up into three distinct regions: (1) the upper region, (2) the drag bucket, and (3) the lower region.

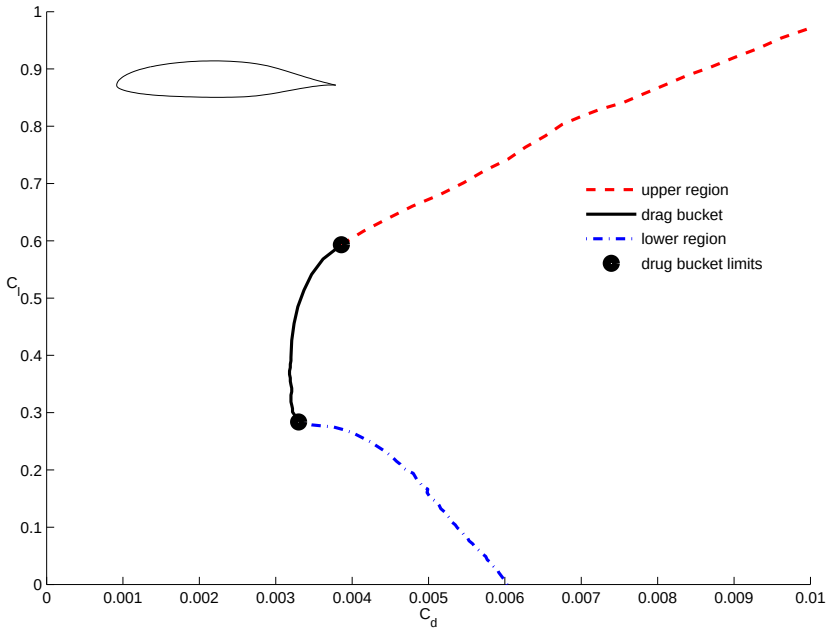

Figure 2.6: Graphical representation of drag polar regions for an NLF airfoil. Re = 6e6 and no flap deflection.

The routine for modeling the drag polar designed for this work focuses on the three regions displayed in Fig. 2.6 and builds them independently from a common starting point. Because the characteristics of the drag polar are very dependent on airfoil geometry, several drag polars are created for an airfoil to define how the polars change with flap angle and Reynolds number. These drag polars are selected to encompass the operating region typical of the design problem. Displayed in Fig. 2.7 is an example of a set of polar files that are provided as inputs to the curve-fit development routine. Plots (a), (c), and (e) provide information for how the drag polars change with flap angle, while plots (b), (c), and (d) provide information for how the drag polars change with Reynolds number. The drag bucket limits for each drag polar are provided as input separately. Section 2.1.6 mentioned that cruise flap effectiveness tends to be limited to ± 10 degrees deflection, and therefore plots (a) and (e) were chosen with these limits. The Reynolds number for this example varies from 2- to 10-million, and were selected based on values that are expected for the particular design problem.

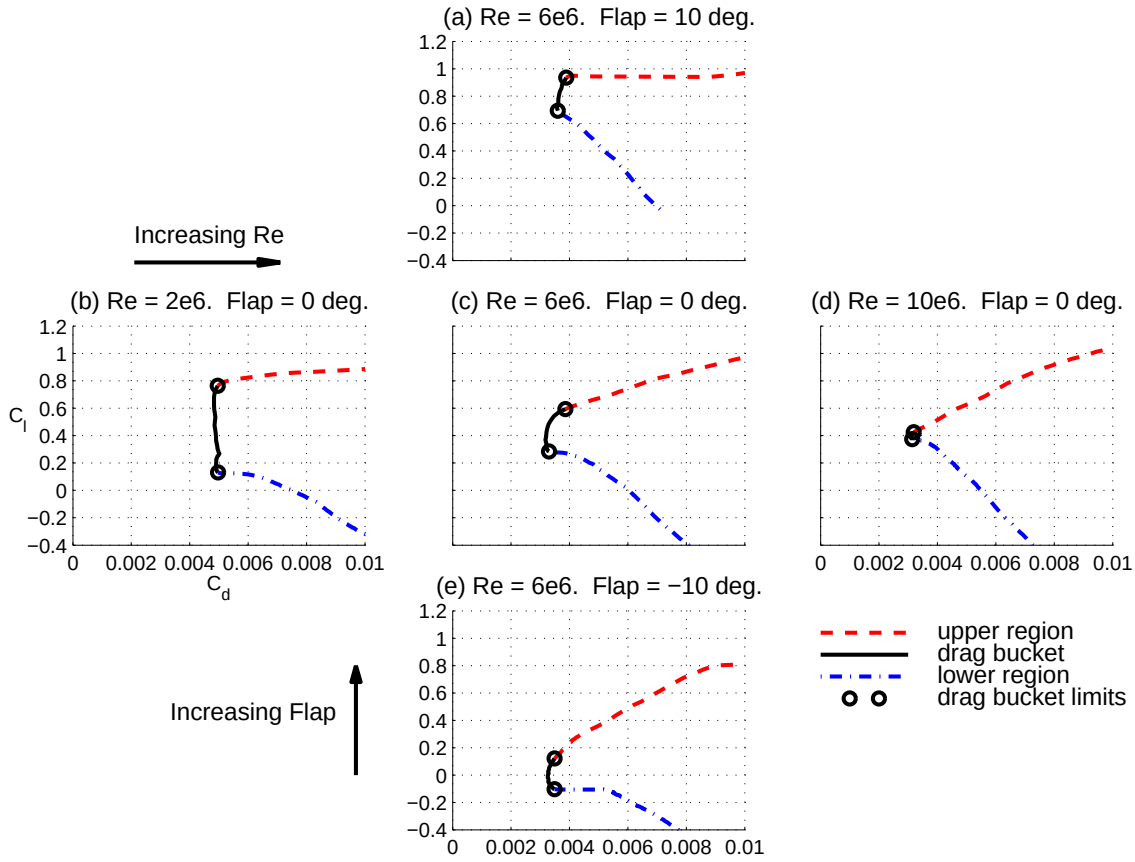

Figure 2.7: Example input polar files for the drag polar approximation routine. Plots (a), (c), and (e) illustrate changes in TE flap angle. Plots (b), (c), and (d) illustrate changes in Reynolds number. The different drag polar regions are highlighted.

The first step for constructing the drag polar is to determine a starting point on the $C_d - C_l$ axis, which is decided to be the center of the drag bucket. For a NLF airfoil, the center of the drag bucket is typically designed to be the location of minimum drag. Reynolds number has very non-linear effects on the drag of an airfoil, and thus unpredictably effects the specific placement of the drag polar on the $C_d - C_l$ axis. However, plots (b), (c), and (d) of Fig. 2.7 show that as Reynolds number changes, the drag buckets are largely centered around the same C_l value ($C_l = 0.4$ in this example). Thus, constant C_l value can be used for each flap angle independent of Reynolds number which will relate to the center of the drag bucket. The airfoil can analyzed at this C_l value for several Reynolds numbers to gain a more accurate model for minimum drag location. For the displayed example, airfoil drag is

computed for Reynolds numbers spanning 1-million to 11-million in increments of 1-million, or 11 total Reynolds numbers. This was done for each flap-angle deflection (-10 degrees, 0 degrees, 10 degrees), thus resulting 33 total additional analysis runs. While this might seem like a time consuming process, because only minimum drag approximations are required, the entire drag polars do not need to be predicted for each of the 33 runs. Instead, the airfoil is only analyzed at 33 different (Re,C_l) points, and C_d is stored for each. If an airfoil analysis code such as XFOIL is used, this process takes little time. Linear interpolation is used to approximate how the (C_d,C_l) location of the drag bucket center changes with both flap angle and Reynolds number. This value, labeled $(C_d, C_l)_{center}$, becomes the starting point for constructing the drag polar and positions the plot.

The next step for constructing the drag polar is to define its shape. Highlighted in Fig. 2.7 are the three regions of interest for each drag polar, namely the upper region, drag bucket, and lower region. It is necessary to construct each of these regions for an airfoil given a flap-angle deflection and Reynolds number. Each region is constructed in a similar manor, beginning by isolating the data from the region for each drag polar provided as input. The data from the drag polars are normalized to span a common area, then 6^{th} order polynomials are fit to each line. The coefficients for the polynomials are stored, and linear interpolation is used for determining how the coefficients change with both flap angle and Reynolds number. Once the polynomial coefficients are interpolated for a specific case, they can be used to produce a line which represents that region of the drag polar. This is done independently for each of the three regions, then pieced together to form the final drag polar. The drag polar is positioned such that the center of the drag bucket corresponds to the $(C_d, C_l)_{center}$ value interpolated previously. Matlab is used in this work for fitting the polynomial coefficients and for the linear interpolation.

The optimization method for induced drag is powerful in that once the basic and additional loading information is created, it can be stored and reused for future analysis. Similarly, the method provided here for predicting the drag polar of an airfoil makes use of a one-time process of creating specific data files that can be reused for any configuration using that airfoil. The ability to predict the drag polar for an airfoil, given Reynolds number and flap angle, greatly increases the design capabilities of the routine, as profile drag can be optimized with along with induced drag to insure minimum total drag. Figure 2.8 illustrates an example adaptive wing and displays drag polars predicted by both XFOIL and

the approximate curve-fit method discussed here for comparison. This particular example is a single planar wing with five trailing edge flaps distributed evenly along its span, and is analyzed for a wing $C_L = 0.4$. The top plot indicates flap angle for each section, and Reynolds number is displayed below each drag polar. Reynolds number is changing in the spanwise direction due to wing taper. As shown, the approximated drag polars match well with the drag polars predicted by XFOIL, indicating the success of the method. The profile component of C_D predicted for this wing using the XFOIL drag polars is $3.335e^{-3}$, while the value when using the approximate drag polars is $3.219e^{-3}$, providing further validation. When the necessary data files are pre-computed, creation of the approximate drag polars take insignificant amounts of time to compute. Conversely, producing the five polar plots for this example using XFOIL takes several minutes on a fast computer.

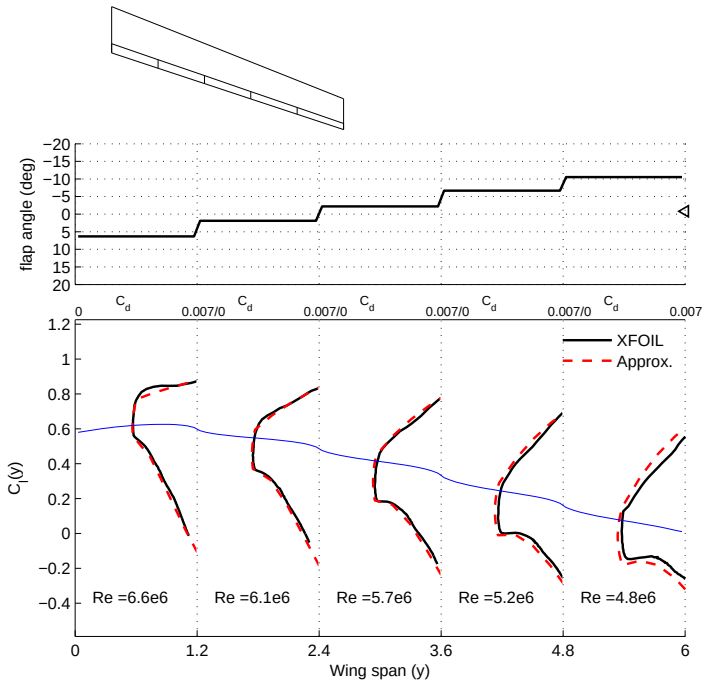

Figure 2.8: Example displaying drag polars predicted by the approximate method versus drag polars predicted by XFOIL. RHS of wing geometry with multiple TE flaps also shown.

2.2.8 Flap Angles for Minimum Total Drag

Total drag is defined in the current work as the sum of the profile and induced components of drag. Methodology has been previously described for minimizing both induced and profile drag independently. While these methods provide much opportunity for aerodynamic insight and analysis, often these drag components present trade-offs in terms of total drag. If TE flap angles are set so that induced drag is minimized, for example, profile drag may suffer due to the airfoil sections operating outside their drag buckets. Similarly, if the flaps are determined to ensure the majority of the wing is operating in the low-drag range, the lift distribution may be skewed from optimal such that induced drag significantly suffers. It becomes desirable, then, to create a method that chooses flap angles resulting in minimum total drag.

The previous methodology of Secs. 2.1.2 and 2.1.3 provide the opportunity for a drag function to be created which gives total drag for a configuration geometry, C_L, and series of TE flap angles. Provided the basic and additional loading information, induced drag $C_{D_{ind}}$ can be solved for given flap deflection angles and C_L using Eq. 2.24. The same flap angles are provided as input to the drag polar model of Sec. 2.2.7 and used to approximate airfoil section drag polars. These drag polars are interpolated using the spanwise lift distribution to form the profile drag component $C_{d,pro}(y)$ of Eq. 2.12 and solve for profile drag $C_{D_{pro}}$. The induced and profile drag components are summed as in Eq. 2.38 to produce total drag $C_{D_{tot}}$.

$$C_{D_{tot}} = C_{D_{ind}} + C_{D_{pro}} \tag{2.38}$$

A function which takes TE flap angles and C_L as inputs and outputs total drag can be used with a nonlinear optimizer for minimizing total drag with a specified constraint on the $C_{M_{NP}}$. The optimizer used by this work is the built-in Matlab optimizer function fmincon, which finds minimums of nonlinear multivariable functions with equality constraints.

Using an optimizer for determining flap angles introduces limitations on the solution. First of all, very little aerodynamic insight can be gained from the solutions, as the flap angles are not set based on any specific aerodynamic goal. The lift distribution and airfoil sections, for example, are allowed to be altered by the optimizer and solutions result that present no correlation between these variables and drag reduction. In fact, perhaps the only analysis conclusion drawn might be that is that total drag is minimized by the

optimized flap angles. Even this should be questioned, however, as a second important limitation of optimizers is their sensitivity to starting values. For this problem, starting values for the flap angles need to be provided to the optimizer. Upcoming sections will show that the optimizer is reliant on the starting flap angles as they greatly affect results. The sensitivity can be explained by considering the drag polar approximation routine described in the previous subsection. That routine uses curve-fit techniques to build a drag polar in three sections. Often times, especially for cases with particularly large and small flap deflection angles, sharp corners exist on the drag polars at the junctions of the three sections. The sharp transition areas can cause the optimizer to get stuck, and leads to the optimizer finding minimums near to the starting values. While these limitations exist, the optimized solutions do offer valuable comparisons for the drag reduction approaches which focus on specific drag components, as they provide a value for lowest possible total drag.

Chapter 3

Optimal Lift Distributions for a Tailless Aircraft

Presented in this chapter are descriptions and examples of how the methodology of Chapter 2 can be applied to a tailless configuration. Section 3.1 describes specific drag reduction schemes that are derived from the previous methodology, and includes subsections dedicated to induced drag reduction, profile drag reduction, and total drag reduction. Section 3.2 details the configuration information for the adaptive tailless aircraft used in this chapter for illustrating the methodology. Section 3.3 presents induced, profile, and total drag results for a range of C_L values for different variations of the tailless aircraft configuration in the first four subsections. Also displayed are flap-angle solutions and spanwise lift distribution examples for each configuration variation. The final subsection presents an optimizer starting value sensitivity study. Section 3.4 presents conclusions pertaining to the drag reduction schemes applied to a tailless configuration.

3.1 Drag Reduction Schemes for a Tailless Aircraft

3.1.1 $C_{D_{ind}}$ Minimization (Scheme A)

The first drag reduction scheme presented here is intended to minimize induced drag $C_{D_{ind}}$. Aerodynamic theory provides the classical result for minimum induced drag of a planar wing to occur when the spanwase loading, or spanwise lift coefficient C_l times the chord

distribution c, is elliptical in shape. Therefore, the drag reduction scheme is intended to produce near-elliptical loading on the wing using the flaps.

Section 2.2.2 decomposed the TE flap angle distribution into two unique flap types, a full-span mean flap and a set of variation flaps. For a tailless aircraft these flap variables offer different methods for affecting both the aircraft lift distribution and pitching moment about the neutral point. A deflection of the mean flap is comparable to a change in angle-of-attack, and thus results in no change to the basic loading of the wing. Therefore, elliptical loading can be achieved by changing the variation flaps alone. The method for determining flap angles resulting in minimum induced drag was displayed previously in Eq. 2.32, and re-displayed here:

$$\begin{bmatrix} C_{D_{11}} & \dots & C_{D_{1N}} \\ \vdots & & \vdots \\ C_{D_{N1}} & \dots & C_{D_{NN}} \\ W_1 & \dots & W_N \end{bmatrix} \begin{Bmatrix} \hat{\delta}_{f,1} \\ \vdots \\ \hat{\delta}_{f,N} \end{Bmatrix} = - \begin{Bmatrix} C_L C_{D_{a1}} + C_{D_{01}} \\ \vdots \\ C_L C_{D_{aN}} + C_{D_{0N}} \\ 0 \end{Bmatrix} \tag{3.1}$$

where the $(N+1)^{th}$ row is the weighting function presented in Eq. 2.30.

For this drag reduction scheme, there is no pitching moment constraint as purely elliptical loading is desired. The variation flap vector displayed in Eq. 3.1 is solved, resulting in variation flap settings that produce elliptical loading. These flap angles contribute to a pitching moment, which can be solved using the variables $C_{M_{sections}}$ and $C_{M_{basic}}$ presented in Sec. 2.2.1. For trim, a desired SM is given and $C_{M_{NP}}$ is known. The mean flap can then be altered to achieve this value, as a mean-flap deflection will not upset the basic loading of the wing, but will produce a change to $C_{M_{sections}}$. Lastly, α is varied to achieve desired C_L.

By following these steps, it is possible to create a tailless aircraft that maintains elliptical loading (minimum induced drag), longitudinal trim, and desired lift. It should be noted that no constraints were placed on the value of the flap settings or on α. It is assumed that the airfoil design, twist distribution, etc., of an aircraft using this system will be such that extreme flap angles will not be necessary. Minimizing induced drag is typically desirable at high-C_L flight conditions such as for long range, longer endurance, and for climb.

3.1.2 $C_{D_{pro}}$ Minimization (Scheme B)

Profile drag $C_{D_{pro}}$ reduction is primarily focused on reducing skin friction, and ensuring that the wing is operating in the low-drag ranges of the airfoil sections becomes the goal of this drag reduction scheme. A mean flap deflection of a wing is similar to an airfoil flap deflection, and can be used for drag bucket control. For this drag reduction scheme, the mean flap is set to ensure minimum profile drag then the variation flaps are set to provide the best induced drag while achieving trim.

To determine the mean flap deflection resulting in minimum profile drag, the methods of Sec. 2.2.6 are used, specifically Eq. 2.36, reproduced here:

$$\bar{\delta}_f = \delta_{f_{min}} + \frac{C_L - C_{l_{low}}}{C_{l_{up}} - C_{l_{low}}}(\delta_{f_{max}} - \delta_{f_{min}}) \tag{3.2}$$

This equation uses linear interpolation for determining $\bar{\delta}_f$, and works well for wings with NLF airfoils having well-defined drag buckets. The requirement for trim at a given SM determines the value of $C_{M_{NP}}$. Because the mean flap deflection does not influence the basic loading of the wing, the only pitching moment contribution will be to the $C_{M_{sections}}$ variable. The mean flap determines the value of $C_{M_{sections}}$, which can be subtracted from $C_{M_{NP}}$ along with the zero-lift moment C_{M_0} determined by the configuration geometry, shown in Eq. 3.3.

$$C_{M_{basic}} = C_{M_{NP}} - (C_{M_{sections}} + C_{M_0}) \tag{3.3}$$

This $C_{M_{basic}}$ is the moment that has to be generated by the basic lift to trim, and, is inserted as a constraint on the variation flaps.

$$\begin{bmatrix} C_{D_{11}} & C_{D_{12}} & \dots & C_{D_{1N}} & C_{M_{b,1}} \\ C_{D_{21}} & C_{D_{22}} & \dots & C_{D_{2N}} & C_{M_{b,2}} \\ \vdots & \vdots & & \vdots & \vdots \\ C_{D_{N1}} & C_{D_{N2}} & \dots & C_{D_{NN}} & C_{M_{b,N}} \\ W_1 & W_2 & \dots & W_N & 0 \\ C_{M_{b,1}} & C_{M_{b,2}} & \dots & C_{M_{b,N}} & 0 \end{bmatrix} \begin{Bmatrix} \hat{\delta}_{f,1} \\ \hat{\delta}_{f,2} \\ \vdots \\ \hat{\delta}_{f,N} \\ \lambda/2 \end{Bmatrix} = - \begin{Bmatrix} C_{D_{a1}} C_L + C_{D_{01}} \\ C_{D_{a2}} C_L + C_{D_{02}} \\ \vdots \\ C_{D_{aN}} C_L + C_{D_{0N}} \\ 0 \\ -C_{M_{basic}} \end{Bmatrix} \tag{3.4}$$

The above equation solves for minimum induced drag with a constraint on the $C_{M_{basic}}$. This ensures that the pitching moment produced by the variation flaps results in longitudinal

trim. While this will most often not result in elliptical loading, the induced drag value will be as small as possible while allowing for the mean flap to minimize profile drag. The $(N+1)^{th}$ row of Eq. 3.4 displays the weighting function for the multiple flap system. This not only ensures that additional lift added by the variation flaps is zero, but also acts to minimize effects to the $C_{M_{sections}}$ variable. Because the variation flaps do result in airfoil section changes, $C_{M_{sections}}$ could be upset when setting the variation angles. The weighting function acts to negate the affect on lift, and also negates the affect on $C_{M_{sections}}$. However, if trim is not achieved due to small *sections* moments introduced by the variation flap angles, an iteration process is used to adjust the constraint on $C_{M_{basic}}$ and re-solving for the variation angles.

The above steps ensure that, for the desired SM, the wing will operate in the LDR (minimizing profile drag), and set variation flaps which achieve the lowest possible induced drag while trimming the aircraft. Just as *Scheme A* uses the variation flap angles to ensure minimum induced drag and utilized $C_{M_{sections}}$ for trim, *Scheme B* conversely sets the mean angle to ensure minimum profile drag and utilizes $C_{M_{basic}}$ to trim.

3.1.3 $C_{D_{tot}}$ Minimization (Scheme C)

While *Scheme A* and *Scheme B* are successful for reducing their respective components of drag, often times total drag $C_{D_{tot}}$ is not minimized in either case. Total drag is defined as the sum of induced and profile drag, and can suffer in either case because of requirements to trim. For example, if the variation flaps are set to produce elliptical loading and minimum induced drag, the mean flap needs to be set to trim the aircraft. The setting of the mean flap may cause a large increase in profile drag, and thus large total drag.

Minimizing total drag requires the use of an optimizer as discussed in Sec. 2.2.8. The total drag function which outputs total drag based on configuration geometry and flap angles is used by the optimizer as the function to minimize, and the pitching moment about the neutral point is the constraint. The total drag function makes use of the drag polar model for predicting profile drag. Starting values provided to the optimizer are selected to be those flap angles from either *Scheme A* or *B*, whichever produces lower total drag. By choosing starting flap angles in this manner it increases the likelihood of the optimizer finding lowest total drag, guarding against the starting value sensitivity limitation of optimizers discussed in Sec. 2.2.8. For this example, the built-in Matlab optimizer function

fmincon was used which finds minimums of nonlinear multivariable functions with equality constraints. The simplex algorithm was used as the optimization algorithm and the tolerance level of the optimizer was set at $1.0e^{-9}$.

3.2 Configuration Information

In order to demonstrate the drag reduction schemes developed in this chapter, a hypothetical tailless aircraft was used as the example platform with characteristics displayed in Table 3.1.

Table 3.1: Assumed parameter values for the example tailless aircraft.

Static Parameters	Value
Gross weight (W)	14,200 N (3,200 lbf)
Mean aerodynamic chord ($\bar{c}$)	1.01 m (3.31 ft)
Reference area (S)	12.0 m^2 (130 ft^2)
Wing aspect ratio (AR)	12
Static margin (SM)	10 % $\bar{c}$
Number of half-span TE flaps (N)	5
Flap-to-chord ratio (all flaps)	0.2
Variable Parameters	**Value**
$\frac{1}{4}$ *chord* sweep angle (Λ)	20 deg
	35 deg
Airfoil section	A - $C_{m_0} = -0.0802$
	B - $C_{m_0} = 0.055$

As shown, certain parameters were varied, namely quarter-chord sweep angle and airfoil section, in order to provide test cases pertaining to the specific methods used for drag reduction and trim. The aircraft weight (W) along with flight C_L were used to solve for Reynolds number at each flap section location across the span of the tapered wing in order to more accurately predict the effects of the flap deflections. As shown, the aircraft static margin was chosen to be 10% of the mean aerodynamic chord. For each case, the number of TE flaps along the wing half-span was selected to be five, with each flap maintaining a flap-to-chord ratio of 0.2. Figure 3.1 displays the planform of this aircraft when $\Lambda = 20$ deg and shows the equally-spaced TE flaps.

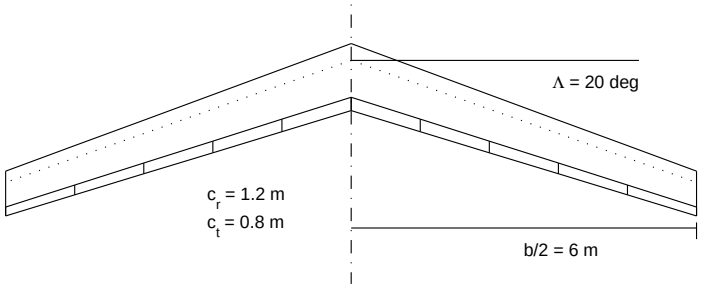

Figure 3.1: Example planform for Λ of 20 degrees and 5 TE flaps per half span.

Indicated by the variable parameter section of Table 3.1 are the two airfoil sections that were tested during this study, which are labeled A and B. Airfoil A is a cambered NLF airfoil which has a zero lift pitching moment coefficient (C_{m_0}) of -0.0802. This airfoil was selected due to its well defined low-drag range, or drag bucket, which surrounds the C_l value of 0.5. Airfoil B is a reflexed NLF airfoil which was designed to have a positive C_{m_0} value of 0.055. It was chosen to study an airfoil of this type because reflexed airfoils are often used on tailless aircraft due to the need for positive lift while also maintaining near-zero or positive pitching moment. Both airfoil A and B were created using the multi-point inverse airfoil design method PROFOIL,[50,51] which allows for the specification of airfoil C_{m_0} as a design parameter.

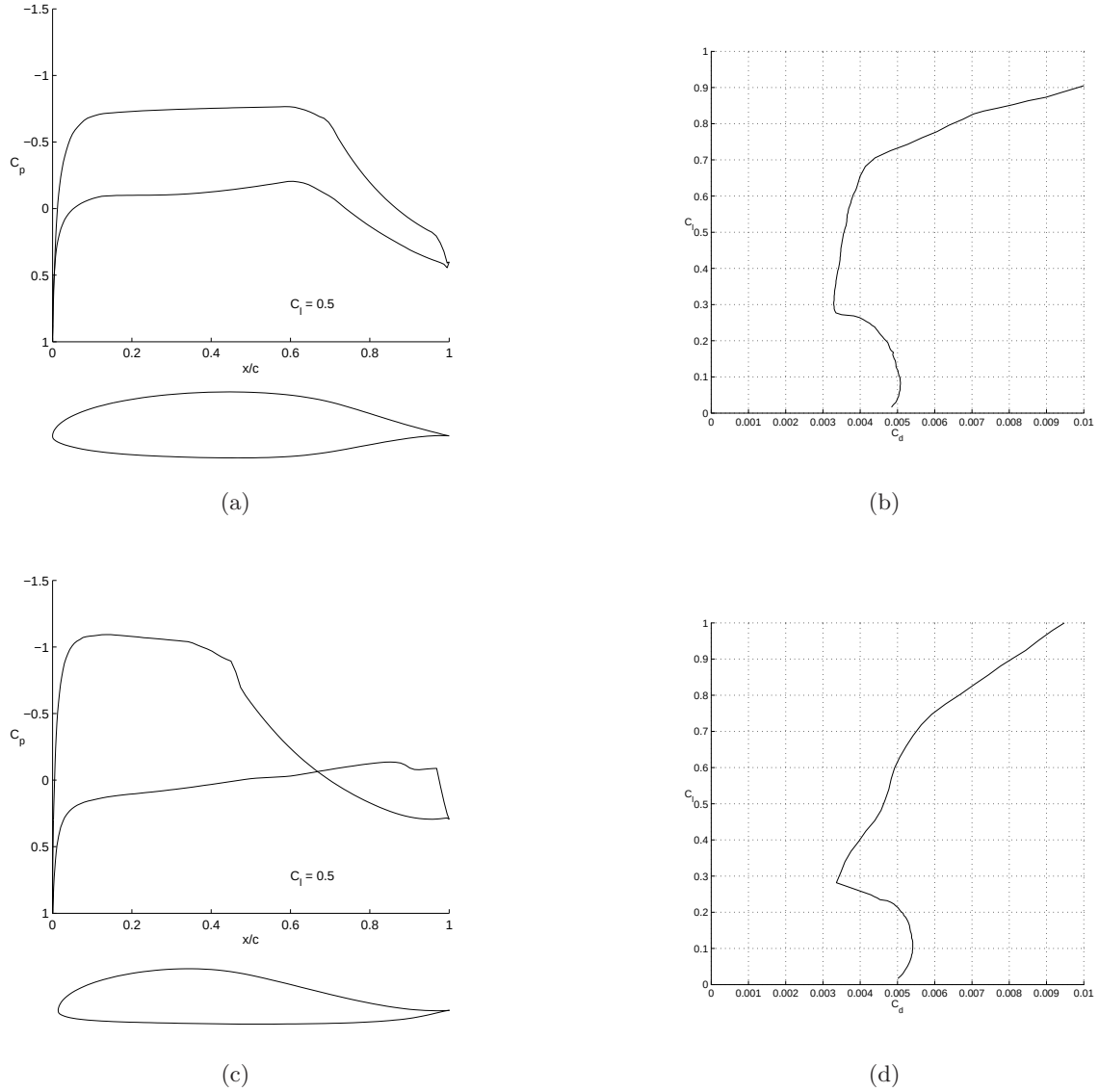

Figure 3.2: (a) Geometry and C_p distribution, airfoil A, (b) drag polar $Re\sqrt{C_l} = 3e6$, airfoil A, (c) Geometry and C_p distribution, airfoil B, and (d) drag polar $Re\sqrt{C_l} = 3e6$, airfoil B.

Figure 3.2 displays the properties of these airfoils as predicted by XFOIL[39] calculated at a $Re\sqrt{C_l}$ of three million, as well as their corresponding geometries. It should be noted that care was taken in the design of airfoil B to place the center of the drag bucket at $C_l = 0.5$ in an attempt to mimic the lift and drag properties of airfoil A. By doing so, it is believed that more accurate comparisons can be made between the airfoils pertaining to drag reduction as well as sweep angle and C_{m_0} influence with respect to trim.

As previously stated, the two airfoils whose aerodynamic properties are displayed in Fig. 3.2 were utilized for the wing planform shown in Fig. 3.1 at sweep angles of 20 deg and 35 deg. This results in four specific configurations, which are presented here as example cases. For each case, spanwise lift plots were produced and validated verses an optimum distribution that was derived from a previous adaptive wing study. In that study, methodology developed by R.T. Jones[52] was followed which solved for optimal loading given a constraint. For the current application, that constraint was modified to be the pitching moment about the neutral point, therefore resulting in the optimal distributions presented here.

3.3 Tailless Results

3.3.1 Cambered airfoil with 20 degree sweep

The first example discusses airfoil A applied to the tapered wing planform with a sweep angle of 20 degrees. Presented in Fig. 3.3 are the total drag numbers for each drag reduction scheme along with their induced and profile components for a range of C_L values. Recall that total drag is the sum of the induced and profile components. Also displayed is the span efficiency for the configuration, which provides a measure of induced drag that is often easier to distinguish. From this figure it is easy to deduce how successful each scheme is for reducing either induced or profile drag, and how that relates to total drag reduction.

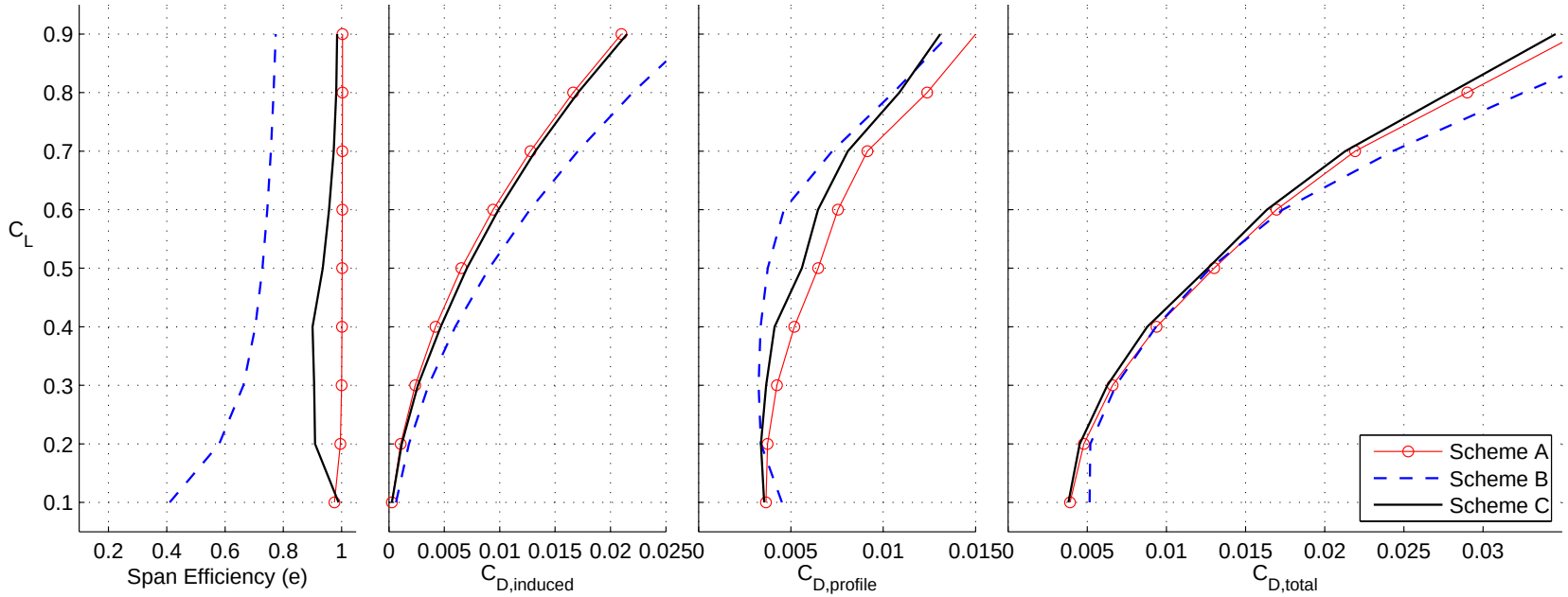

Figure 3.3: Comparison of induced, profile, and total drag for different implementations of the minimization scheme. Results presented for the adaptive tailless configuration with a cambered airfoil and 20 degree wing sweep. Span efficiency results are also shown.

Figure 3.3 shows some important and interesting results regarding the drag reduction schemes. *Scheme A* is focused on reducing induced drag, as is shown to be successful in that objective compared to the other schemes. This is indicated by lower $C_{D_{ind}}$ for the entire C_L range and a span efficiency of 1. For a single wing, a span efficiency value of 1 is achieved through elliptical loading. While *Scheme A* acts well to reduce induced drag, there are penalties in profile drag when compared to *Scheme B*, which is the scheme that reduces profile drag. *Scheme B* is shown to have lower profile drag for the majority of the C_L range, which is expected. At the limits of the C_L range *Scheme B* is shown to produce higher profile drag then the other schemes, which is due to extreme flap angles and separated flow. While *Scheme B* successfully reduced profile drag over the majority of the C_L range, it was shown that induced drag suffers. This is because the mean flap was set to ensure low profile drag, and the lift distribution was set to trim, and is thus off-optimal.

Analyzing the results from *Schemes A* and *B* proves that each is working properly to reduce either induced or profile drag. However, penalties for each scheme in terms of the non-optimized drag component are evident. This leads to higher total drag for both schemes. *Scheme C* optimizes the flap angles such that total drag is reduced, and the result is shown in Fig. 3.3. While total drag is lower for this scheme, it is interesting to note that both the induced- and profile-drag components are not minimized. Rather, the flap angles find a balance between the drag components that leads to total drag reduction.

Further analysis of the drag reduction schemes is obtained from spanwise lift plots, which are displayed for this example in Figs. 3.4 and 3.5. For each scheme the RHS of the wing is plotted with spanwise C_l and overlaid drag polars as predicted by XFOIL. Above each lift plot is a graph of the flap angles as predicted by each scheme. The y-axis is flipped because traditionally trailing-edge down indicates positive flap angles. The lone arrowhead on the right side of each flap angle plot indicates the mean flap deflection angle. Also shown is an optimal C_l distribution for each case, indicated by the spanwise circles. For *Schemes A* and *C* (plots (a) and (c) of the figures), the circles indicate elliptical loading. For *Scheme B* the optimal C_l distribution is produced by following methodology developed by R.T. Jones[52] which solves for optimal loading given a pitching moment constraint.

A low C_L case of 0.3 was chosen as an example for Fig. 3.4. Plot (a) displays *Scheme A*, and shows that elliptical loading is achieved, and thus the high span efficiency for this case. While induced drag is minimized for this case, it comes at the price of profile drag,

shown by the highly negative flaps angles and wing operating outside of the drag buckets. The airfoil used on this configuration is a cambered airfoil with a negative pitching moment (C_{m_0} = -0.0802). To offset this moment the flaps need to be deflected negatively (upwards), and thus the large negative angles. When profile drag is minimized the wing should operate within the drag buckets, which is displayed in *Scheme B*. For this scheme, the flap angles are more reasonable, with the mean flap angle only slightly negative. The shifting of the drag buckets is evident in plot (b), as well as the lift distribution being off-optimal. Recall that for this scheme the lift distribution is used to trim the aircraft, and thus requires more inboard loading. Plot (c) presents a balance between the two previous schemes, as total drag is reduced in *Scheme C*. Shown in the plot is that the C_l distribution is off-optimal, as indicated by the line not matching with the circles. Also, the wing is operating in the upper portion of the drag buckets, indicating some profile drag penalty. However, the penalties for each drag component are balanced such that total drag is minimum.

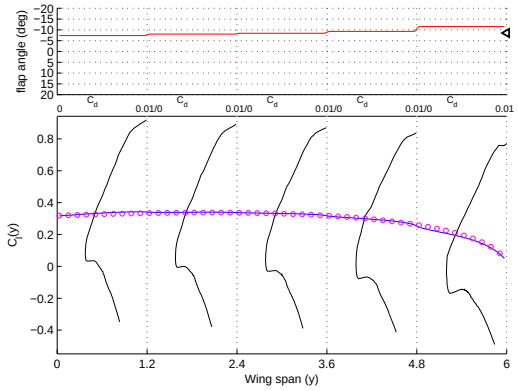

(a) Scheme A

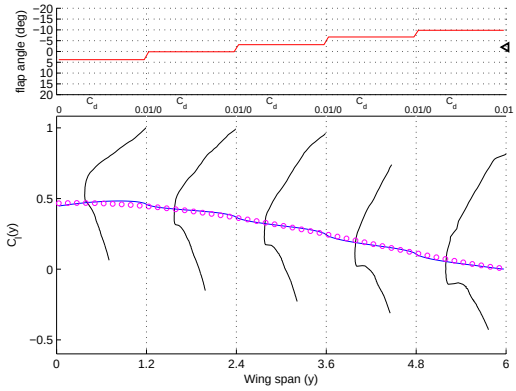

(b) Scheme B

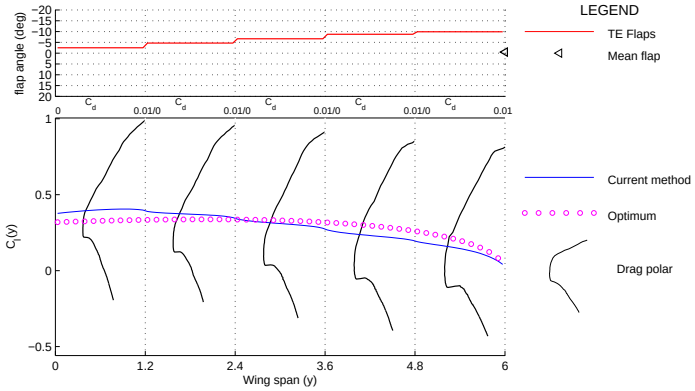

(c) Scheme C

Figure 3.4: Spanwise C_l and drag polar plots to show how drag is reduced at $C_L = 0.3$ for each drag reduction scheme using TE flaps. RHS shown for the adaptive tailless configuration with a cambered airfoil and 20 degree wing sweep.

Figure 3.5 presents spanwise lift plots for the high C_L case of 0.7. Each of the three drag reduction schemes are again represented, and similar arguments can be presented. Plot (a) shows that once again elliptical loading is achieved, and that at higher C_L more negative flap angles are required to trim. This leads to more profile drag for this case. Plot (b) displays the attempt to reduce profile drag. For this scheme, the mean flap is set such that the wing is operating in the low-drag range, and the variation flaps are set to trim the aircraft via the lift distribution. As shown by the most inboard flap, the off-optimal lift distribution requires a large flap deflection and leads to degeneration of the drag polar due

to flow separation. At high C_L values this can often be the case as cruise flaps have limited effectiveness. The spike in profile drag shown by *Scheme B* in Fig. 3.3 indicates the effects of flow separation. The spanwise plot for *Scheme C* highlights the benefits for operating without flow separation, as total drag is minimized for this C_L with lesser flap deflection angles. Again, the C_l distribution is off-optimal and the drag buckets are not perfectly aligned for low profile drag, however a balance is achieved which reduces total drag on the configuration.

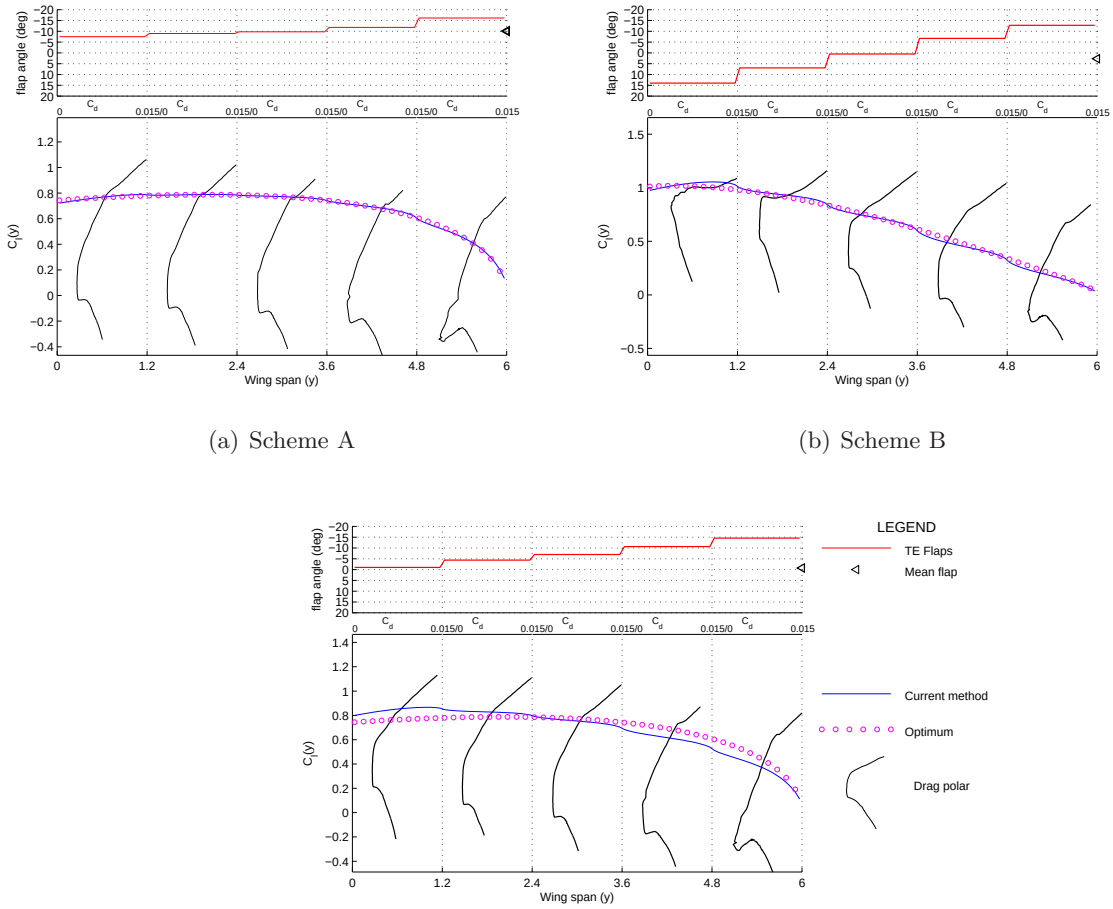

(a) Scheme A

(b) Scheme B

(c) Scheme C

Figure 3.5: Spanwise C_l and drag polar plots to show how drag is reduced at $C_L = 0.7$ for each drag reduction scheme using TE flaps. RHS shown for the adaptive tailless configuration with a cambered airfoil and 20 degree wing sweep.

The analysis provided above presents insight into the drag reduction schemes and their capabilities. It can has been shown that for this particular configuration, trimmed examples reducing both induced and profile drag can be achieved. Aerodynamics is often a science of trade-offs, which was displayed by the total drag results. If total drag is to be lowest, the lift distribution should be designed to consider both induced- and profile-drag components.

3.3.2 Cambered airfoil with 35 degree sweep

The second example case presents a 35 degree sweep configuration again using Airfoil A. Changes in sweep provide interesting results for the drag reduction schemes because the lift distribution is critical for trim on a tailless aircraft. With a larger sweep angle the neutral point location moves further aft, and changes how optimal lift is distributed fore-and-aft. Figure 3.6 displays similar results to the last example, showing the induced- and profile-drag components of the drag reduction schemes over a range of C_L values, and how they combine for total drag.

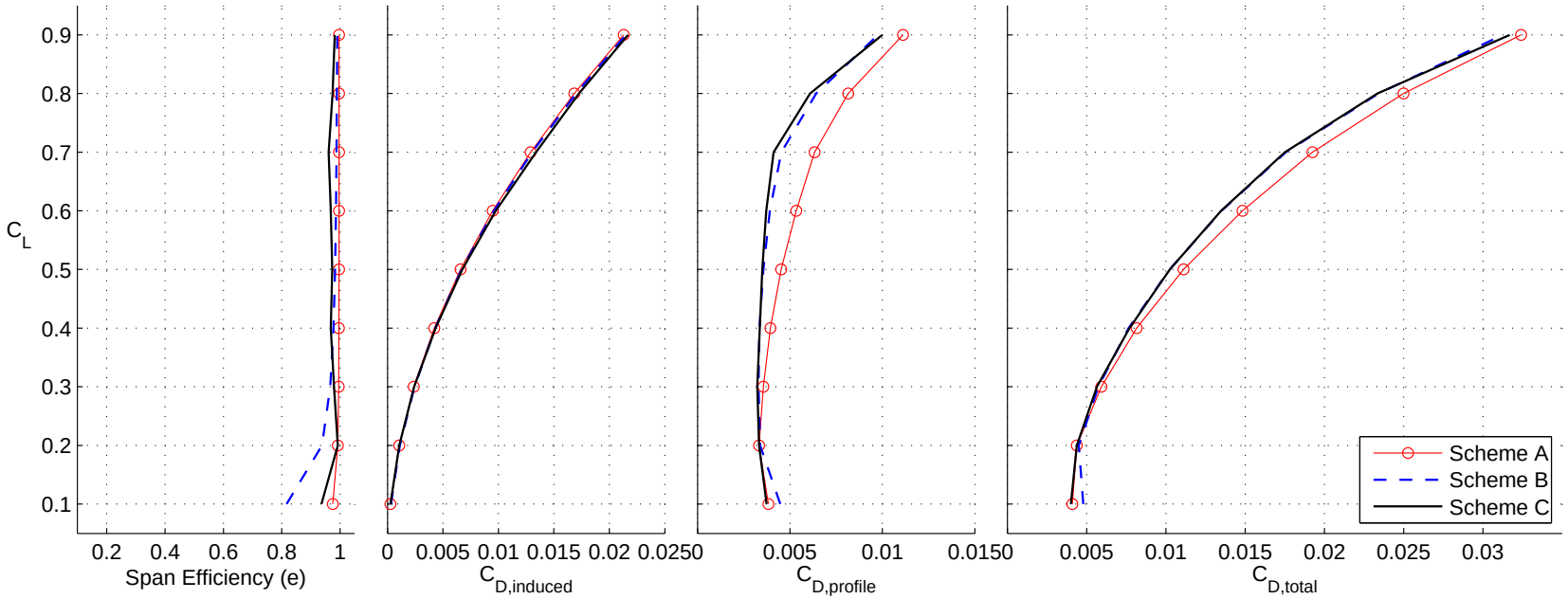

Figure 3.6: Comparison of induced, profile, and total drag for different implementations of the minimization scheme. Results presented for an adaptive tailless configuration with a cambered airfoil and 35 degree wing sweep. Span efficiency results are also shown.

Figure 3.6 once again shows that *Scheme A* effectively minimizes induced drag, and achieves a span efficiency of 1 for the entire C_L range. Profile drag suffers for this scheme, as expected, and leads to higher total drag. *Scheme B* presents interesting results and shows that while profile drag is minimized as expected, the penalties to induced drag is not as severe as in the 20 degree sweep case. This can be explained by considering that, for this sweep angle the NP is shifted aft, and it turns out that a near-elliptical loading ends up trimming the wing in Scheme B. Thus, *Scheme B* results in induced drag values similar to *Scheme A*, and therefore lower total drag. *Scheme C* seeks to balance the induced and profile components of drag to minimize total drag, which is does. However, the amount of drag reduction is vary small, as *Scheme B* already is acting to reduce profile drag and results in good induced drag numbers. Only minimal gains are seen by *Scheme C* for this configuration.

The spanwise lift plots shown below in Fig. 3.7 for a low C_L case of 0.3 provide insight into the ideas presented above. *Scheme A* shows that elliptical loading is achieved, however highly negative flap angles are required for trim and the wing is operating just outside the low-drag-range. This configuration uses the same cambered airfoil as the previous example, and the negative flap angles compensate for the negative C_{m_0}. Plot (b) shows *Scheme B* which acts to position the drag buckets for low profile drag. However, when compared to *Scheme B* for the 20 degree swept wing in Fig. 3.4(b), the loading is spread out more evenly along the span and is closer to elliptical. This shows how induced drag does not suffer much for this configuration. Plot (c) shows that total drag is reduced using flap angles which are very similar to those in plot (b), indicating that reducing profile drag is most important for this particular configuration.

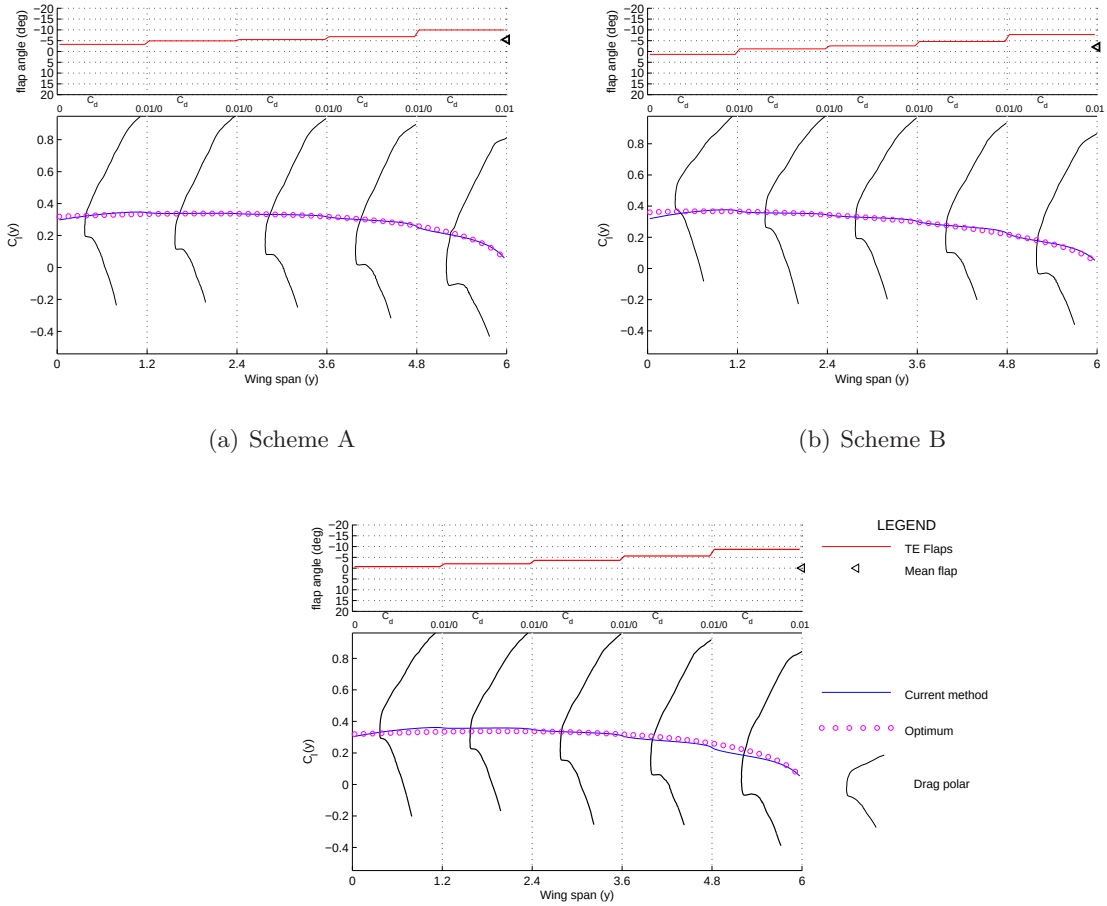

(a) Scheme A

(b) Scheme B

(c) Scheme C

Figure 3.7: Spanwise C_l and drag polar plots to show how drag is reduced at $C_L = 0.3$ for each drag reduction scheme using TE flaps. RHS shown for the adaptive tailless configuration with a cambered airfoil and 35 degree wing sweep.

Figure 3.8 displays spanwise results for the high C_L case of 0.7. Many of the same arguments exist for this example, specifically that profile drag suffers in *Scheme A* and that the loading for *Scheme B* is nearly elliptical, leading to *Scheme B* having lower total drag. Because for each scheme the lift distribution is nearly elliptical, it follows that profile drag reduction will be most important for minimizing total drag. An interesting note is that the total drag reduction scheme, *Scheme C*, found flap angles resulting in lower profile drag then *Scheme B*, as was shown in Fig. 3.6. This is due to approximations being used for the drag polar model and possible unexpected results from flow separation. Considering plots

(b) versus (c), total drag is very slightly lower for plot (c). However the poorly defined drag polar shows that the most inboard flap experiences separated flow. Thus, it is more likely that the flap angles from plot (b) avoid this separation and this result indicates limitations of the approximated drag polar model.

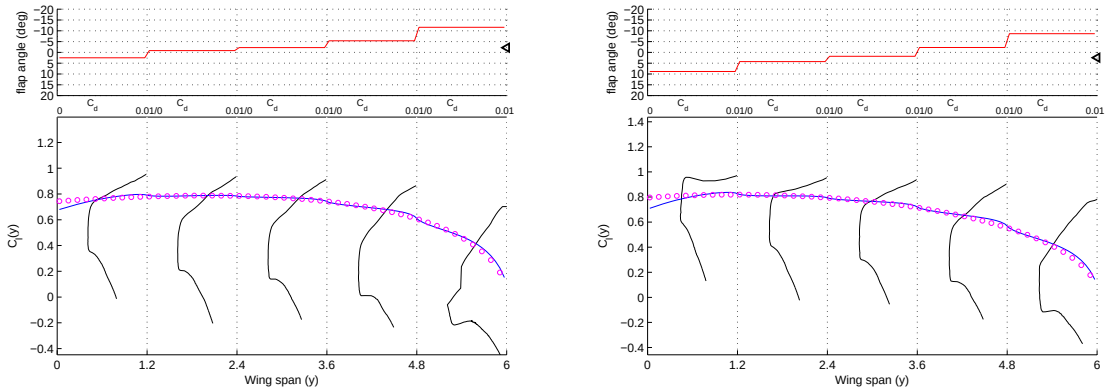

(a) Scheme A

(b) Scheme B

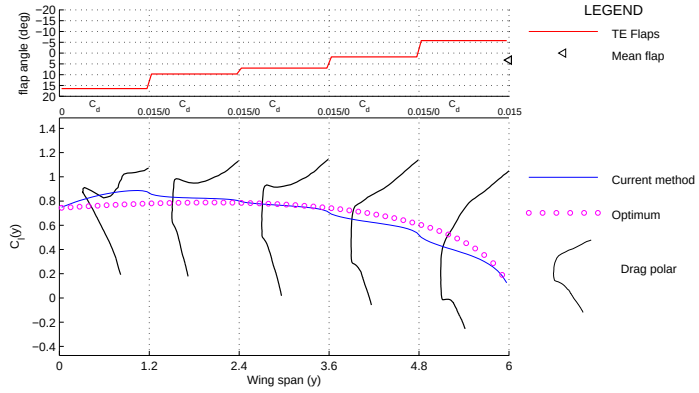

(c) Scheme C

Figure 3.8: Spanwise C_l and drag polar plots to show how drag is reduced at $C_L = 0.7$ for each drag reduction scheme using TE flaps. RHS shown for the adaptive tailless configuration with a cambered airfoil and 35 degree wing sweep.

The results of this section highlight specific attributes of the drag reduction schemes and show the results are affected by changes in wing sweep. There are some clear benefits to the higher sweep angle, specifically the ability to operate with nearly elliptical lift for each

case. These ideas give general insight into design trends for tailless aircraft with cambered airfoils.

3.3.3 Reflexed airfoil with 20 degree sweep

This section presents results produced by a tailless configuration with 20 degrees of sweep, shown in Fig. 3.1, and with a reflexed airfoil section, Airfoil B. Information regarding the airfoil section is presented in Fig. 3.2(c) and (d). It is interesting to study a reflexed airfoil section for this problem because they are often used on tailless configurations which require a nearly zero C_{m_0} due to the lack of secondary lifting surface. As shown, this reflexed airfoil maintains some laminar flow along its upper and lower surfaces, and has a defined drag bucket similar to the cambered airfoil. The C_{m_0} for this airfoil is 0.055.

Displayed in Fig. 3.9 are total drag results for this configuration over a range of C_L values. As expected, *Scheme A* results in lower induced drag and a span efficiency of 1 for the C_L range due to elliptical loading. Profile drag suffers for this scheme at high and low C_L values, however at mid-range C_L values, the profile drag is as low as that from *Scheme B*. This result is coincidental, as the positive C_{m_0} of this airfoil will require a slightly positive mean flap deflection for trim, and thus places the wing inside the drag buckets of the airfoil section. *Scheme B* shows that when profile drag is minimized, induced drag suffers particularly at low C_L values. However, the lower profile drag of *Scheme B* leads to lower total drag for the low and high C_L cases when compared to *Scheme A*. The most curious results are those of *Scheme C*, which minimizes total drag. While total drag is primarily lower for the C_L range, the drag results tend to jump around at low C_L values. This can be explained by the sensitivity that the optimizer used by this work has on input flap angles. For example, at $C_L = 0.1$ the starting flap angles provided to the optimizer were those resulting in minimum induced drag (from *Scheme A*). The solution is optimized and finds lower drag in the vicinity of the starting values, giving high span efficiency. At $C_L = 0.3$, flap angles from *Scheme B* are used as starting values, and the solution is optimized with lower span efficiency. This particular example highlights the limitations of the optimizer for finding minimum total drag, as it is very dependent on starting values. Section 3.3.5 focuses on the starting value dependency of the optimizer and shows results produced from different starting values to illustrate this limitation of the optimizer for the example configuration.

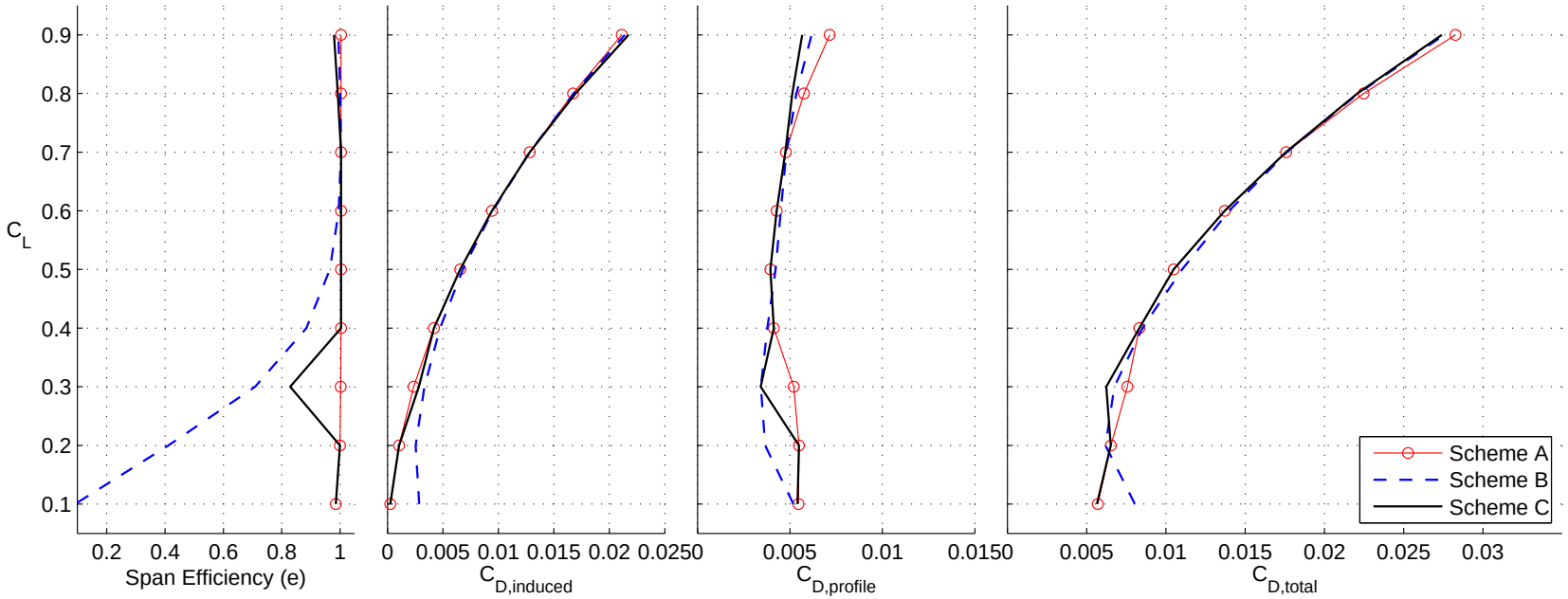

Figure 3.9: Comparison of induced, profile, and total drag for different implementations of the minimization scheme. Results presented for an adaptive tailless configuration with a reflexed airfoil and 20 degree wing sweep. Span efficiency results are also shown.

Figures 3.10 and 3.11 show spanwise lift results for the example case and allows further analysis of the drag reduction schemes. Figure 3.10 presents the results for the low C_L case of 0.3 for each scheme. Plot (a) shows that *Scheme A* does indeed result in elliptical loading, however the wing is operating well outside the drag buckets, leading to increased profile drag. Plot (b) shows the opposite, as the wing is operating in the low drag ranges of the airfoil sections, but is very far from optimal, leading to increased induced drag. Plot (c) shows results from *Scheme C*, and looks similar to plot (b). The flap angles for this case are optimized starting with the flap angles from *Scheme B*, and minimal gains are shown from there.

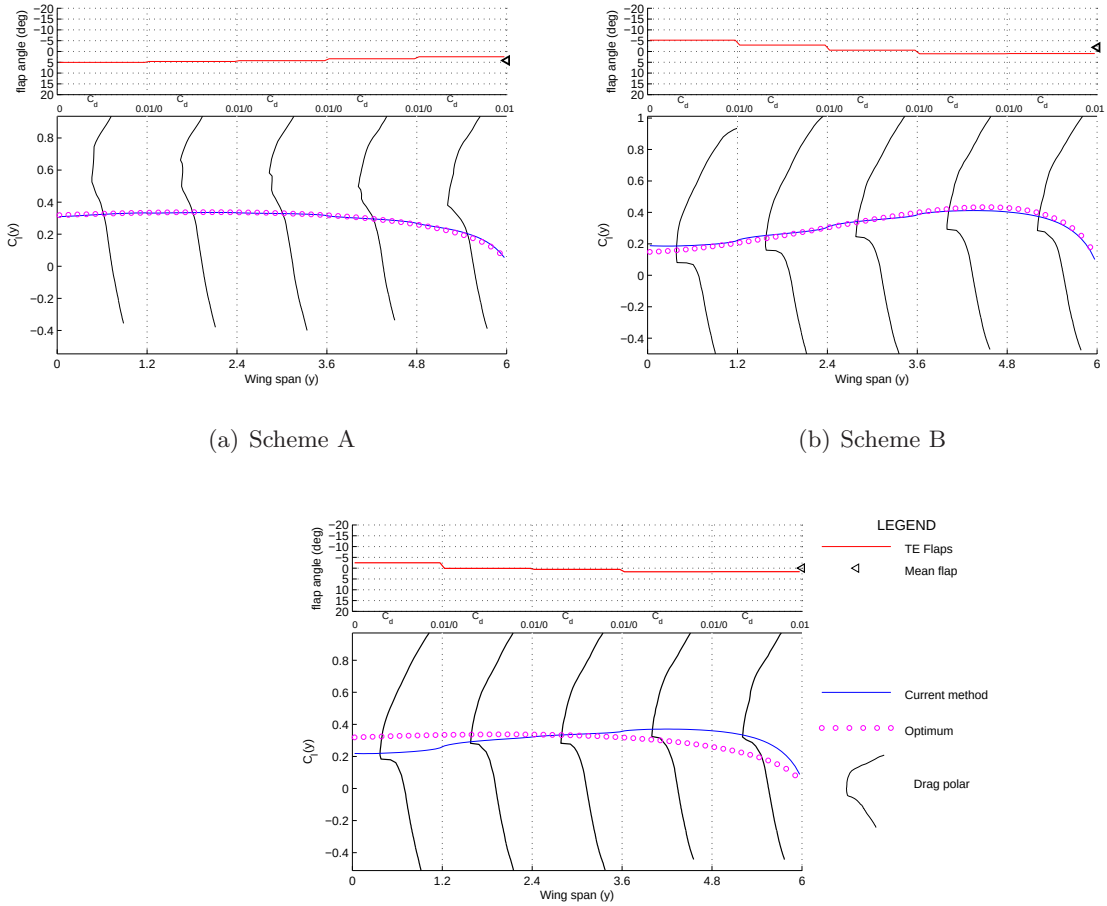

(a) Scheme A

(b) Scheme B

(c) Scheme C

Figure 3.10: Spanwise C_l and drag polar plots to show how drag is reduced at $C_L = 0.3$ for each drag reduction scheme using TE flaps. RHS shown for the adaptive tailless configuration with a reflexed airfoil and 20 degree wing sweep.

The high C_L case of 0.7 is displayed in Fig. 3.11 for each drag reduction scheme. For this C_L each of the drag reduction schemes predict very similar solutions, as shown by the shape of the lift distribution and the flap angles. An explanation for this result is that both *Scheme A* and *B* coincidentally lead to similar flap deflections, which also happen to be optimal for low total drag. The positive C_{m_0} produced by the reflexed airfoil used on this configuration leads to similar mean flap angles required for trimming the aircraft when elliptical loading is achieved and when the wing is operating within the low-drag range. As a consequence of similar flap angles, the drag results are also similar.

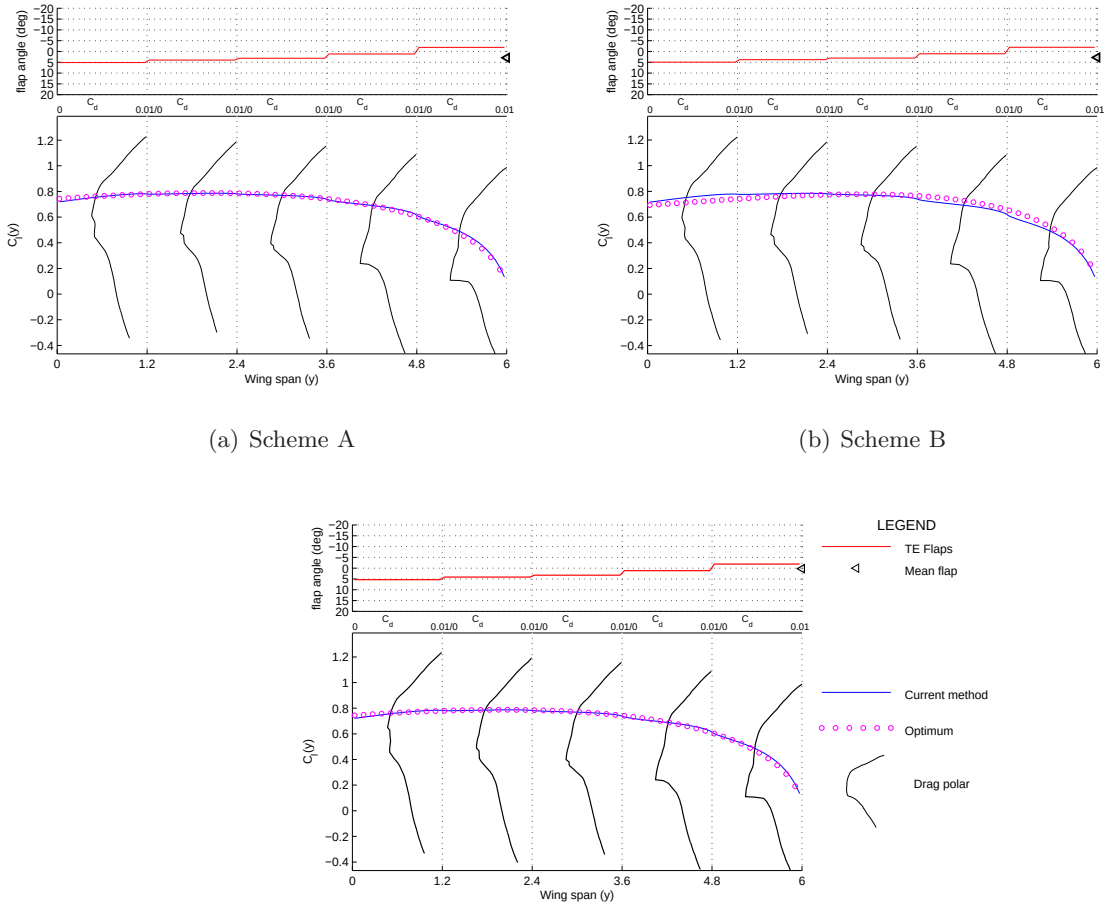

(a) Scheme A

(b) Scheme B

(c) Scheme C

Figure 3.11: Spanwise C_l and drag polar plots to show how drag is reduced at $C_L = 0.7$ for each drag reduction scheme using TE flaps. RHS shown for the adaptive tailless configuration with a reflexed airfoil and 20 degree wing sweep.

This example provides interesting insight into the benefits of using an airfoil with a positive pitching moment. It was shown that by using such an airfoil, flap angles predicted by each drag reduction schemes will be similar, and lead to low total drag for each scheme. Also shown by this example were limitations for using an optimizer for solving total drag. Specifically, the optimizer is shown to be very sensitive to input flap angles and leads to results that can be non-intuitive.

3.3.4 Reflexed airfoil with 35 degree sweep

The final example presented for the tailless configuration is a sweep angle of 35 degrees utilizing the reflexed airfoil, Airfoil B. Previous wing sweep analysis for the configuration using the cambered airfoil concluded that increasing sweep allowed for load distributions close to elliptical due to the shift in the fore-and-aft distribution of lift relative to the NP. When using the reflexed airfoil, however, the positive C_{m_0} of the airfoil requires that the lift distribution produce a nose-down moment for trim. This will lead to off-elliptical loading, and thus induced drag penalties are shown by *Scheme B* in Fig. 3.12. The induced drag penalties of *Scheme B* are not significant, however, and low total drag is achieved by the profile drag scheme for the majority of the C_L range. *Scheme C* shows results that produce low total drag, while again displaying sensitivity at low C_L values. The results from *Scheme C* provides little insight, which is another limitation of using an optimizer for minimizing drag.

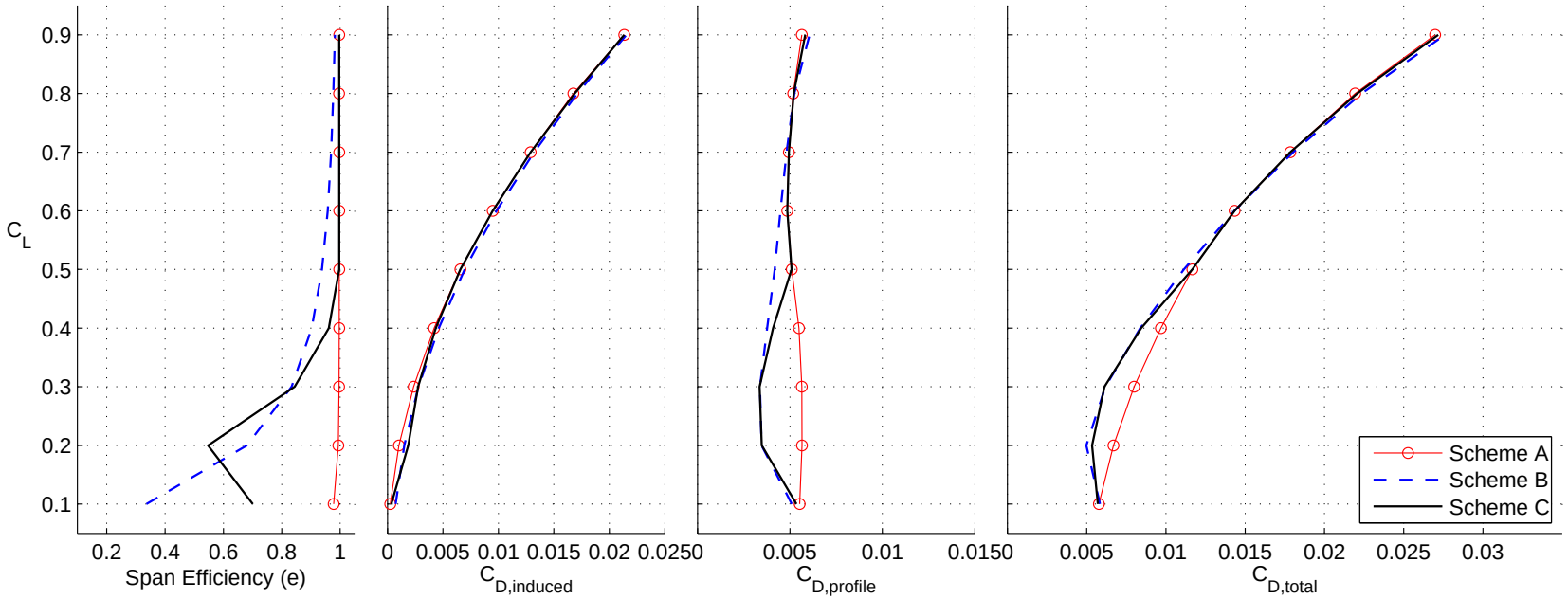

Figure 3.12: Comparison of induced, profile, and total drag for different implementations of the minimization scheme. Results presented for an adaptive tailless configuration with a reflexed airfoil and 35 degree wing sweep. Span efficiency results are also shown.

The spanwise plots in Fig. 3.13 again show how the induced and profile drag reduction schemes act to minimize drag at a low C_L value of 0.3. As mentioned above, when using a cambered airfoil the loading shown by plot (b) was nearly elliptical due to the fore-and-aft distribution of lift relative to the neutral point. For the configuration of this example, which uses the reflexed airfoil, plot (b) shows that the loading is far from elliptical, and results in induced drag penalties. Plot (c) once again shows a solution similar to plot (b), and indicates the influence that the starting values derived from *Scheme B* have on the optimizer.

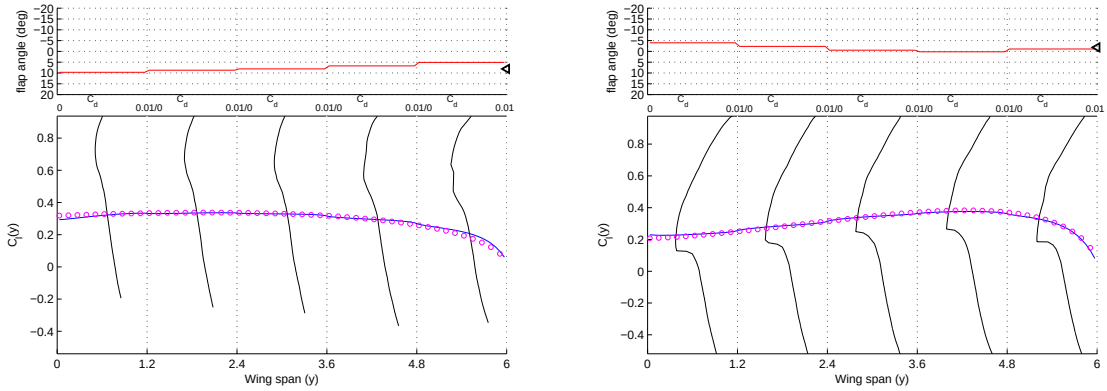

(a) Scheme A

(b) Scheme B

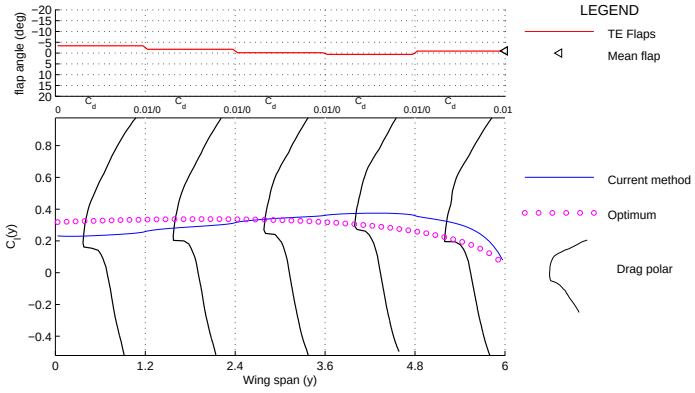

(c) Scheme C

Figure 3.13: Spanwise C_l and drag polar plots to show how drag is reduced at $C_L = 0.3$ for each drag reduction scheme using TE flaps. RHS shown for the adaptive tailless configuration with a reflexed airfoil and 35 degree wing sweep.

For the high C_L case of 0.7 displayed in Fig. 3.14, each of the spanwise lift plots look similar. This indicates that each of the drag reduction schemes are acting similar to reduce drag, and is a coincidental result for this configuration. The total drag plots shown in Fig. 3.12 support this result, as for each drag reduction scheme at high C_L the total drag values are nearly the same.

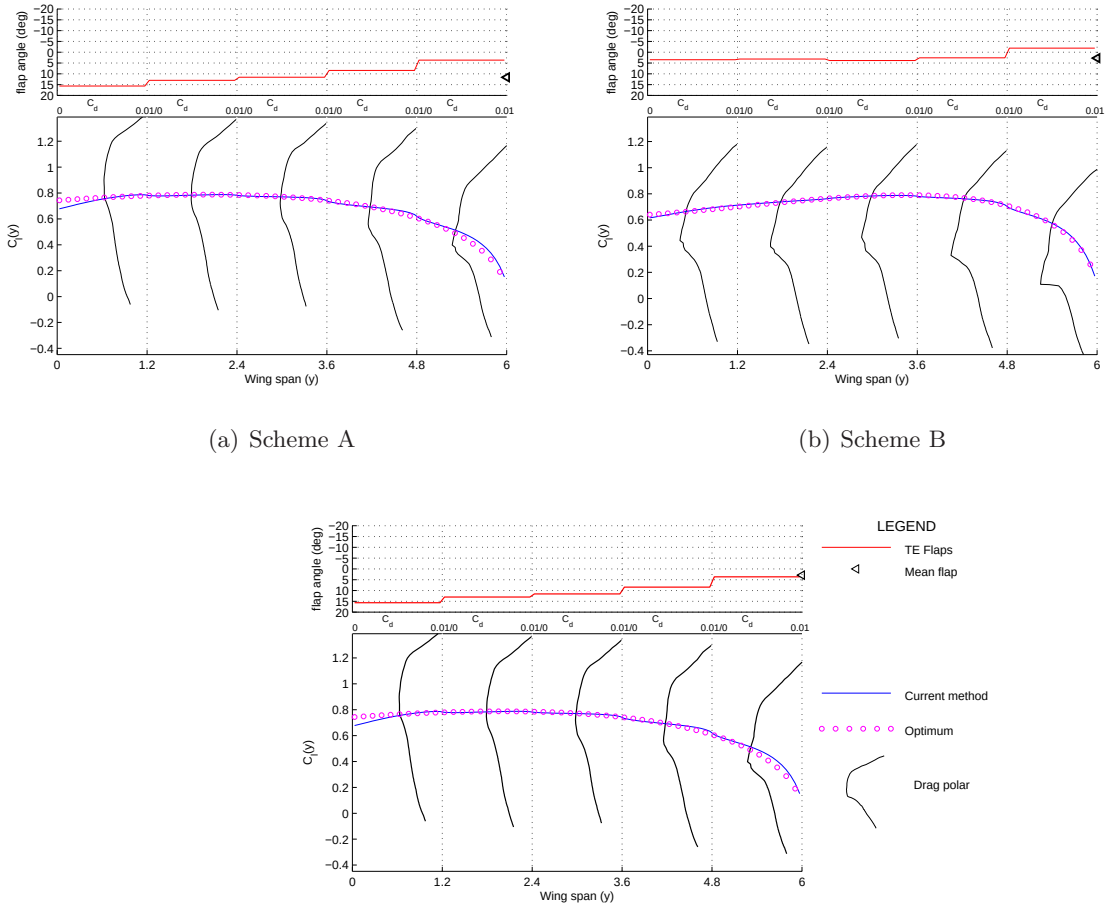

(a) Scheme A

(b) Scheme B

(c) Scheme C

Figure 3.14: Spanwise C_l and drag polar plots to show how drag is reduced at $C_L = 0.7$ for each drag reduction scheme using TE flaps. RHS shown for the adaptive tailless configuration with a reflexed airfoil and 35 degree wing sweep.

The configuration discussed here displays similar results to those of the 20 degree sweep case using the same airfoil. For the particular drag reduction schemes it seems that there is little benefit increasing wing sweep.

3.3.5 Optimizer Starting Value Sensitivity Study

Discussed in Sec. 2.2.8 was the sensitivity to starting values that the optimizer has when determining optimal flap angles. Further, results presented in this chapter have highlighted this sensitivity, and showed how input flap angles influence total drag solutions. This section focuses on the optimizer sensitivity, and presents results from the total drag optimizer over a range of C_L values when provided different starting values. The configuration used in this study is identical to that of section 3.3.4, which is the tailless aircraft with 35 degree wing sweep and the reflexed airfoil section. Figure 3.15 shows drag values in a manner similar to previous results. Total drag is displayed along with the induced- and profile-drag components. For each case, the total drag reduction scheme ($Scheme\,C$) was used with the specified starting flap values provided to the optimizer.

The obvious result shown by Fig. 3.15 is that, despite the fact that each case is attempting to minimize total drag, different drag values are produced by each case. Clearly, the optimizer converges on different minimums and produces very different solutions based on starting values. As shown, the results from the case which uses starting values from the induced drag reduction scheme maintain low induced drag. This is evident from the high span efficiency over the entire range of C_L values. On the other hand, the results shown from the case using starting values from the profile drag reduction scheme show more induced drag and less profile drag for the C_L range. The last set of results shown is from the optimizer with starting values of zero degrees for each flap. These results show values that differ from the other two cases, and have neither low induced nor low profile drag for the entire C_L range. The case with zero flap angles as starting values is shown to produce total drag results that are sometimes less than the other cases, and sometimes greater than the other cases depending on the C_L value. These results cannot be anticipated, further reinforcing the sensitivity of this scheme to starting flap values.

These results clearly show the limitation of using an optimizer for the current problem, highlighting the sensitivity that the solution has on starting flap values. While the flap angle solutions provided by the optimizer have been shown to be valuable for producing low total drag results in some cases, caution must be taken to ensure that the flap angles are truly indicative of the lowest total drag solution. These flap angle solutions provide good opportunity for comparison versus other drag reduction schemes, however their ability to provide insight into aerodynamic design is limited.

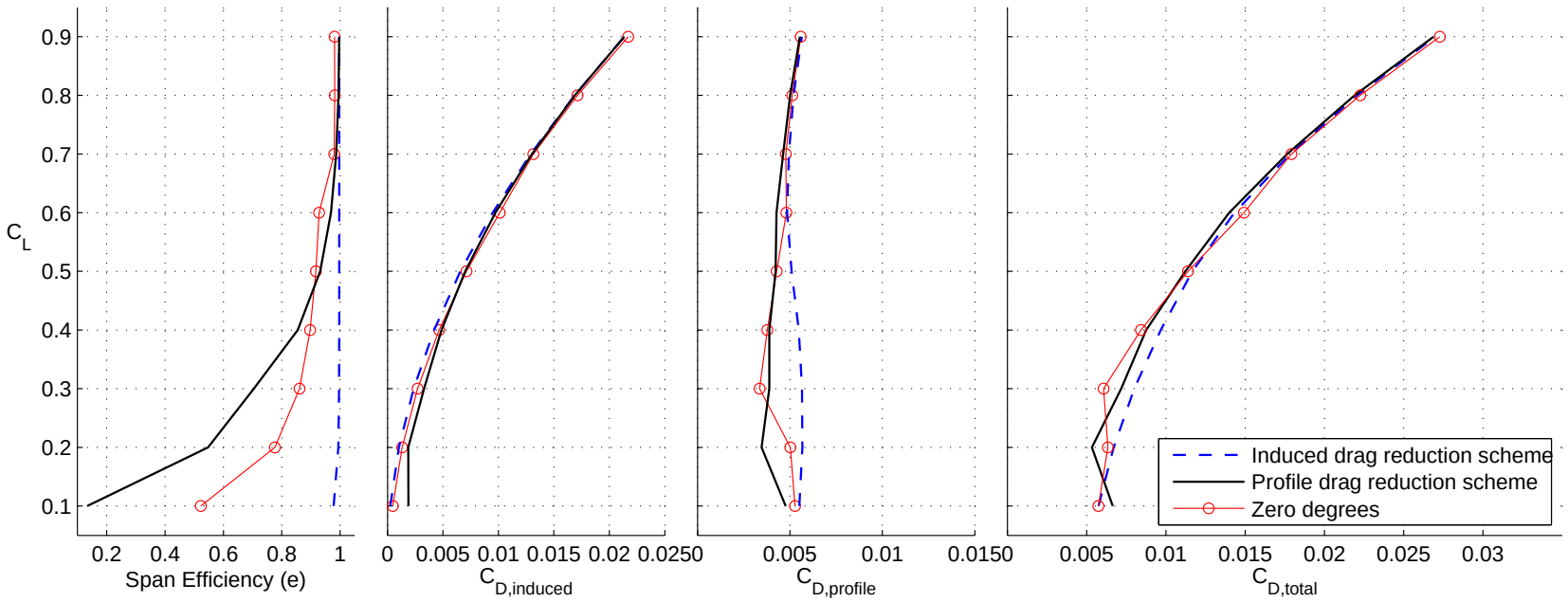

Figure 3.15: Comparison of drag produced by the total drag reduction scheme (*Scheme C*) when provided different starting flap-angle values to the optimizer. Starting flap-angle values are: zero degrees for all flaps, flaps produced by the induced drag reduction scheme, and flaps produced by the profile drag reduction scheme. The results show the starting flap-angle sensitivity of the optimizer.

3.4 Tailless Aircraft Summary and Conclusions

This chapter has presented specific methodology for determining optimal flap angles for an adaptive tailless aircraft. Tailless configurations are of interest due to their design simplicity and theoretical gains in efficiency. Building on the background and methodology presented in Chapter 2, specific drag reduction schemes were introduced for minimizing induced, profile, or total drag. Example cases were presented which studied how changes in wing sweep and airfoil section affect the drag reduction schemes. These examples utilized a cambered NLF airfoil, as well as a reflexed NLF airfoil which is more typical of tailless configurations.

The example cases highlighted the success that each drag reduction scheme has for minimizing their respective components of drag. For each configuration example, the drag reduction scheme which intends to minimize induced drag led to spanwise elliptical loading of the wing. While the scheme which reduces profile drag led to the wing operating within the low-drag ranges of the airfoil sections. Each drag reduction scheme presented trade-offs in terms of their non-optimized component of drag. For example, when induced drag was minimized, profile drag increased, and vice-versa. The total drag scheme acted to balance this trade-off and solved for flap angles resulting lower total drag.

When using a cambered airfoil with a negative C_{m_0}, minimizing induced drag led to high total drag because large, negative mean flap deflections were necessary to trim. This led to higher profile drag. When more sweep was introduced into the configuration, low induced drag was achieved for each drag reduction scheme due to the shifting of the distribution of lift relative to the neutral point. This allowed for the spanwise load to take on a more elliptical shape, and thus low induced drag. For the reflexed airfoil, sweep was not as beneficial, as the positive C_{m_0} required the spanwise loading outboard to produce a nose-down pitching moment and trim. The reflexed airfoil examples showed benefits in that the mean flap angles to trim and to achieve low profile drag are similar. In particular at higher C_L values, the examples using the reflexed airfoil showed that flap angle settings predicted by the drag reduction schemes can be similar, thus resulting in similarly optimal total drag results.

The example cases also brought out some limitations of using an optimizer for determining flap angles. While the optimizer successfully reduced total drag in most cases, the results were very sensitive to input flap angles. Further, the solutions predicted by the

optimizer provides little insight into successful design, and merely produce flap angles to be plugged into an analysis routine.

This chapter has introduced the usefulness of the adaptive methodology and has applied it successfully to example configurations. The methodology provides useful aerodynamic insight for tailless configurations, and shows the trade-offs that are involved in aerodynamic design. For each example case, the schemes act differently indicating that no one scheme is universal for reducing total drag. However, the methodology can be considered a powerful design tool for analyzing tailless configurations with constraints.

Chapter 4

Optimal Lift Distributions for a Three-Surface Aircraft

This chapter explores drag reduction using multiple TE flaps on an example adaptive three-surface aircraft configuration. The three-surface example is a planar configuration consisting of a wing, aft-tail, and canard. The configuration was chosen due to the increased design opportunities provided by the additional surfaces. Section 4.1 introduces specific drag reduction schemes in five subsections. The first two subsections discuss the minimization of induced and profile drag. The third subsection provides a two-step optimization approach for drag reduction and aerodynamic analysis. The fourth subsection discusses total drag reduction. The fifth and final subsection displays a surface lift study which validates the methods. Section 4.2 details the configuration information for the three-surface adaptive aircraft used as an example in this study. Section 4.3 presents induced, profile, and total drag results for a range of C_L values for the three-surface aircraft configuration. Also displayed are flap-angle solutions and spanwise lift distribution examples for the configuration and discussion pertaining to the flap angles is provided. Section 4.4 presents conclusions pertaining to the drag reduction schemes applied to a three-surface configuration.

4.1 Drag Reduction Schemes for a Three-Surface Aircraft

4.1.1 $C_{D_{ind}}$ Minimization

The first drag reduction scheme presented focuses on minimizing $C_{D_{ind}}$. It was stated that for a wing, minimum induced drag results from elliptical loading. For the tailless aircraft example presented in Chapter 3, flap angles were determined such that induced drag was minimized and elliptical load was achieved. Multiple surface configurations provide different results, as often surfaces operate in wake regions of other surfaces, affecting the flow over the surface and its lift and drag properties. Thus, for a multiple surface example, the shape of the loading on the wing for minimum induced drag is not unique and is dependent on vertical separation between the lifting surfaces. To validate if minimum induced drag is achieved, the span efficiency of the configuration can be compared to a single wing, and should equal or exceed unity.

Section 2.2.5 introduced a system of equations which solve for minimum induced drag with a constraint on the pitching moment. This method is closely followed for the multiple-surface example as it is the simplest method optimizing a configuration for induced drag. Given a configuration with N flaps, the flap angles resulting in minimum trimmed induced drag can be obtained by solving the system of linear equations expressed in matrix form as:

$$\begin{bmatrix} C_{D_{11}} & C_{D_{12}} & \dots & C_{D_{1N}} & C_{M_1} \\ C_{D_{21}} & C_{D_{22}} & \dots & C_{D_{2N}} & C_{M_2} \\ \vdots & \vdots & & \vdots & \vdots \\ C_{D_{N1}} & C_{D_{N2}} & \dots & C_{D_{NN}} & C_{M_N} \\ C_{M_1} & C_{M_2} & \dots & C_{M_N} & 0 \end{bmatrix} \begin{Bmatrix} \delta_{f,1} \\ \delta_{f,2} \\ \vdots \\ \delta_{f,N} \\ \lambda/2 \end{Bmatrix} = - \begin{Bmatrix} C_{D_{a1}} C_L + C_{D_{01}} \\ C_{D_{a2}} C_L + C_{D_{02}} \\ \vdots \\ C_{D_{aN}} C_L + C_{D_{0N}} \\ -(SM \times C_L) + C_{M_0} \end{Bmatrix} \tag{4.1}$$

It is important to note that in the above equation the flap angles to be optimized can be variation flaps, mean flaps, or a combination of the two. It is only necessary that the terms of the drag interdependency matrix and constraint equation be calculated and stored appropriately. Because the flaps exist on multiple surfaces, ensuring linear independence of the matrix equations is not an issue for a multiple configuration. Thus, the weighting factor equation is not present in Eq. 4.1.

4.1.2 $C_{D_{pro}}$ Minimization

Decomposing the TE flap angles into mean and variation angles allows for the use of drag reduction techniques similar to those presented for the tailless configuration. Recall that for a single surface, a deflection of the mean flap is similar to deflecting the flap of an airfoil, and acts as a cruise flap for reducing profile drag $C_{D_{pro}}$. For a multiple surface configuration utilizing a primary lifting surface that is much larger then the secondary surfaces, profile drag caused by the primary surface will dominate the total profile drag of the aircraft due to its much larger surface area. Profile drag can be sufficiently reduced by setting the mean flap of this primary surface to ensure the surface is operating in the low-drag range. The method for determining the mean-flap setting resulting in low total drag was shown in Sec. 2.2.6, and Eq. 2.36 is specifically used to interpolate the optimal value.

Considering the system of multiple flap variables presented earlier, if one of the flap angles is fixed at a value for drag-bucket control (profile drag optimization), the dimension of the system reduces by one and the remaining flaps can still be optimized for minimum $C_{D_{ind}}$. Displayed in Eq. 4.2 is the example where flap j has been fixed at a value of $X_{f,j}$.

$$\begin{bmatrix} C_{D_{11}} & \cdots & C_{D_{1j-1}} & C_{D_{1j+1}} & \cdots & C_{D_{1N}} & C_{M_1} \\ \vdots & & \vdots & \vdots & & \vdots & \vdots \\ C_{D_{j-11}} & \cdots & C_{D_{j-1j-1}} & C_{D_{j-1j+1}} & \cdots & C_{D_{j-1N}} & C_{M_{j-1}} \\ C_{D_{j+11}} & \cdots & C_{D_{j+1j-1}} & C_{D_{j+1j+1}} & \cdots & C_{D_{j+1N}} & C_{M_{j+1}} \\ \vdots & & \vdots & \vdots & & \vdots & \vdots \\ C_{D_{N1}} & \cdots & C_{D_{Nj-1}} & C_{D_{Nj+1}} & \cdots & C_{D_{NN}} & C_{M_N} \\ C_{M_1} & \cdots & C_{M_{j-1}} & C_{M_{j+1}} & \cdots & C_{M_N} & 0 \end{bmatrix} \begin{Bmatrix} \delta_{f,1} \\ \vdots \\ \delta_{f,j-1} \\ \delta_{f,j+1} \\ \vdots \\ \delta_{f,N} \\ \lambda/2 \end{Bmatrix} = \tag{4.2}$$

$$- \begin{Bmatrix} C_{D_{a1}} C_L + C_{D_{01}} \\ \vdots \\ C_{D_{aj-1}} C_L + C_{D_{0j-1}} \\ C_{D_{aj+1}} C_L + C_{D_{0j+1}} \\ \vdots \\ C_{D_{aN}} C_L + C_{D_{0N}} \\ -SM \times C_L + C_{M_0} \end{Bmatrix} - \begin{Bmatrix} C_{D_{1j}} \\ \vdots \\ C_{D_{j-1j}} \\ C_{D_{j+1j}} \\ \vdots \\ C_{D_{Nj}} \\ C_{M_j} \end{Bmatrix} [\, X_{f,j} \,]$$

Thus, it is possible to fix the value of flap j to some value which ensures minimum profile drag for that surface, and still achieve the minimum $C_{D_{ind}}$ value by optimum selection of the remaining flap angles. For a multiple surface example, flap j would represent the mean-flap on the primary surface. The remaining $N-1$ flap variables represent the variation flaps of the configuration as well as the mean flaps of the secondary surfaces. The $(N+1)^{th}$ row is the pitching moment constraint which ensures trim.

4.1.3 Two-Step Optimization Approach

While the above methods provide powerful and elegant approaches for minimizing drag, it may be desirable to formulate the problem in other ways in order to gain additional insight into the aerodynamic principles at work in such a complex system. For instance, the Results section of this chapter explores a three-surface aircraft which has eight flaps distributed on three surfaces. And while all eight flaps could be inserted into Eq. 4.1, producing a valid solution, it would be very difficult to speak intelligently about the solution angles, except to say that $C_{D_{ind}}$ is minimized. The two-step optimization approach presented in this section is intended to not only provide the solution, but also provide valuable insight and control over some flap angles for profile drag minimization. For this approach, the eight flaps are decomposed into three mean flaps (one for each surface) and eight variation flaps, resulting in 11 flap variables.

The two-step approach is as follows. First, only the three mean flaps are optimized for trimmed $C_{D_{ind}}$ as displayed in Eq. 4.3, providing specific insight into optimal trimmed lift ratios for the three surface aircraft.

$$\begin{bmatrix} C_{D_{ww}} & C_{D_{wt}} & C_{D_{wc}} & C_{M_w} \\ C_{D_{tw}} & C_{D_{tt}} & C_{D_{tc}} & C_{M_t} \\ C_{D_{cw}} & C_{D_{ct}} & C_{D_{cc}} & C_{M_c} \\ C_{M_w} & C_{M_t} & C_{M_c} & 0 \end{bmatrix} \begin{Bmatrix} \bar{\delta}_{f,w} \\ \bar{\delta}_{f,t} \\ \bar{\delta}_{f,c} \\ \lambda/2 \end{Bmatrix} = - \begin{Bmatrix} C_{D_{aw}} C_L + C_{D_{0w}} \\ C_{D_{at}} C_L + C_{D_{0t}} \\ C_{D_{ac}} C_L + C_{D_{0c}} \\ -SM \times C_L + C_{M_0} \end{Bmatrix} \tag{4.3}$$

In Eq. 4.3, the bars designate mean flaps and the subscripts indicate the surface (wing, tail, or canard) being considered. Second, the eight variation flap angles are solved such that each individual surface C_L is unchanged, and the added section pitching moment due to variation flap deflection is forced to zero.

$$\begin{bmatrix} C_{D_{11}} & C_{D_{12}} & \cdots & C_{D_{18}} \\ C_{D_{21}} & C_{D_{22}} & \cdots & C_{D_{28}} \\ \vdots & \vdots & & \vdots \\ C_{D_{81}} & C_{D_{82}} & \cdots & C_{D_{88}} \\ C_{L_{w,1}} & C_{L_{w,2}} & \cdots & C_{L_{w,8}} \\ C_{L_{t,1}} & C_{L_{t,2}} & \cdots & C_{L_{t,8}} \\ C_{L_{c,1}} & C_{L_{c,2}} & \cdots & C_{L_{c,8}} \\ C_{M_{sections,1}} & C_{M_{sections,2}} & \cdots & C_{M_{sections,8}} \end{bmatrix} \begin{Bmatrix} \hat{\delta}_{f,1} \\ \hat{\delta}_{f,2} \\ \vdots \\ \hat{\delta}_{f,8} \end{Bmatrix} =$$

$$-\begin{Bmatrix} C_{D_{a1}}C_L + C_{D_{01}} \\ C_{D_{a2}}C_L + C_{D_{02}} \\ \vdots \\ C_{D_{a8}}C_L + C_{D_{08}} \\ 0 \\ 0 \\ 0 \\ 0 \end{Bmatrix} - \begin{Bmatrix} C_{D_{1w}} & C_{D_{1t}} & C_{D_{1c}} \\ C_{D_{2w}} & C_{D_{2t}} & C_{D_{2c}} \\ \vdots & \vdots & \vdots \\ C_{D_{8w}} & C_{D_{8t}} & C_{D_{8c}} \\ 0 & 0 & 0 \\ 0 & 0 & 0 \\ 0 & 0 & 0 \\ 0 & 0 & 0 \end{Bmatrix} \begin{Bmatrix} \bar{\delta}_{f,w} \\ \bar{\delta}_{f,t} \\ \bar{\delta}_{f,c} \end{Bmatrix} \tag{4.4}$$

With the trim constraint solved in the first step (Eq. 4.3), the eight variation flaps are the unknowns. There are, however, four additional equations, creating an over determined system when solving for optimal variation flaps. In the first three added equations, the terms $C_{L_{w,1}}$, $C_{L_{t,1}}$, $C_{L_{c,1}}$, etc. represent the lift added to each individual surface (denoted by subscripts w, t, and c for wing, tail, and canard) by the variation flaps. As explained above, each equation is set to zero to ensure that the variation flaps change the lift ratios produced by the mean flaps. The fourth added equation forces the change in airfoil section pitching moment produced by the variation flaps to zero.

Approaching the problem in this manner allows the variation flaps to only redistribute the lift laterally along each surface, ensuring that the lift ratios produced by the mean flaps are maintained and the trim condition is unaltered. While this two-step process is technically unnecessary, the decoupling of the mean and variation flaps provides additional insight. Specifically, the variation flap angles that laterally distribute the lift show how spanwise lift is optimized for the aircraft, and the mean flap angles provide insight into optimal lift ratios for trim.

4.1.4 $C_{D_{tot}}$ Minimization

The previous methods provide the ability to adapt a configuration with multiple TE flaps to achieve minimum induced and profile drag. As was stated in several previous sections of this work, minimizing either induced or profile drag does not necessarily ensure the minimization of total drag $C_{D_{tot}}$. Recall that total drag is defined as the sum of induced and profile drag.

The method for total drag reduction used on the tailless aircraft example, described in Sec. 3.1.3, can also be used for a multiple surface configuration. An optimizer is employed to solve for optimal flap angles with a constraint on the pitching moment. A total drag function which outputs total drag based on configuration geometry and flap angles is used by the optimizer as the function to minimize. The drag polar model described in Sec. 2.2.7 is used to predict the profile drag of the surfaces. For this example, the built-in Matlab optimizer function fmincon was used which finds minimums of nonlinear multivariable functions with equality constraints. The simplex algorithm was used as the optimization algorithm and the tolerance level of the optimizer was set at $1.0e^{-9}$.

4.1.5 Surface Lift Validation Study

A simple way to determine optimal lift ratios of a three surface aircraft is by studying the effect of changes to the incidence of the canard and tail relative to the wing incidence. For validation purposes, a study was performed to mimic that of Goodrich, et al.,[34] which optimally adjusts the incidence angles of the surfaces on a three-surface aircraft in order to minimize induced drag with trim. Figure 4.1 compares the results from the current method with those from LOTS (Linear Optimum Trim Solution)[34] for a static margin of 10% and a $C_{M_0} = -0.1$. While it was not possible to completely replicate the configuration used in the LOTS study,[34] the correlations for how the surfaces are loaded are excellent, validating the effectiveness of the current optimization method. As shown in Fig. 4.1, both methods call for the wing to carry the primary loading while maintaining a slightly negative load on the aft tail.

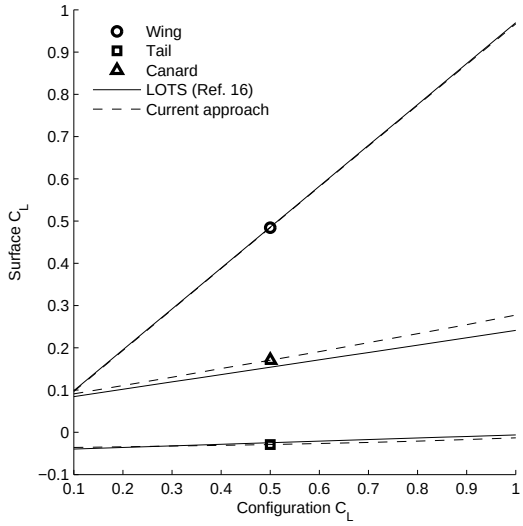

Figure 4.1: Surface lift comparison for a three surface aircraft. Optimization variables are the canard and tail incidence angles.

4.2 Configuration Information

To demonstrate the multiple-surface optimization methods derived in the previous sections, an example three-surface aircraft was created with multiple flaps and multiple locations at which twist could be specified, as displayed in Fig. 4.2. It should be noted that while the methodology was presented for flap variables, wing twist and incidence can be substituted easily, as a flap deflection is comparable to twisting the wing. Twist, incidence, and flaps were all explored as optimization variables and are presented below.

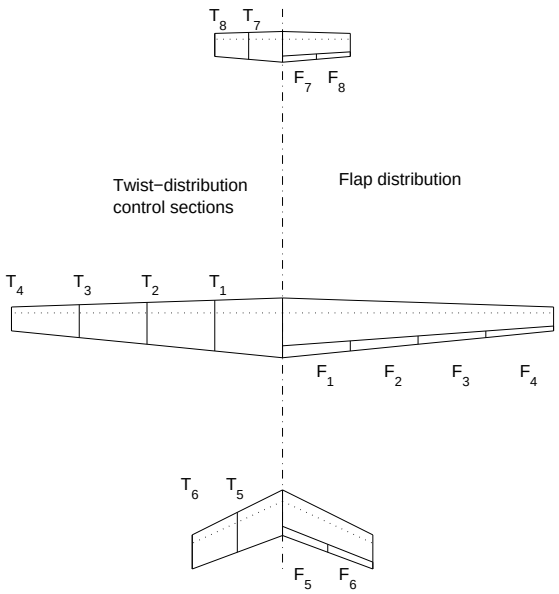

Figure 4.2: Planform for example aircraft. LHS shows twist locations. RHS shows flap locations.

The twist and flap locations are symmetric on each side of the aircraft, but labeled separately in Fig. 4.2 for clarity. The incidence on the tail and canard also exist as variables to be optimized. Table 4.1 details the geometry specifications for the individual surfaces. A three surface configuration was chosen because the added variables should allow for optimal $C_{D_{ind}}$ and trim to be achieved simultaneously. Other aircraft parameters include $W = 18,000$ N, $\bar{c} = 3.933$ ft, and $S = 177.9$ ft^2.

Table 4.1: Individual surface geometry for the example three-surface aircraft.

Surface	Aspect ratio	Span (ft)	$\frac{1}{4}$-chord sweep (deg)	Taper	$z/\bar{c}$	$l/\bar{c}$
Wing	12.95	48	0	0.4	0.0	0.0
Aft tail	4.53	16	25	0.75	1.8	4.32
Canard	5.04	12	0	0.75	-0.62	-6.0

The airfoils used on the configuration were a natural laminar flow (NLF) airfoil on the wing, the MH 201 airfoil on the canard, and the NACA 0012 airfoil on the tail. Specific information about the airfoil sections is presented in Table 4.2.

Table 4.2: Airfoil characteristics for the example three-surface aircraft.

Surface	C_{m_0}	Thickness	Flap hinge
Wing	-0.0802	16%	$0.8c$
Aft tail	0	12%	$0.8c$
Canard	-0.1161	13%	$0.8c$

Figure 4.3 shows drag polar plots and C_p distributions for each the airfoils, not including the NACA 0012. The NLF airfoil used on the wing section (plot (a)) is the same airfoil used on two of the tailless example cases of Sec. 3.3. The MH 201 airfoil shown in plot (b) was designed by Martin Hepperle for use on a canard airplane.[53]

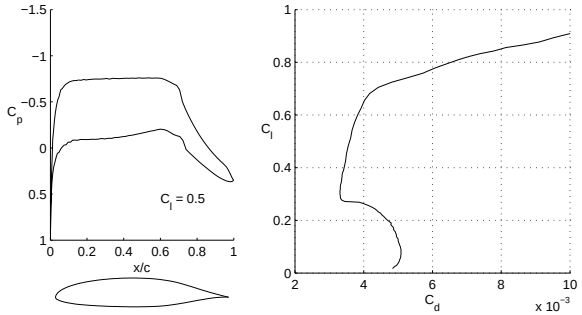

(a) NLF Airfoil, Wing

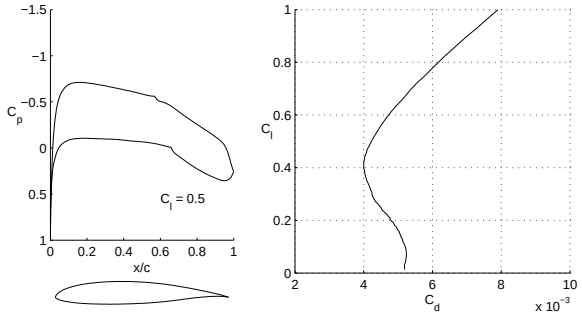

(b) MH 201 Airfoil, Canard

Figure 4.3: C_p distributions and polar plots for the wing and canard airfoils. Results are shown for $Re\sqrt{C_l} = 3e6$.

The wing airfoil was chosen due to its distinct low-drag range and previous success for achieving low profile on the tailless aircraft study. The canard airfoil was chosen because it was designed specifically to be used on a canard.

4.3 Three-Surface Results

4.3.1 Induced Drag Reduction

Presented in this section are the results from different implementations of the induced drag minimization schemes described in Sec. 2.2. Both constrained and unconstrained results are presented and compared with each other. The results include plots of induced, profile, and total drag, as well as span efficiency, and will be referred to in the following subsections.

4.3.1.1 Unconstrained $C_{D_{ind}}$ minimization with twist

In order to gain a baseline understanding of the configuration, and multiple surface configurations in general, it was desired to study how the scheme would perform when no constraints are present. Canard configurations have been shown by studies **??** to be inferior to tailed configurations for achieving low trimmed induced drag with a positive static margin. The reasoning for this is that with the use of a forward surface the NP moves forward. It was shown in Sec. 4.1.5 that for low induced drag the wing carries the majority of the load. Consider the moment about the NP required for trim, presented earlier in Eq. 2.18. For positive longitudinal static stability at a positive C_L the moment at the NP needs to be positive. Typical NLF airfoils have negative C_{m_0} values, which means that the lift must produce a positive moment for trim. But a highly loaded wing and a forward neutral point leads to a negative (nose-down) pitching moment. Therefore, the fore-and-aft lift distribution needs to be off-optimal if a positive SM is necessary. Presented in Fig. 4.4 variations of are $C_{D_{ind}}$ and span efficiency with SM at $C_L = 0.5$ for the example configuration when twisted optimally. The eight twist variables along with the canard and tail incidence angles were used as variables for constrained optimization using the methodology of Eq. 4.1. As shown, $C_{D_{ind}}$ is minimum at a negative SM value. At $C_L = 0.5$, the minimum value of $C_{D_{ind}}$ is 0.00601 achieved at SM $= -35\%\bar{c}$. For a SM of $10\%\bar{c}$, the $C_{D_{ind}}$ is 0.00619.

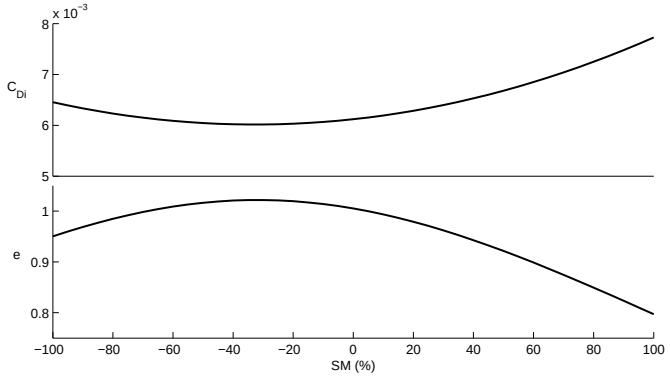

Figure 4.4: $C_{D_{ind}}$ and span efficiency plots for a range of SM values, showing minimum drag at a negative SM for the canard configuration, $C_L = 0.5$.

Presented as solid lines in Fig. 4.5 are $C_{D_{ind}}$ and span efficiency results as a function of C_L for the unconstrained case. For this case, the eight twist variables displayed in Fig. 4.2 along with tail and canard incidence were used as variables in the optimization scheme, and the constraint equation was removed. The results represent the best $C_{D_{ind}}$ values for the example configuration, as the lift distribution is free to take any shape. At $C_L = 0.5$, the $C_{D_{ind}}$ is 0.00601, which matches that from the constrained optimization with the optimum SM $= -35\%\bar{c}$.

4.3.1.2 Constrained $C_{D_{ind}}$ minimization with twist

For this section, the eight twist variables displayed in Fig. 4.2 plus tail and canard incidence were optimized for trimmed induced drag over a range of C_L values. The static margin was set at 10%. Because wing twist does not alter the airfoil section, it will not alter the airfoil section pitching moment (*sections* terms in Eq. 2.19). Any moment added by the twist distribution will be due to the change in spanwise loading, again forcing the lift distribution to trim the aircraft. As discussed in the previous section, for a twisted canard configuration the best trimmed induced drag is expected to be worse than the unconstrained optimal, as the longitudinal distribution of lift needs to be off-optimal to satisfy trim. Displayed in Fig. 4.5 as dashed lines are the results for the constrained, twisted configuration. As shown, both the $C_{D_{ind}}$ values and span efficiency are worse than that for the unconstrained case.

4.3.1.3 Constrained $C_{D_{ind}}$ minimization with flaps

It was shown for the canard configuration that twisting the wing for trimmed induced drag reduction results in less than optimal induced drag. This resulted because the lift distribution was required to produce a positive pitching moment about the NP, as the airfoils have negative C_{m_0} values. First impressions for solving this problem might suggest using airfoils with positive C_{m_0} values, such as reflexed airfoils. While valid, reflexed airfoils tend to have characteristics, such as low $C_{L_{max}}$ values, that make them undesirable.

Flaps, as opposed to twist, not only change the lift distribution, but also affect the section pitching moment. It might be possible, then, to deflect a series of flaps such that the moment contribution added by the section pitching moment produces the necessary positive moment at the NP, while still maintaining optimal fore-and-aft distribution of lift.

To explore this possibility, the eight flaps shown in Fig. 4.2 were used to generate 11 variables (three mean flaps and eight variation flaps) for the optimization scheme. Again, the SM was fixed at 10%. A baseline twist distribution, optimized for induced drag and trim at $C_L = 0.5$, was selected and was kept unchanged during this study. Methods presented in Sec. 4.1.3 were employed, where first the mean flap angles were set to produce an optimal lift ratio for trim, then the variation flaps were deflected to redistribute the lift in the spanwise direction for low induced drag. The results for all C_L values indicate that the mean flaps are forced to negative deflection angles (flap-up), thereby producing a positive section pitching moment, much like a reflexed airfoil.

With a positive moment being produced by the mean flaps, the variation flaps were provided greater flexibility for redistributing the basic load, and thus $C_{D_{ind}}$ approached that of the unconstrained case. The flapped, constrained drag values are presented as dotted lines in Fig 4.5. Also displayed for this case is profile drag response, leading to high total drag. This will be explained further in the following section.

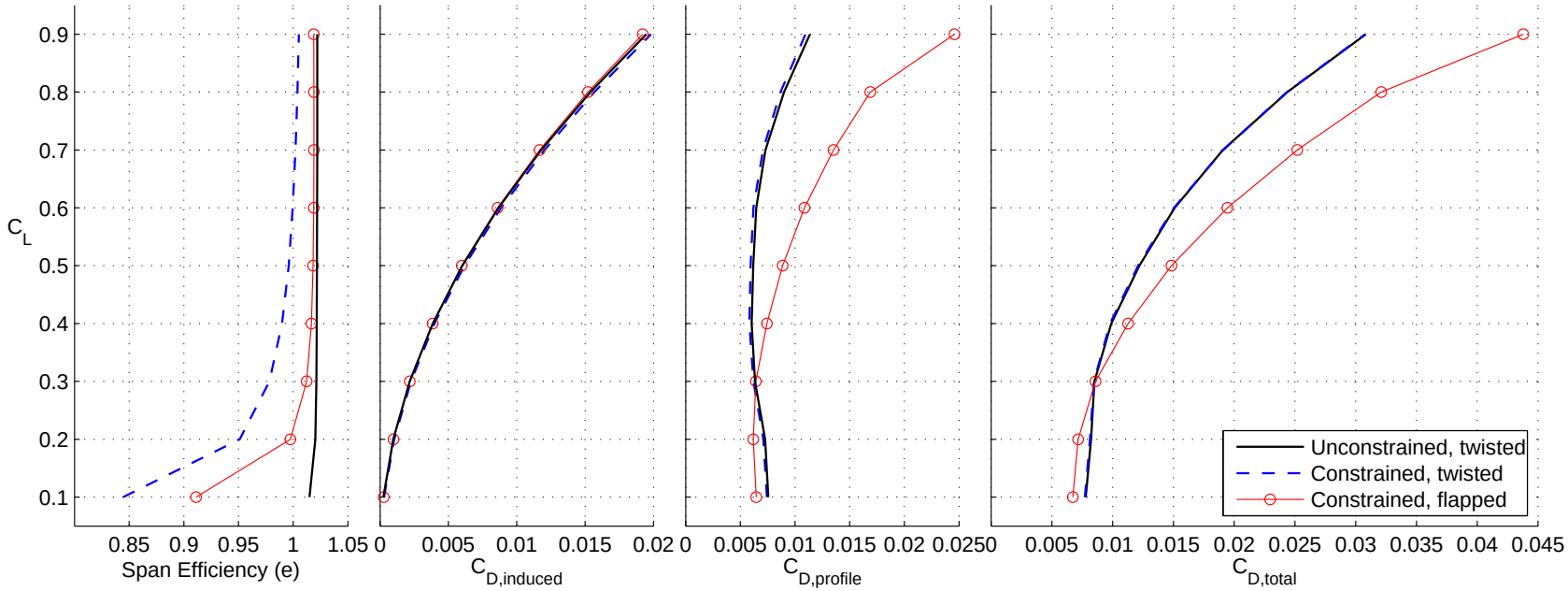

Figure 4.5: Comparison of induced, profile, and total drag for the three-surface configuration with multiple TE flaps. Shown are results from drag reduction schemes using unconstrained twist variables, constrained twist variables, and constrained flap variables for induced drag reduction. Span efficiency results are also shown.

Displayed in Figs. 4.6 and 4.7 are spanwise C_l plots with drag polars from XFOIL[39] superimposed over each flap section to display how well profile drag is being reduced. Induced drag reduction is shown by a comparison of the C_l distribution for the drag reduction scheme (solid line) versus the C_l distribution corresponding to the loading for unconstrained minimum $C_{D_{ind}}$ (circles). In the plots, the vertical dotted lines indicate where each flap section begins and ends. Above the lift plots are deflection values for the flaps at each section, where the line indicates the value of the flap and the arrowhead points to the mean flap value for each surface. The vertical axis of these plots are reversed because negative flap angles refer to upward deflections. As shown in the plots, the flap angles straddle the mean flap values of each surface because the total flap angle is the addition of the mean and variation angles.

The first set of plots in Fig. 4.6 show the results for minimizing induced drag using (a) twist and (b) TE flaps at a wing $C_L = 0.3$. The previous discussion of using twist for optimizing the configuration stated that because twisting the wing results in no change to the airfoil section pitching moment, the list distribution must be altered to trim. This is seen in plot (a), and the lift on the secondary surfaces is off-optimal, resulting in higher induced drag. A flap deflection results in a pitching moment contribution due to the change in airfoil section, which can be used to trim. The lift distribution is then free to optimize for minimum induced drag. Plot (b) shows that for the flap case, nearly optimal induced drag is achieved with trim.

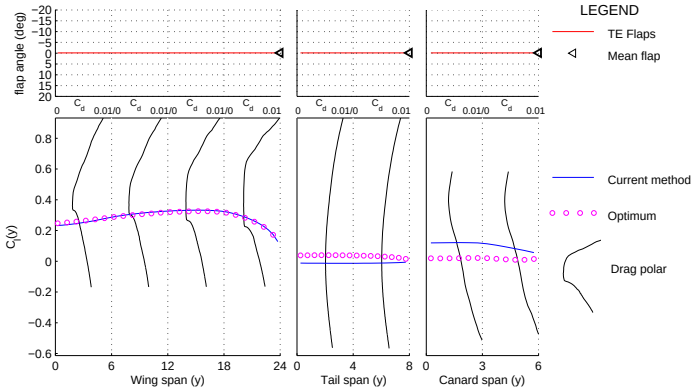

(a) Minimum $C_{D_{ind}}$ using twist

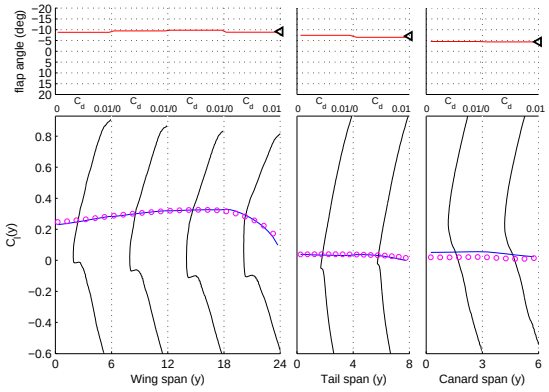

(b) Minimum $C_{D_{ind}}$ using flaps

Figure 4.6: Spanwise C_l and drag polar plots to show how drag is reduced at $C_L = 0.3$ for $C_{D_{ind}}$ minimization using twist and flap variables. RHS shown for the adaptive three-surface configuration.

Figure 4.7 displays similar plots for the high C_L case of 0.7. Induced drag for this C_L responds similar to the $C_L = 0.3$ case above. Profile drag at this C_L is more interesting, as clearly the flap angles shown in plot (b) are causing the wing to operate well outside the airfoil section low-drag ranges. Plot (a) shows that when only wing twist is employed, the airfoils maintain well defined drag buckets and allow lower profile drag. While profile drag is not optimized for the twist case, it is clearly lower than that for the flapped case. Recall that for induced drag reduction using flaps, the mean flap angles were being forced to highly negative values as to produce a positive airfoil section pitching moment and optimal

lift. Plot (b) shows this, and also indicates the increase in profile drag. Clearly, the wing is operating well outside of the airfoil section drag buckets, which have little definition due to the highly negative flap angles. While using flaps allow for optimal induced drag and trim to be achieved, the consequence of higher profile drag outweighs the induced drag benefit and leads to higher total drag. The higher total drag result was shown in Fig. 4.5 for the constrained, flapped case at high C_L values.

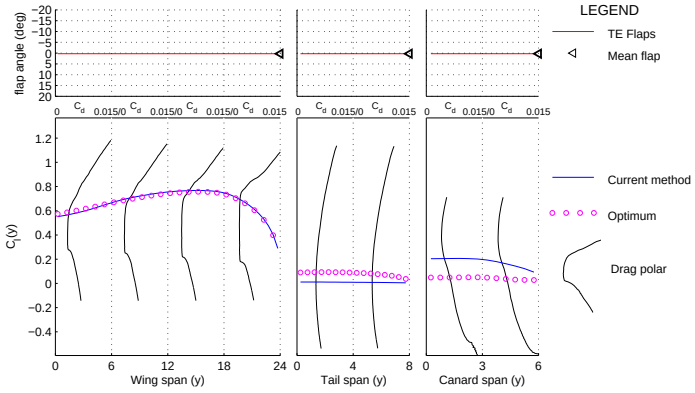

(a) Minimum $C_{D_{ind}}$ using twist

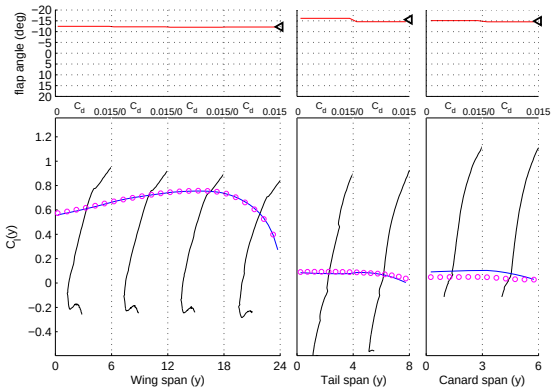

(b) Minimum $C_{D_{ind}}$ using flaps

Figure 4.7: Spanwise C_l and drag polar plots to show how drag is reduced at $C_L = 0.7$ for $C_{D_{ind}}$ minimization using twist and flap variables. RHS shown for the adaptive three-surface configuration.

4.3.2 Profile Drag Reduction

In this section profile drag is the focus, making use of the methodology presented in Sec. 4.1.2. Recall that for profile drag reduction it is important that the surfaces operate in the airfoil low-drag range, and that the mean flap of a surface can be used like a cruise flap for this purpose. For this example, it was chosen to fix the mean flap on the wing. Because of its much larger surface area, the wing will contribute more to profile drag than the tail or canard. With the wing mean flap fixed, the optimization scheme will adjust the other flap angles resulting in the best possible $C_{D_{ind}}$ values, which are hopefully not too far from optimal for reduction of total drag. Figure 4.8 presents results in a similar style to Fig. 4.5, displaying the response to induced, profile, and total C_D, as well as span efficiency as a function of C_L for this case with the wing mean flap set for profile drag reduction. In these plots, the flapped cases in which induced and profile drag reduction are the focus are displayed versus the unconstrained case. Of interest is the expected result that with the mean flap of the wing constrained, the profile drag is much lower through most of the C_L range, however induced drag suffers, as shown clearly in the span efficiency plots. This $C_{D_{ind}}$ penalty is not significant, though, as it is shown in the total drag plot that the profile drag case achieves as good or better drag than the unconstrained case for the entire C_L range. This is a positive result, as it can be concluded that using flaps as a method for wing adaptation, low drag can be achieved for a three-surface configuration with a positive SM.

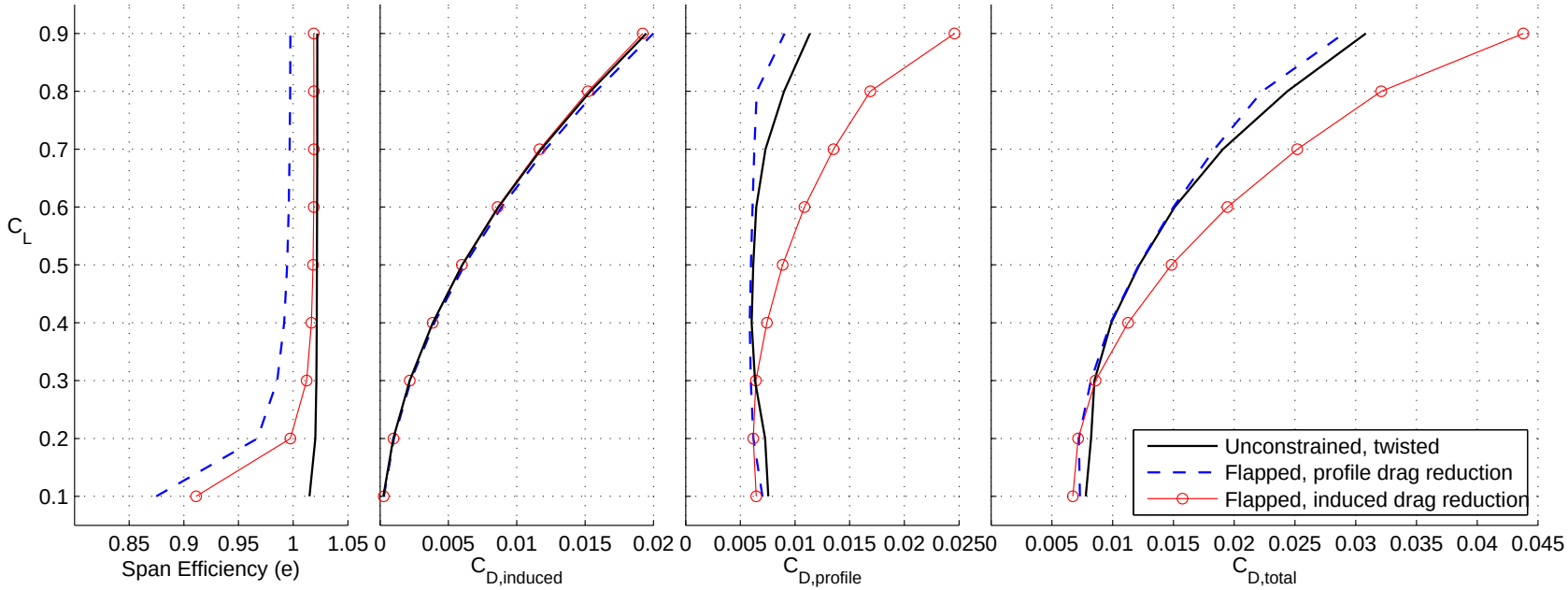

Figure 4.8: Comparison of induced, profile, and total drag for the three-surface configuration with multiple TE flaps. Shown are results from drag reduction schemes using unconstrained twist variables, constrained flap variables for induced drag reduction, and constrained flap variables for profile drag reduction. Span efficiency results are also shown.

Figures 4.9 and 4.10 show spanwise lift results that are similar to those presented above. Example C_L cases of 0.3 and 0.7 are again displayed. Distributions from the flapped case which minimizes induced drag are repeated in the following figures to provide side-by-side comparisons of the induced drag scheme versus the profile drag scheme.

The first set of plots in Fig. 4.9 show the results when flaps are used for reducing (a) induced drag and (b) profile drag at $C_L = 0.3$. Figures 4.5 and 4.8 showed good drag numbers for this C_L, and these plots show why. Plot (a) shows that for minimizing induced drag, the mean flaps are set negative to produce a positive airfoil section pitching moment and optimal lift. It was mentioned that these negative flap deflection should result in poor profile drag. However, at this low C_L a coincidental result occurred where the wing is largely operating in the low drag range, as shown by the polar plots. Therefore, this case results in both low induced and profile drag, and thus total drag, even though no effort was made to ensure this. Plot (b) displays results from the profile drag reduction attempts, which fixed the wing mean flap, in this case to -2.1 deg. The tail and canard mean flaps, along with the variation flaps, were then allowed to find the best solution for trimmed induced drag. The lift distribution for this case is skewed further from the unconstrained lift, especially on the secondary surfaces, thus resulting in more induced drag. As desired, the polar plots indicate that the wing is operating with low profile drag, as each drag bucket is clearly defined and the local C_l values fall inside the drag bucket. The result is that this case sacrifices some induced drag for gains in profile drag, which was the target. As a result, total drag is reduced.

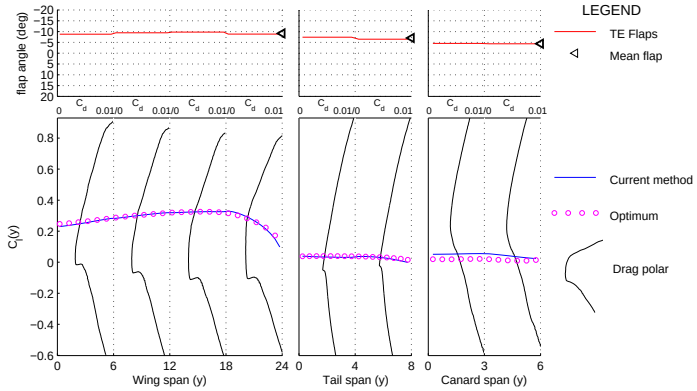

(a) Minimum $C_{D_{ind}}$ using flaps

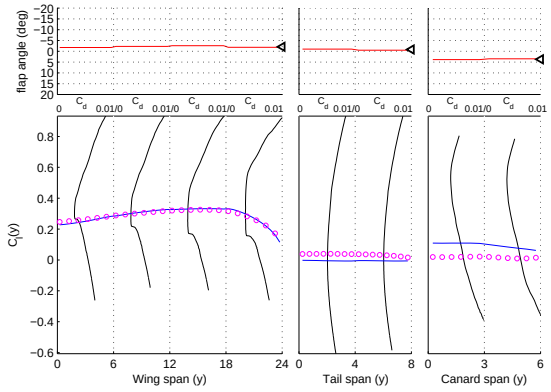

(b) Minimum $C_{D_{pro}}$ using flaps

Figure 4.9: Spanwise C_l and drag polar plots to show how drag is reduced at $C_L = 0.3$ for $C_{D_{ind}}$ minimization and $C_{D_{pro}}$ minimization using flap variables. RHS shown for the adaptive three-surface configuration.

At higher a C_L some pros and cons of the different drag reduction schemes are more clearly illustrated. Displayed in Fig. 4.10 are spanwise lift plots at a $C_L = 0.7$. Figure 4.10(a) again shows that for induced drag reduction the mean flaps are highly negative. And while this provides good induced drag results, the drag polars show the surfaces operating far outside of the low drag range, as the drag buckets are nearly nonexistent. This explains the high profile drag shown in Figs. 4.5 and 4.8. By forcing the wing to operate in the low drag range with the wing mean flap, Fig. 4.10(b) shows that the mean flap value for the wing is no longer negative, and the drag buckets become well defined. For this case

the mean flap of the wing was forced to be 2.5 deg. And while there is some sacrifice of induced drag, this penalty does not weigh heavily on the total drag numbers. In fact, at higher C_L values, this scheme is predicting lower total drag than the unconstrained case.

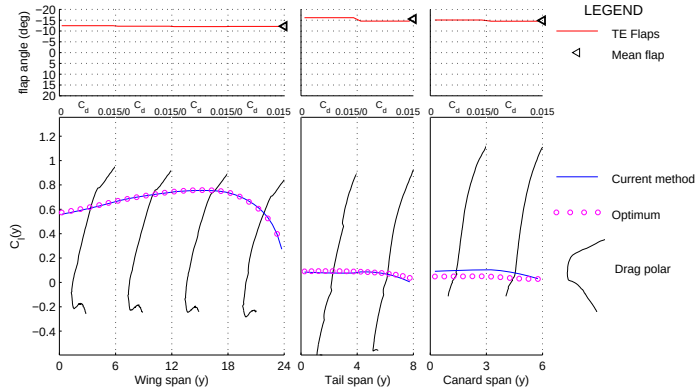

(a) Minimum $C_{D_{ind}}$ using flaps

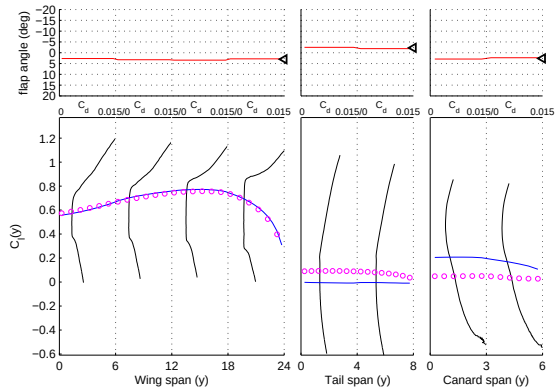

(b) Minimum $C_{D_{pro}}$ using flaps

Figure 4.10: Spanwise C_l and drag polar plots to show how drag is reduced at $C_L = 0.7$ for $C_{D_{ind}}$ minimization and $C_{D_{pro}}$ minimization using flap variables. RHS shown for the adaptive three-surface configuration.

4.3.3 Total Drag Reduction

The previous sections showed examples and results for the drag reduction schemes which used both twist and flaps for minimizing induced and profile drag. Highlighted was the benefits for using flaps versus twist, as the additional pitching moment contribution from

the change in airfoil section allowed for nearly minimum induced drag and trim to be achieved simultaneously. Further, benefits to total drag was shown through the use of flaps, and the wing could be constrained to operate with low profile drag, resulting in low total drag. Section 4.1.4 discusses a method for reducing total drag which is similar to the one used for the tailless aircraft example. Benefits were shown for the tailless configuration in Sec. 3.3 when using the total drag scheme, and thus it was used on the three-surface configuration for comparison.

Figure 4.11 displays results from the total drag reduction scheme plotted with the results from the induced and profile drag minimization schemes using flaps. As shown, the total drag results match well with the results from the profile drag reduction scheme, indicating that for this configuration profile drag is of primary importance. The total drag reduction scheme does lead to slightly lower total drag for the C_L range, as it has found solutions which have less profile drag and the lower and upper C_L limits, and less induced drag for mid-range C_L values. Starting values for the optimizer are again chosen from either the induced or profile drag reduction scheme, whichever has lower total drag. The sensitivity to these starting values could also explain why the total drag results match closely with the profile drag results, as the profile drag case resulted in lower total drag and were most often chosen as starting flap values for the optimizer.

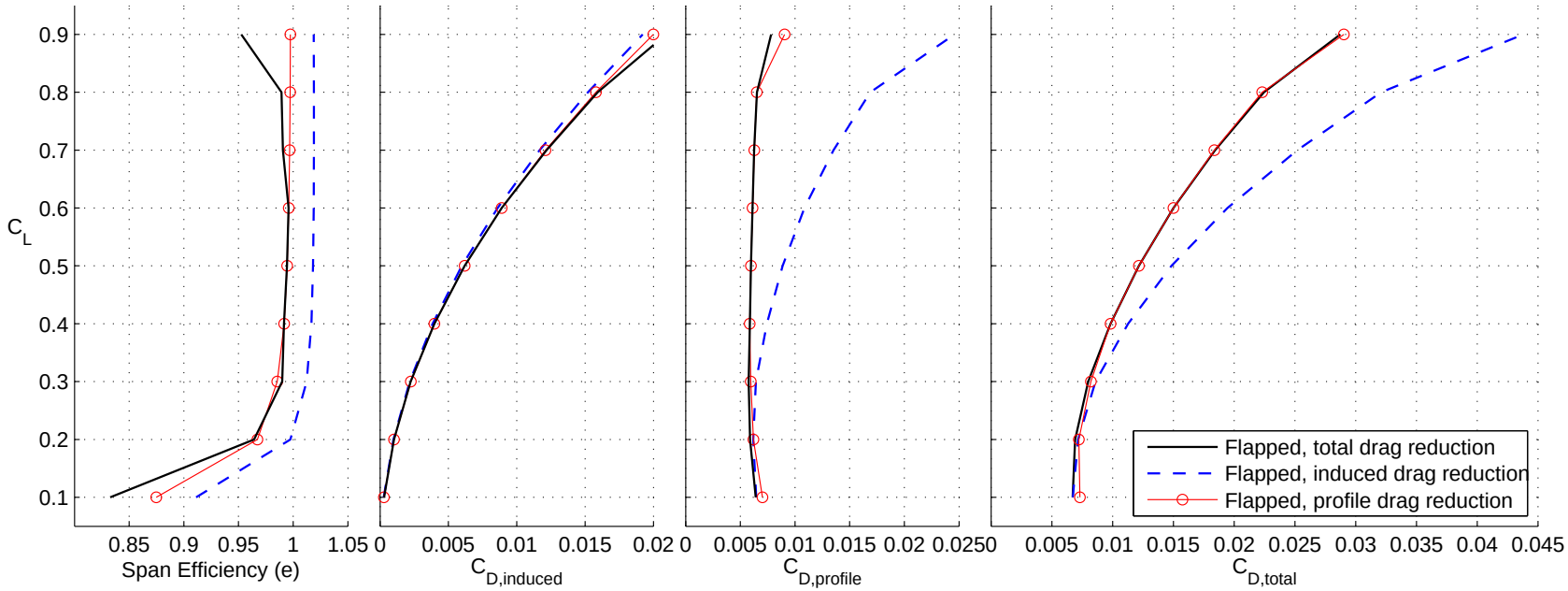

Figure 4.11: Comparison of induced, profile, and total drag for the three-surface configuration with multiple TE flaps. Shown are results from drag reduction schemes using constrained flap variables for total drag reduction, induced drag reduction, and profile drag reduction. Span efficiency results are also shown.

Figures 4.12 and 4.13 provide spanwise lift plots for comparison of the total drag reduction scheme versus the profile drag reduction scheme. The high and low C_L cases of 0.3 and 0.7 are again displayed. As expected, the side-by-side comparison at each C_L shows that the two cases are very similar, indicating only small opportunity to optimize the solution for total drag. This indicates both the importance that profile drag reduction has for achieving low total drag, as well as the aerodynamic opportunities presented by the three surface configuration. The multiple surfaces allow for low induced drag, low profile drag, and trim to be achieved simultaneously.

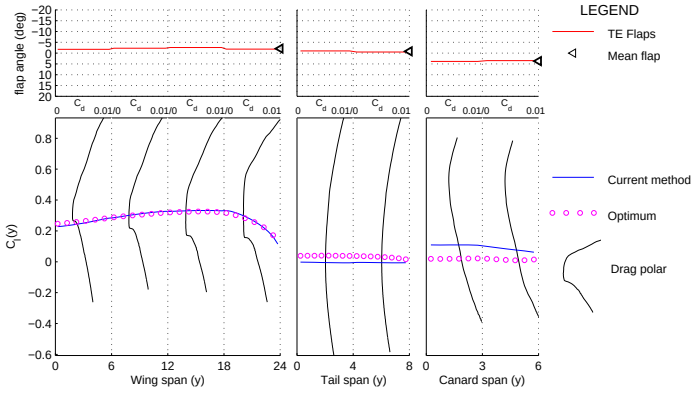

(a) Minimum $C_{D_{pro}}$ using flaps

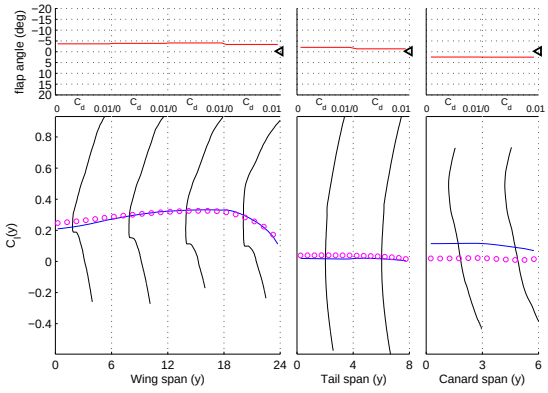

(b) Minimum $C_{D_{tot}}$ using flaps

Figure 4.12: Spanwise C_l and drag polar plots to show how drag is reduced at $C_L = 0.3$ for $C_{D_{ind}}$ minimization and $C_{D_{tot}}$ minimization using flap variables. RHS shown for the adaptive three-surface configuration.

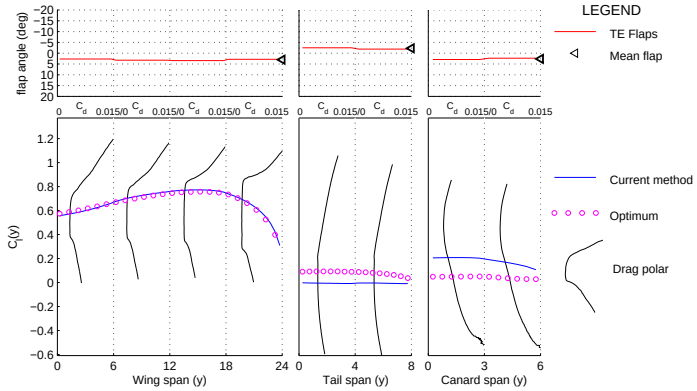

(a) Minimum $C_{D_{pro}}$ using flaps

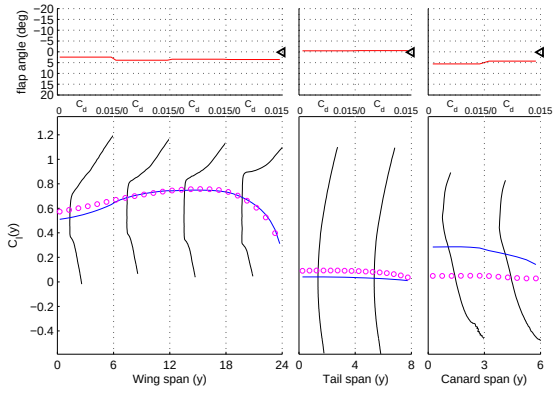

(b) Minimum $C_{D_{tot}}$ using flaps

Figure 4.13: Spanwise C_l and drag polar plots to show how drag is reduced at $C_L = 0.7$ for $C_{D_{ind}}$ minimization and $C_{D_{tot}}$ minimization using flap variables. RHS shown for the adaptive three-surface configuration.

4.4 Three-Surface Aircraft Summary and Conclusions

This chapter presented specific methods for determining optimal lift distributions of adaptive multiple-surface configurations. The drag reduction schemes developed were derived from the background and methodology introduced in Chapter 2. Induced, profile, and total drag reduction schemes were developed which optimize configuration variables including TE flaps (variation and mean flaps), wing twist, and wing incidence. As an example, the drag reduction schemes were applied to a three-surface configuration with multiple twist

and flap variables on each surface. A three-surface configuration was chosen because the additional surfaces provide unique opportunity to solve for optimal lift and trim simultaneously. Results from each drag reduction scheme were analyzed to show their capabilities and potential.

Typical results for a three-surface configuration showed that when optimally twisted, minimum induced drag occurs at a negative static margin, due to the forward cg location. With a trim constraint, using wing twist variables to optimize lift led to off-optimal loading because the lift distribution was adjusted for trim at a positive static margin. When flaps were used instead of twist, however, results showed that minimum induced drag could be achieved at a positive static margin because of the positive section pitching moment contributions from negative flap angles. Particularly at high C_L values, minimizing induced drag required highly negative flap angles to produce the proper pitching moment about the aircraft neutral point. These highly negative flap angles led to high profile drag, and thus high total drag. Methods were then employed to set the mean flaps for low profile drag, and the variation flaps were allowed to redistribute the lift for low induced drag. Results show that this system produced near optimal induced drag numbers and lower profile drag, therefore leading to lower total drag.

The additional surfaces of the three-surface configuration provided the opportunity to find solutions with low induced and profile drag, as well as trim at a positive static margin. When the total drag reduction scheme was employed, only small gains were possible due to the success of the profile drag reduction scheme. The total drag scheme did find slightly better solutions in terms of total drag, however the results matched closely with the results from the profile drag reduction scheme. This either indicates that the profile drag reduction scheme results in nearly optimal flap angles, or that the optimizer used by the total drag reduction scheme was heavily influenced by the starting flap angles. For these results, the flap angles used as input for the optimizer were from the result of the profile drag scheme. While acknowledging the sensitivity of the results from the total drag minimization scheme to inputs, it can be concluded that the results from the total drag scheme validate the success of the drag reduction scheme for reducing drag.

This chapter has extended the adaptive methodology to multiple surface configurations and has shown its potential for reducing drag. Further, the methods have proven to be versatile for use on different applications and design variables. While there are cer-

tainly several other design considerations for multiple-surface aircraft, drag reduction is an important goal. The drag reduction methods can form an important part of a designer's toolbox for complex configurations and for adaptive lifting surfaces.

Chapter 5

Concluding Remarks

5.1 Summary of Research

Adaptive aircraft which can tailor themselves for different flight conditions have gained popularity due to their ability to achieve lower drag and higher efficiency. Methods for wing adaptation have evolved from simple geometry changes required to control the aircraft, to more complex changes that seek to tailor an aircraft for specific flight regimes. No matter the complexity, wing adaptation is central to aircraft design and represents future opportunity for increased efficiency. Recent advancements in adaptive wing technology has led to the desire for applying that technology to unconventional configurations. Unconventional configurations have proven their worth is several instances. Specifically, tailless configurations present theoretical gains in efficiency due to the lack of secondary surface. Also, three-surface configurations provide redundant surfaces for achieving optimal lift and trim simultaneously. These examples provide motivation for further study of adaptive and unconventional configurations. The current work is derived from this desire, and is focused on applying multiple trailing-edge (TE) cruise flaps to various aircraft configurations in an effort to reduce drag. Multiple TE flaps act to optimize a lift distribution by redistributing the spanwise lift of a wing for low drag at various flight conditions.

An aircraft with multiple TE flaps presents complexity for determining the lift distribution resulting from a series of flap deflections and aircraft C_L. However, the concept of basic and additional lift can be used to simplify, and linearize, the problem. Under the assumptions of linear aerodynamics, a configuration lift distribution can be built from

the superposition of the additional lift distribution multiplied by the lift coefficient and individual basic lift distributions resulting from unit flap deflections scaled by the flap angles. If follows that superposition of lift distributions can be used to solve for the induced drag of a multiple flap configuration given flap angles. Provided a linear formulation of induced drag in terms of flap angles, standard constrained minimization techniques can be used to solve for flap angles resulting in minimum induced drag and trim. The research presented methodology which develops matrix expressions derived from the additional and basic lift distributions of a multiple TE flap configuration, which can be solved to produce optimal lift distributions and trim.

Profile drag of airfoils at low subsonic speeds is largely the result of skin friction when no flow separation is present. For low profile drag, natural laminar flow airfoils have been designed which have distinct low-drag-ranges (drag buckets) surrounding a design value. Cruise flaps have been developed which utilize small angle deflections to raise and lower the drag bucket limits of an NLF airfoil. Methods were presented by the research that sets the TE flap angles optimally such that an aircraft is operating within the corresponding airfoil drag buckets, and thus achieving low profile drag. Further, a routine which predicts the drag polar of an NLF airfoil has been developed by this research that approximates the shape of the drag polar based on Reynolds number and flap angle. This allows for profile drag values to be predicted by the drag optimization routines, and methods for determining TE flap angles resulting in minimum total were derived.

A hypothetical tailless aircraft configuration was created to explore the drag reduction capabilities on a single surface. Specific drag reduction schemes were developed which solve for minimum induced and profile drag and trim. The drag reduction schemes utilize specific definitions of the flap angle distribution, decomposing it into a full-span mean flap value and a set of variation flaps taken about the mean. These two variables were utilized independently for reducing induced and profile drag, as they each have specific affects on the lift distributions and pitching moment. It was shown that the mean flap can be used to reduce profile drag and the variation flaps can be used to reduce induced drag. Results were presented for the tailless aircraft configuration with different sweep angles and airfoil sections. The results highlighted the aerodynamic trade-offs associated with tailless aircraft. Methods for reducing induced drag resulted in elliptical loading, however profile drag typically suffered. Conversely, methods for minimized profile drag led to the wing operat-

ing within the drag buckets of the airfoil sections, however induced drag suffered. For each specific drag reduction scheme, total drag was higher then optimal due to the trade-off. A scheme was developed with optimized the flap angles for total drag reduction which provided a solution that optimally balanced induced and profile drag. These solutions showed that minimum total drag often resulted at the expense of some induced and profile drag, and that configuration variables such as wing sweep and airfoil section provide opportunity to optimize a configuration for low drag and trim.

Multiple surface drag reduction schemes were developed which focused on induced, profile, and total drag. As an example, a three-surface aircraft with multiple TE flaps was developed to explore the drag reduction possibilities on a configuration with multiple surfaces. The specific drag reduction schemes similarly used the mean and variation flap angle definitions to independently solve for minimum induced and profile drag, where the mean flap was used to lower profile drag and the variation flaps were used to lower induced drag. Results for the three-surface aircraft were similar to the tailless aircraft in that when induced drag is minimized, profile drag suffers and thus total drag is higher. Profile drag was minimized by forcing the wing surface to operate in the airfoil section drag bucket, and the canard and tail surfaces were used to trim the aircraft. Results showed that when profile drag is reduced, the additional surfaces allow for low induced drag to be achieved as well as trim. Total drag reduction schemes showed that the trade-offs associated with the tailless aircraft were not as prevalent on the three-surface aircraft due to the additional surfaces. Thus, minimizing profile drag for the three-surface configuration typically resulted in best results.

5.2 Future Work

A primary benefit of the research presented in this dissertation is the capability to apply it to any aircraft configuration. The methods were designed to be universal and allow for not only different configurations to be considered, but also different optimization variables. Therefore, flap variables could be inputted into the drag reduction approach along with wing twist or wing incidence variables. The universal nature of the method allows limitless design opportunity for aircraft of various configurations. Further, the mathematical formulation of the constrained minimization technique allows for any constraint which is described in

terms of the optimization variables to be easily inserted into the routine for solving minimum constrained induced drag.

The research presented focused only on planar configurations. Non-planar configurations, such as wings with winglets, are well known for their capabilities for achieving high span efficiency. The current methods can be easily applied to non-planar designs, creating opportunity for analyzing and designing adaptive non-planar configurations. Future studies could focus on the span efficiency gains shown by the non-planar configurations and use flap, or other, variables for optimizing these configuration for low drag.

It was discussed in several sections that using an optimizer for solving flap angles introduces limitations on the solution of total drag. The use of an optimizer provides very little insight into the aerodynamic design, as the optimizer acts as a "black box" for providing flap angles resulting in low total drag. A drag reduction approach that solves for minimum total drag in a more concise and elegant manner, similar to the induced and profile drag reduction schemes presented in this work that where based on aerodynamic and mathematical fundamentals, would extend the capabilities of the drag reduction approach and provide greater opportunity to an aerodynamic designer.

The optimizer starting value sensitivity was another important limitation of the total drag reduction scheme shown by this work. To combat this, the design space could be further explored by a more powerful optimization tool, such as a genetic algorithm (GA). The advantage of a GA versus an optimizer is that the GA can first seed the design space with several random starting points, and exploit promising design space locations to find the minimum value. The GA is less likely to get stuck in areas surrounding the starting values as it is free to more completely explore the design space and seek out other minimum values. With a more powerful optimization tool, such as a GA, the issue of starting value sensitivity could be reduced and total drag results could be presented with more confidence. Further, it was discussed that the optimizer starting value sensitivity was due in part to the drag polar approximation routine which builds the airfoil drag polar in three sections. The sectional nature of the drag polars leads to sharp edges at the transition points where the sections come together, and these sharp edges cause the optimizer to get stuck in those regions. The drag polar approximation routine could be improved to better account for these transition areas, and optimized flap-angle results for total drag minimization could be improved.

Bibliography

[1] Somers, D. M., "Design and Experimental Results for a Natural-Laminar-Flow Airfoil for General Aviation Applications," NASA TP 1861, June 1981.

[2] Anderson, J. D., *Introduction to Flight*, McGraw-Hill, Inc., 1989.

[3] Abzug, M. J. and Larrabee, E. E., *Airplane Stability and Control: A History of the Technologies That Made Aviation Possible*, Cambridge University Press, 2002.

[4] Spillman, J. J., "The use of variable camber to reduce drag, weight and costs of transport aircraft," *Aeronautical Journal*, 1992.

[5] Zink, P. S., Love, M. H., and Youngren, H., "Drag Minimization Through the Use of Mission Adaptive Trailing Edge Flaps and Fuel State Control," AIAA Paper 2004–4365, August 2004.

[6] Neal, D. A., Good, M. G., Johnson, C. O., Robertshaw, H. H., Mason, W. H., and Inman, D. J., "Design and Wind-Tunnel Analysis of a Fully Adaptive Aircraft Configuration," AIAA Paper 2004–1727, 2004.

[7] Ricci, S. and Terraneo, M., "Conceptual Design of an Adaptive Wing for a Three-Surfaces Airplane," AIAA Paper 2005–1959, April 2005.

[8] Thornton, S. V., "Reduction of Structural Loads Using Maneuver Load Control on the Advanced Fighter Technology Integration (AFTI)/F-111 Mission Adaptive Wing," NASA TM 4526, September 1993.

[9] Bolonkin, A. and Gilyard, G. B., "Estimated Benefits of Variable-Geometry Wing Camber Control for Transport Aircraft," NASA TM 1999-206586, October 1999.

[10] Stanewsky, E., "Aerodynamic benefits of adaptive wing technology," *Aerospace Science and Technology*, Vol. 4, 2000, pp. 439–452.

[11] Monner, H. P., Breitbach, E., Bein, T., and Hanselka, H., "Design aspects of the adaptive wing — the elastic trailing edge and the local spoiler bump," *The Aeronautical Journal*, February 2000, pp. 89–95.

[12] King, R. M. and Gopalarathnam, A., "Ideal Lift Distributions and Flaps Angles for Adaptive Wings," AIAA Paper 2004–4722, August 2004.

[13] Cusher, A. A., *Ideal Lift Distributions and Flap Settings for Adaptive Tailless Aircraft*, Master's thesis, North Carolina State University, June 2005, (under the supervision of A. Gopalarathnam).

[14] Segawa, H. and Gopalarathnam, A., "Optimum Flap Angles for Roll Control on Wings with Multiple Trailing-Edge Flaps," AIAA Paper 2008–0319, January 2008.

[15] Shipley, E. and Gopalarathnam, A., "Static Aeroelasticity Considerations in Aerodynamic Adaptation of Wings for Low Drag," AIAA Paper 2006–0451, January 2006.

[16] McAvoy, C. W. and Gopalarathnam, A., "Automated Cruise Flap for Airfoil Drag Reduction Over a Large Lift Range," *Journal of Aircraft*, Vol. 39, No. 6, November–December 2002, pp. 981–988.

[17] Vosburg, V. and Gopalarathnam, A., "The Stability and Control of an Aircraft with an Adaptive Wing," AIAA Paper 2004–4814, August 2004.

[18] Cox, C., Gopalarathnam, A., and Hall, C., "Analysis of Different Stabilizing Control Systems for Aircraft with Automated Cruise Flaps," AIAA Paper 2006–6134, August 2006.

[19] Cox, C., Gopalarathnam, A., and Hall, C., "Development of Stable Automated Cruise Flap for an Aircraft with Adaptive Wing," AIAA Paper 2008–0206, January 2008.

[20] Jepson, J. and Gopalarathnam, A., "Experimental Demonstration of a Sense-and-Adapt Approach for Automated Adaptation of a Wing with Multiple Trailing-Edge Flaps," AIAA Paper 2007–4062, June 2007.

[21] Nickel, K. and Wohlfahrt, M., *Tailless Aircraft in theory and practice*, Edward Arnold, 1994.

[22] Raymer, D. P., *Aircraft Design: A Conceptual Approach*, American Institute of Aeronautics and Astronautics, Inc., 3rd ed., 1999.

[23] Kroo, I., "Aeroelasticity of Very Light Aircraft," *Recent Trends in Aeroelasticity, Structures, and Structural Dynamics*, February 1986, pp. 187 – 202.

[24] Kroo, I., "Tailless Aircraft Design – Recent Experiences," *Symposium on Aerodynamics and Aeroacoustics*, March 1993, pp. 207 – 229.

[25] Liebeck, R. H., Page, M. A., and Rawdon, B. K., "Blended-Wing-Body Subsonic Commercial Transport," AIAA Paper 98–0438, January 1998.

[26] Prandtl, L., "Induced Drag of Multiplanes," NACA TN 182, March 1924.

[27] Laitone, E., "Positive Tail Loads for Minimum Induced Drag of Subsonic Aircraft," *Journal of Aircraft*, Vol. 15, 1978, pp. 837–842.

[28] McLaughlin, M., "Calculations and Comparison with an Ideal Minimum of Trimmed Drag for Conventional and Canard Configurations Having Various Levels of Static Stability," NASA TN-D 8391, 1977.

[29] Laitone, E., "Prandtl's Biplane Theory Applied to Canard and Tandem Aircraft," *Journal of Aircraft*, Vol. 17, 1980, pp. 233–237.

[30] Kroo, I. and McGeer, T., "Optimization of Canard Configurations," ICAS 82–1498, August 1982.

[31] Rokhsaz, K. and Selberg, B. P., "Three-Surface Aircraft – Optimum vs Typical," *Journal of Aircraft*, Vol. 26, No. 8, 1989, pp. 699–704.

[32] Ostowari, C. and Naik, D., "Experimental Study of Three-Lifting-Surface Configuration," *Journal of Aircraft*, Vol. 25, No. 2, 1988, pp. 106–112.

[33] Kendall, E. R., "The Theoretical Minimum Induced Drag of Three-Surface Airplanes in Trim," *Journal of Aircraft*, Vol. 22, No. 10, 1985, pp. 847–854.

[34] Goodrich, K. H., Silwa, S. M., and Lallman, F. J., "A Closed-Form Trim Solution Yielding Minimum Trim Drag for Airplanes With Multiple Longitudinal-Control Effectors," NASA TP 2907, 1989.

[35] Kuethe, A. M. and Chow, C.-Y., *Foundations of Aerodynamics: Bases of Aerodynamic Design*, John Wiley and Sons, Inc., 5th ed., 1997.

[36] Anderson, R. F., "Determination of the Characteristics of Tapered Wings," NACA Rept. 572, 1936.

[37] Abbott, I. H. and von Doenhoff, A. E., *Theory of Wing Sections*, Dover, New York, 1959.

[38] Munk, M. M., "The Minimum Induced Drag of Aerofoils," NACA Rep. 121, 1921.

[39] Drela, M., "XFOIL: An Analysis and Design System for Low Reynolds Number Airfoils," *Low Reynolds Number Aerodynamics*, edited by T. J. Mueller, Vol. 54 of *Lecture Notes in Engineering*, Springer-Verlag, New York, June 1989, pp. 1–12.

[40] Bryson, A. E. Jr and Yu-Chi Ho, *Applied Optimal Control*, John Wiley and Sons, Inc., 1975.

[41] Pfenninger, W., "Investigation on Reductions of Friction on Wings, in Particular by Means of Boundary Layer Suction," NACA TM 1181, August 1947.

[42] Pfenninger, W., "Experiments on a Laminar Suction Airfoil of 17 Per Cent Thickness," *Journal of the Aeronautical Sciences*, April 1949, pp. 227–236.

[43] McGhee, R. J., Viken, J. K., Pfenninger, W., Beasley, W. D., and Harvey, W. D., "Experimental Results for a Flapped Natural-Laminar-Flow Airfoil with High Lift/Drag Ratio," NASA TM 85788, May 1984.

[44] Althaus, D. and Wortmann, F. X., *Stuttgarter Profilkatalog I*, Friedr. Vieweg & Sohn, Braunschweig, 1981.

[45] Drela, M., "Elements of Airfoil Design Methodology," *Applied Computational Aerodynamics*, edited by P. A. Henne, Vol. 125, AIAA, Washington, DC, 1990, pp. 167–189.

[46] Althaus, D., *Niedrig-geschwindigkeits-profile*, Friedr. Vieweg & Sohn Verlagsgesellschaft mbH, Braunschweig/Wiesbaden, 1996.

[47] Cusher, A. and Gopalarathnam, A., "Drag Reduction Methodology for Adaptive Tailless Aircraft," AIAA Paper 2006–3320, June 2006.

[48] Cusher, A. and Gopalarathnam, A., "Drag Reduction on Aircraft Configurations with Adaptive Lifting Surfaces," AIAA Paper 2008–0296, January 2008.

[49] Drela, M. and Youngren, H., *AVL 3.26 User Primer*, MIT Department of Aeronautics and Astronautics, Cambridge, MA 02139, http://web.mit.edu/drela/Public/web/avl/.

[50] Selig, M. S. and Maughmer, M. D., "A Multi-Point Inverse Airfoil Design Method Based on Conformal Mapping," *AIAA Journal*, Vol. 30, No. 5, May 1992, pp. 1162–1170.

[51] Selig, M. S. and Maughmer, M. D., "Generalized Multipoint Inverse Airfoil Design," *AIAA Journal*, Vol. 30, No. 11, November 1992, pp. 2618–2625.

[52] Jones, R. T., "The Spanwise Distribution of Lift For Minimum Induced Drag of Wings Having a Given Lift and a Given Bending Moment," NACA TN 2249, December 1950.

[53] Hepperle, M., *Design of two Airfoils for a Canard Airplane, http://www.mh-aerotools.de/company/paper-3/yaka.html*, MH AeroTools.